ACS ES&T Air

Open Access

Primary Sulfate Is the Dominant Source of Particulate Sulfate during Winter in Fairbanks, Alaska

Allison Moon,* Ursula Jongebloed, Kayane K. Dingilian, Andrew J. Schauer, Yuk-Chun Chan, Meeta Cesler-Maloney, William R. Simpson, Rodney J. Weber, Ling Tsiang, Fouad Yazbeck, Shuting Zhai, Alanna Wedum, Alexander J. Turner, Sarah Albertin, Slimane Bekki, Joël Savarino, Konstantin Gribanov, Kerri A. Pratt, Emily J. Costa, Cort Anastasio, Michael O. Sunday, Laura M. D. Heinlein, Jingqiu Mao, and Becky Alexander*

Cite This: *ACS EST Air* 2024, 1, 139−149

Read Online

ACCESS | Metrics & More | Article Recommendations | SI Supporting Information

ABSTRACT: Within and surrounding high-latitude cities, poor air quality disturbs Arctic ecosystems, influences the climate, and harms human health. The Fairbanks North Star Borough has wintertime particulate matter (PM) concentrations that exceed the Environmental Protection Agency's (EPA) threshold for public health. Particulate sulfate (SO_4^{2-}) is the most abundant inorganic species and contributes approximately 20% of the total PM mass in Fairbanks, but air quality models underestimate observed sulfate concentrations. Here we quantify sulfate sources using size-resolved $\delta^{34}S(SO_4^{2-})$, $\delta^{18}O(SO_4^{2-})$, and $\Delta^{17}O(SO_4^{2-})$ of particulate sulfate in Fairbanks from January 18th to February 25th, 2022 using a Bayesian isotope mixing model. Primary sulfate contributes 62 ± 12% of the total sulfate mass on average. Most primary sulfate is found in the size bin with a particle diameter < 0.7 μm, which contains 90 ±5% of total sulfate mass and poses the greatest risk to human health. Oxidation by all secondary formation pathways combined contributes 38 ± 12% of total sulfate mass on average, indicating that secondary sulfate formation is inefficient in this cold, dark environment. On average, the dominant secondary sulfate formation pathways are oxidation by H_2O_2 (13 ± 6%), O_3 (8 ± 4%), and NO_2 (8 ± 3%). These findings will inform mitigation strategies to improve air quality and public health in Fairbanks and possibly other high-latitude urban areas during winter.

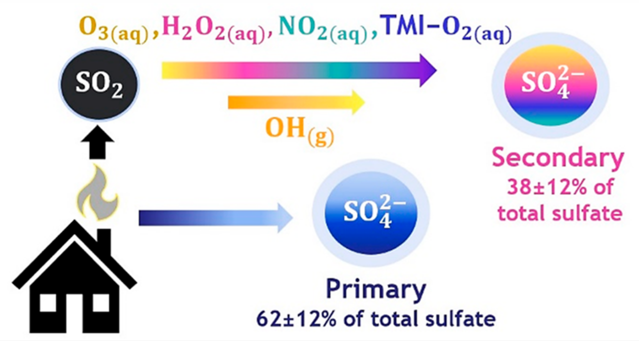

KEYWORDS: *air quality, aerosols, stable isotopes, sulfate, particulate matter, sulfur oxidation*

1. INTRODUCTION

Particulate matter smaller than or equal to 2.5 microns in diameter ($PM_{2.5}$) causes cardiovascular and respiratory diseases and is responsible for over 4 million premature deaths per year globally.[1−4] In urban environments, sulfate is a major contributor to particulate mass, accounting for 20% of $PM_{2.5}$ on average.[5,6] Air quality models often underestimate sulfate concentrations in polluted regions on the order of 2−6× lower than the observed ambient concentrations, suggesting unaccounted for primary sulfate emissions or secondary sulfate formation mechanisms in these environments.[7−9]

The Fairbanks North Star Borough (FNSB) is classified by the US Environmental Protection Agency (EPA) as a "serious" nonattainment area because the city exceeds the 24 h national standard of 35 μg m^{-3} every winter. The American Lung Association ranks Fairbanks in the top three worst cities for 24 h particle pollution, averaging 37 days where $PM_{2.5}$ concentrations exceed 35.5 $\mu g \cdot m^{-1}$ per year between 2017−2021.[10] Pollution events in Fairbanks often occur at temperatures less than −20 °C and are exacerbated by strong temperature inversions, low winds, and minimal vertical mixing.[11,12] Most particulate matter (PM) mass in Fairbanks is organic PM from domestic woodburning (19−52%), gasoline exhaust (16−18%), and diesel (9−14%).[13−16] After woodsmoke, sulfate is the second largest contributor to $PM_{2.5}$ mass (15−33%).[14−16] Community multiscale air quality (CMAQ) model simulations underestimate sulfate concentrations during winter in FNSB by 67%.[17] This discrepancy

Received: August 9, 2023
Accepted: September 28, 2023
Published: November 29, 2023

makes it difficult to use the model to develop effective mitigation measures for reducing atmospheric sulfate.

Most studies conducted in Fairbanks have identified residential fuel oil as the dominant source of sulfur PM in Fairbanks.[14−16,18] Wood-fired space heating is a minor source of atmospheric sulfur in Fairbanks. Emissions inventories in Fairbanks estimate that woodburning produces 4% as much SO_2 as fuel oil in tons·day^{-1} for space heating sources.[19] Coal is not considered an important sulfate source even though several coal-fired power plants are within the Fairbanks nonattainment area.[19] These plants burn low-sulfur coal from the Usibelli mine (sulfur content < 0.20%).[19] Most importantly, their smokestacks often emit above the stable and shallow inversion layer (<20 meters) during winter pollution events.[11,12,19] This suggests that there is a minimal contribution of coal-derived sulfate on the highest pollution days in Fairbanks and that ground-level, residential fuel oil combustion is the major sulfur source.[11,12,20]

Primary sulfate is a sulfate that is emitted from a plume fully oxidized.[21] It is parameterized in emissions inventories and air quality models using a bottom-up approach, where most sulfur is emitted in the form of gas-phase sulfur dioxide (SO_2), and 1−5% is emitted directly as primary sulfate.[1,22,23] Current CMAQ modeling in Fairbanks uses a primary sulfate emission factor of 0.5%. This value is calculated from speciation profiles of Fairbanks heating oil and the ratio of primary sulfate per gallon of fuel oil burned, where the latter is largely based on literature published between 1960−1980.[19,23] The accuracy of this emission factor is limited by the paucity of both laboratory and ambient primary sulfate observations.

The main formation pathways of secondary sulfur PM in polluted environments are gas-phase oxidation of SO_2 by OH and aqueous-phase oxidation of dissolved SO_2 in cloud and aerosol particles by hydrogen peroxide (H_2O_2), ozone (O_3), nitrogen dioxide (NO_2), and oxygen (O_2) (via transition metal ion catalysis (TMI-O_2)) to form sulfate.[7,24,25] Additionally, hydroxymethanesulfonate (HMS), an adduct of sulfite/bisulfite ($SO_3{}^{2-}$/$HSO_3{}^-$) and formaldehyde (HCHO) that is present in PM, can be a major organosulfur species in wintertime haze events in HCHO-rich environments.[26−29]

Factors that influence PM sulfur formation in both cloud drops or aerosol particles include oxidant concentrations, liquid water content, pH, and ionic strength.[3,7,18,25,30−32] Due to the short duration of daylight during winter in Fairbanks (4−6 h day^{-1}), photochemically-produced oxidant abundances (OH and H_2O_2) may be low.[33] Additionally, O_3 is not abundant during ultrapolluted periods because it is titrated by NO_x at the surface.[11] Due to low oxidant abundances and cloud liquid water, it has been hypothesized that sulfur aerosol production in Fairbanks occurs via multiphase and heterogeneous oxidation of SO_2 in aerosol liquid water (ALW) with high ionic strength.[7,18,20,25,34−36] The high ionic strength of ALW and extremely low temperatures affect the solubility of gaseous SO_2, the partitioning of S(IV) species (SO_2 + $HSO_3{}^-$ + $SO_3{}^{2-}$), and the rate constants of aqueous oxidation.[7,18,32] Finally, pH is important for O_3, NO_2, and TMI-O_2 oxidation because it affects the partitioning of S(IV) species and metal solubility.[34] The O_3 oxidation pathway is only significant at pH > 5−6.[37,38] NO_2 oxidation can occur at lower pH but ultimately exhibits similar pH sensitivity as O_3 since the reaction rate increases as pH and SO_2 solubility increase.[30] Conversely, the TMI-O_2 pathway by both Fe(III) and Mn(II) requires acidic conditions since metal solubility increases as pH decreases.[37] These reactions produce sulfate with a specific oxygen isotopic composition and fractionate sulfur isotopes, resulting in isotopic composition that reflects the sulfur source and sulfate formation pathways.

Oxygen isotopes reveal the prevalence of primary sulfate and characterize the dominant secondary oxidation pathways. Primary sulfate has the heaviest $\delta^{18}O$ signature ($\delta^{18}O(SO_4{}^{2-}) = +23.5 \pm 0.3‰$) because it is composed of molecular oxygen from combustion.[39−41] Secondary sulfate is lighter than primary sulfate because SO_2 exchanges its oxygen atoms with both water vapor and liquid water which has a relatively light oxygen isotopic composition (<0‰), with the most depleted $\delta^{18}O$ values in the Northern Hemisphere at high latitudes (−20 to −30‰).[42−45] Thus, the $\delta^{18}O$ of emitted SO_2 does not retain the oxygen composition of the sulfur source due to rapid isotopic exchange between SO_2 and liquid and vapor H_2O in the atmosphere.[42,43] $\Delta^{17}O(SO_4{}^{2-})$ refers to the enrichment of $\delta^{17}O(SO_4{}^{2-})$ relative to $\delta^{18}O(SO_4{}^{2})$ (eq 1) and has been used in many studies to estimate the importance of H_2O_2 ($\Delta^{17}O(SO_4{}^{2-}) = +0.8‰$) and O_3 ($\Delta^{17}O(SO_4{}^{2-}) = +9.8‰$) oxidation in the atmosphere.[25,34,46−50]

$$\Delta^{17}O(SO_4^{2-}) = \delta^{17}O(SO_4^{2-}) - 0.52(\delta^{18}O(SO_4^{2-})) \qquad (1)$$

$\delta^{34}S(SO_4{}^{2-})$ measurements constrain the contribution of different secondary sulfate formation pathways because sulfur isotopes fractionate during the oxidation of SO_2 to sulfate. Sulfur isotope fractionation factors are unique to a specific oxidation pathway and thus the extent of fractionation is sensitive to the oxidants involved.[51] There are several factors that determine the sulfur isotopic signature: (1) the source signature of SO_2 upon emission, (2) the ambient temperature during oxidation, (3) the oxidation pathway, and (4) the sulfur oxidation ratio (SOR) or degree of sulfate formation relative to its precursors.[52] We present sulfur and oxygen isotope measurements of atmospheric sulfate collected during the Alaskan Layered Pollution and Chemical Analysis (ALPACA) field campaign in Fairbanks, AK in January and February 2022. We use these observations to quantify primary and secondary sulfate sources and show that primary sulfate is the dominant contributor to particulate sulfate.

2. METHODS

2.1. Filter Sample Collection in Fairbanks and Gas-Phase Measurements of SO_2 and O_3. Quartz filters (TE-QMA and TE-230-QZ) were rinsed with 18 MΩ·cm water and pre-combusted at 500 °C for 8 h before being wrapped in aluminum foil in airtight polyethylene bags prior to the field campaign. A Volumetric Flow Controlled Particulate Sampling System (TE-5170) with a 4-stage cascade impactor (TE-230) was used to collect 24 h size-resolved aerosol samples at Fairbanks Community Technical College (CTC) (64.84064° N, 147.72677° W) between January 17th to February 25th, 2022. Size-resolved bins were determined by calculating the particle size cutoff (Dp,50) at 50% collection efficiency using the corrected flow rate in each sample (equation S1 in the Supporting Information). For each collection period, filters were combined to form three-size bins: particle diameters <0.7 μm ($PM_{<0.7}$), 0.7−2.5 μm ($PM_{0.7-2.5}$), and 2.5−10 μm ($PM_{2.5-10}$). Both $PM_{0.7}$ and $PM_{0.7-2.5}$ fall within the EPA-regulated fine particle range deemed $PM_{2.5}$, but they are analyzed in separate size bins here.

Filter samples were collected daily between 9:30 AM to 9:00 AM the following day, except for one exceptionally polluted period between January 31st to February 3rd when the filters were changed twice per day at approximately 9:30 AM and 5 PM local time (Table S2). Prior to each TE-5170 calibration, a 1 min blank with no flow through the air sampler was collected to yield four sets of blanks, for a total of 16 slotted filter blanks and 4 backup filter blanks. In-situ gas-phase SO_2 (Thermo Scientific 43C) and O_3 (Thermo Scientific 49C) were measured from an inlet at 3 meters above the valley floor at the CTC site at 1 min resolution, which was used to calculate the average SO_2 and O_3 concentrations during sample collection.

Ten snow samples were collected throughout the campaign to measure $\delta^{18}O(H_2O_{snow})$. Snow samples were collected from the surface of undisturbed snowpack in 50 mL Nalgene bottles approximately 15 feet from the TE-5170 (Table S5).

Two filter samples were collected for 1 week each at the Poker Flat Research range (65.1256° N, 147.4919° W), a relatively clean site 46 km north of Fairbanks, to represent a two-week average of background sulfate. Atmospheric particles were collected using a high-volume sampler (Digitel, DH77, TSP inlet, 1 m^3 min^{-1}) on pre-combusted quartz filters (Whatman 150 nm diameter).

2.2. Ion Chromatography of SO_4^{2-}, S(IV), and Hydroxymethanesulfonate (HMS). Hydroxymethanesulfonate (HMS), non-HMS S(IV), and sulfate (SO_4^{2-}) concentrations were measured in a Metrostep A Supp-5 ion chromatograph (IC) using a low concentration (1.0 mM $NaHCO_3$ and 3.2 mM Na_2CO_3) isocratic elution method, as described by Campbell et al. (2022). With this IC configuration, non-HMS S(IV) (HSO_3^-, and SO_3^{2-}) and HMS have identical retention times and were distinguished by running two aliquots with and without the addition of H_2O_2. Non-HMS S(IV) is oxidized by H_2O_2 to form sulfate, while HMS resists oxidation by H_2O_2 and remains intact in the aqueous phase.[53] Ambient concentrations of SO_4^{2-}, non-HMS S(IV), and HMS from the filter samples and mean SO_2 concentration during each filter sampling period were used to calculate the sulfur oxidation ratio (SOR) for each filter sample. The SOR represents the number of moles of SO_4^{2-} formed relative to the total moles of sulfur species and is an indicator of the degree of oxidation of SO_2 to sulfate aerosol (eq 2):

$$\mathrm{SOR} = \frac{[\mathrm{SO_4^{2-}}]}{[\mathrm{SO_2}] + [\mathrm{S(IV)}] + [\mathrm{SO_4^{2-}}]} \tag{2}$$

where SO_2 is in mols·m^{-3}, S(IV) refers to total S(IV), including HMS in mols·m^{-3}, and SO_4^{2-} represents all S(VI) species (including H_2SO_4, HSO_4^-, and $SO_4^=$) in mols·m^{-3}.

2.3. Isotope Measurements. For isotope analysis at the University of Washington, samples (including field blanks) were extracted into 18 MΩ·cm Millipore water and then filtered through a 0.2 μm poly(ether sulfone) (PES) syringe filter to remove insoluble species. Due to insufficient PM mass for isotopic analysis, $PM_{0.7-2.5}$ and $PM_{2.5-10}$ measurements combined several consecutive days of samples from 10 periods, which are detailed in Table S2 and indicated in Figure 1. Isotope samples were prepared for silver salt pyrolysis as described in Schauer et al. and Geng et al.[54,55] Briefly, the filtrate was neutralized by converting anions to sodium form with an offline cation exchange resin (AG 50W-X8 Resin from Bio-Rad). This converts sulfuric acid (H_2SO_4) to sodium sulfate (Na_2SO_4), which prevents sample loss due to evaporation. This step is followed by the removal of soluble organics by adding 30% H_2O_2 and drying in a MiVAc Duo concentrator. Sulfate was separated from other ions in the sample matrix in a Dionex ICS-2000 before being converted to Ag_2SO_4 using Ag^+-charged cation-exchange resin, as described in Geng et al.[55]

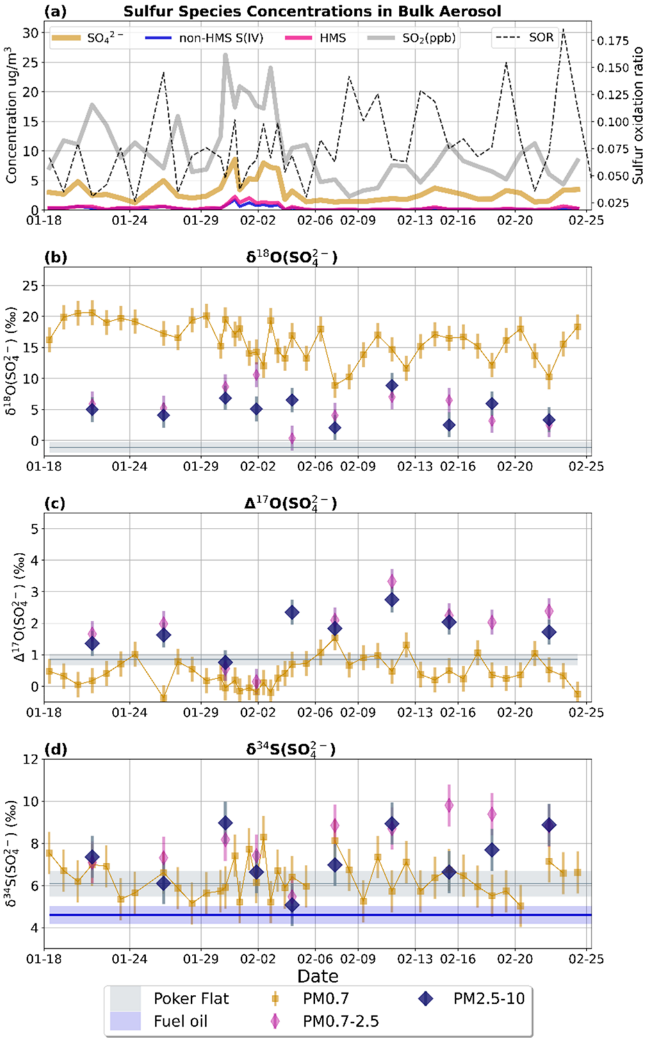

Figure 1. Time series of sulfur species concentrations (a), $\delta^{18}O$(b), $\delta^{18}O$ (c), and $\delta^{18}O$ (d) measurements. (a) Ambient concentrations of sulfur species including SO_4^{2-} (gold), non-HMS S(IV) (blue), and HMS (magenta). The SOR for each sample is plotted with a black dashed line. Isotope observations in (b)−(d) are divided into three size bins: $PM_{0.7}$ (gold squares), $PM_{0.7-2.5}$ (narrow pink diamonds), and $PM_{2.5-10}$ (wide blue diamonds). The error bars represent the propagated errors for each measurement. Daily $PM_{0.7-2.5}$ and $PM_{2.5-10}$ samples were combined into 10 periods as indicated by the vertical gridlines. A 2 week average of isotopic composition at Poker Flat is shown with gray shading in (b)−(d). The measured $\delta^{34}S$ source signature for fuel oil is shown in blue in (d).

Oxygen isotope measurements were performed on a Finnegan MAT253 isotope ratio mass spectrometer using the same configuration as Geng et al.[55] Oxygen isotope measurements were corrected for isotopic exchange with quartz and conversion of HMS and non-HMS S(IV) to sulfate during sample preparation (Supporting Information, section 1.4.1). Sulfur isotope composition was measured using a separate

Finnegan MAT253 isotope ratio mass spectrometer with the same configuration as Jongebloed et al.[56] $\delta^{34}S$ values were normalized to the Vienna Canyon Diablo Troilite (VCDT) scale using four in-house reference materials that are regularly calibrated against the international reference materials IAEA-S-1, IAEA-S-3, and NBS-127. A sulfur isotope correction for sulfate formed from HMS and S(IV) during sample processing was estimated as described in Supporting Information, section 1.4.2. The $\delta^{34}S$ composition of Fairbanks fuel oils #1 and #2 acquired during winter 2022 was measured by combusting 6 μL of fuel oil in a 50 μL tin capsule packed with tin powder. A source signature for $\delta^{34}S_{emission}$ was calculated using the $\delta^{34}S$ measurements for fuel oil #1 (+3.7 ± 0.6‰) and fuel oil #2 (+4.9 ± 0.1‰) and weighing the values by sulfur content (896 and 2053 ppmv, respectively) and domestic use (33% and 67%, respectively; Table S4).[19] This yielded a $\delta^{34}S_{emission}$ signature of +4.7 (±0.6)‰. The analytical error of the measurements (±0.8‰, ±0.2‰, and ±1.0‰ for $\delta^{18}O$, $\Delta^{17}O$, and $\delta^{34}S$, respectively) was estimated from duplicate sample analyses (performed on 30% of the Fairbanks samples) and replicate measurements of standards in quartz and silver capsules. The fully propagated errors, including isotopic corrections for the three measurements, are $\delta^{18}O$ (±1.9‰), $\Delta^{17}O$ (±0.4‰), and $\delta^{34}S$ (±1.2‰).

2.4. Sulfate Source Apportionment Using a Bayesian Isotope Mixing Model. We developed an isotope mixing model to investigate the contributions of primary sulfate and five secondary sulfate formation pathways (H_2O_2, O_3, TMI-O_2, OH, and NO_2). The model inputs are the $\delta^{18}O(SO_4^{2-})$, $\Delta^{17}O(SO_4^{2-})$, and $\delta^{34}S(SO_4^{2-})$ observations. The $\delta^{18}O(H_2O)$ of Fairbanks snow ($\delta^{18}O(H_2O_{(precip)})$) was measured throughout the campaign with an average value of −24.8 ± 2.1‰ (Table S3). The relationship between measured $\delta^{18}O(H_2O_{(precip)})$ and ambient temperature was used to calculate the secondary $\delta^{18}O(SO_4^{2-})$ source signatures for each sample (detailed in Supporting Information, sections 3.1 and 3.2). This represents a source of uncertainty, as the relationship between $\delta^{18}O(H_2O_{(precip)})$ and the temperature was not directly measured for each sulfate sample. For a given temperature, the error in $\delta^{18}O(H_2O_{(precip)})$ is ±0.35‰, which is the error in the intercept of Figure S14(b).

Table 1 summarizes the isotopic signatures used in the model (detailed in Supporting Information, section 3.3).

Table 1. $\delta^{18}O(SO_4^{2-})$, $\Delta^{17}O(SO_4^{2-})$, and $\delta^{34}S(SO_4^{2-})$ Isotopic Signatures Used in Mass Balance Equations

Pathway	$\delta^{18}O(SO_4^{2-})$ (‰) avg ± 1σ[a]	$\Delta^{17}O(SO_4^{2-})$ (‰)	$\delta^{34}S(SO_4^{2-})$ and $\varepsilon^{34}S$[b] (‰) avg ± 1σ[c]
primary	+23.5 ± 0.3	−0.34	$\delta^{34}S_{primary}$ = +4.7 ± 0.6
O_3	+21.3 ± 2.3	+9.8	$\varepsilon^{34}{}_{SO_3}$ = +18.9 ± 0.6
H_2O_2	+9.8 ± 1.5	+0.8	$\varepsilon^{34}S_{H_2O_2}$ = +18.9 ± 0.6
TMI-O_2	−5.6 ± 2.3	−0.09	$\varepsilon^{34}S_{TMI\text{-}O_2}$ = −1.2 ± 1.8
NO_2	+17.5 ± 3.0	0.0	$\varepsilon^{34}S_{NO_2}$ = +1.0 ± 0.465[64]
OH	−6.7 ± 2.1	0.0	$\varepsilon^{34}{}_{S_{OH}}$ = +11.7 ± 0.03

[a] Average ± 1σ reflects the range in $\delta^{18}O(SO_4^{2-})$ signatures due to the temperature-dependence of water vapor and liquid water (see Supporting Information, section 1.3). [b] $\varepsilon_{oxidant} = (\alpha^{34}{}_{oxidant} - 1) \times 1000$ and $\alpha^{34}{}_{oxidant} = (^{34}S/^{32}S)$ products/$(^{34}S/^{32}S)$ reactants. [c] Average ± 1σ reflects the range in ^{34}S signatures and fractionation factors due to the temperature-dependence of sulfur isotope fractionation during secondary sulfate formation (eqs 5−7).[63]

Sulfate formed from the NO_2 oxidation pathway has a light $\delta^{18}O$ signature of −17.2 ± 1.6‰ because NO_2SO_3 decomposes and rapidly hydrolyzes to form SO_4^{2-} and HONO.[25,34,57] TMI-O2-derived sulfate is slightly heavier (−5.3 ± 1.2‰) as the fourth oxygen is from dissolved O_2. The TMI-O_2 path includes both the oxidation of inorganic S(IV) by Fe and Mn as well as by excited triplet states of brown carbon as these produce sulfate with the same O isotopic signature.[24,58] Both H_2O_2 and O_3 oxidation result in a heavier signature ($\delta^{18}O(SO_4^{2-})$ = +10.0 ± 0.8 and +21.3 ± 1.2‰, respectively) because the oxidants themselves have relatively heavy $\delta^{18}O$ values (+22 to +52‰ and +130‰, respectively).[59,60] For H_2O_2, the oxidant supplies two of the four oxygen atoms of sulfate, leaving a smaller contribution from isotopically light water.[50] The H_2O_2 path includes hydrogen peroxide formed in the particle phase and gas phase; however, we expect the gas-phase path to be minor during the most polluted periods because the very high NO_x observed during the campaign may suppress formation of $H_2O_2(g)$.[61,62]

For $\delta^{18}O(SO_4^{2-})$ and $\Delta^{17}O(SO_4^{2-})$, mass balance eqs 3 and 4 were used to represent the fractional contributions of the six sulfate formation pathways.

$$\begin{aligned}\delta^{18}O(SO_4^{2-})(‰) = {} & f_{primary}\cdot\delta^{18}O_{primary} + f_{H_2O_2}\cdot\delta^{18}O_{H_2O_2} + f_{O_3}\cdot\delta^{18}O_{O_3}\\ & + f_{TMI-O_2}\cdot\delta^{18}O_{TMI-O_2} + f_{OH}\cdot\delta^{18}O_{OH}\\ & + f_{NO_2}\cdot\delta^{18}O_{NO_2} \text{ where } f_{primary} + f_{H_2O_2} + f_{O_3}\\ & + f_{TMI-O_2} + f_{OH} + f_{NO_2}\end{aligned} \tag{3}$$

$$\begin{aligned}\Delta^{17}O(SO_4^{2-})(‰) = {} & f_{primary}\cdot\Delta^{17}O_{primary} + f_{H_2O_2}\cdot\Delta^{17}O_{H_2O_2} + f_{O_3}\cdot\Delta^{17}O_{O_3}\\ & + f_{TMI-O_2}\cdot\Delta^{17}O_{TMI-O_2} + f_{OH}\cdot\Delta^{17}O_{OH}\\ & + f_{NO_2}\cdot\Delta^{17}O_{NO_2} \text{ where } f_{primary} + f_{H_2O_2} + f_{O_3}\\ & + f_{TMI-O_2} + f_{OH} + f_{NO_2}\end{aligned} \tag{4}$$

Equations 5−7 show the modeled sulfur isotope fractionation factors for SO_2 oxidation by H_2O_2, O_3, TMI-O_2, and OH as a function of temperature[51,50,51]

$$\varepsilon_{H_2O_2\&O_3} - 1(‰) = 16.51 - 0.085\cdot T(°C) \tag{5}$$

$$\varepsilon_{TMI-O_2} - 1(‰) = -5.039 - 0.237\cdot T(°C) \tag{6}$$

$$\varepsilon_{OH} - 1(‰) = 10.60 - 0.004\cdot T(°C) \tag{7}$$

The fractionation factor (ε_{NO_2}) for SO_2 oxidation by NO_2 is +1.0‰.[64] It should be noted that the average daily temperature in Fairbanks (−30 °C to 0.0 °C) was at times below the temperature ranges tested in laboratory measurements of $\delta^{34}S$ fractionation factors (−25 °C for H_2O_2, O_3, TMI-O_2, OH,) and −7 °C for NO_2.[63,64] Yang et al. found that there was not a significant temperature difference for NO_2 fractionation at temperatures <8 °C.[64]

Sulfur isotope fractionation in secondary sulfate formation is parametrized via Rayleigh distillation. eq 8 was used to calculate the $\delta^{34}S$ isotope fractionation factors (ε) for secondary sulfate as a function of the isotopic primary source signature, average ambient temperature during sample collection (eqs 5−7), and the sulfur oxidation ratio (SOR). $\delta^{34}S_{emission}$ is assumed to be the same as primary sulfate ($\delta^{34}S_{primary}$ = +4.7(±0.6)‰) since sulfur isotope fractionation of fuel oil during high-temperature combustion is expected to

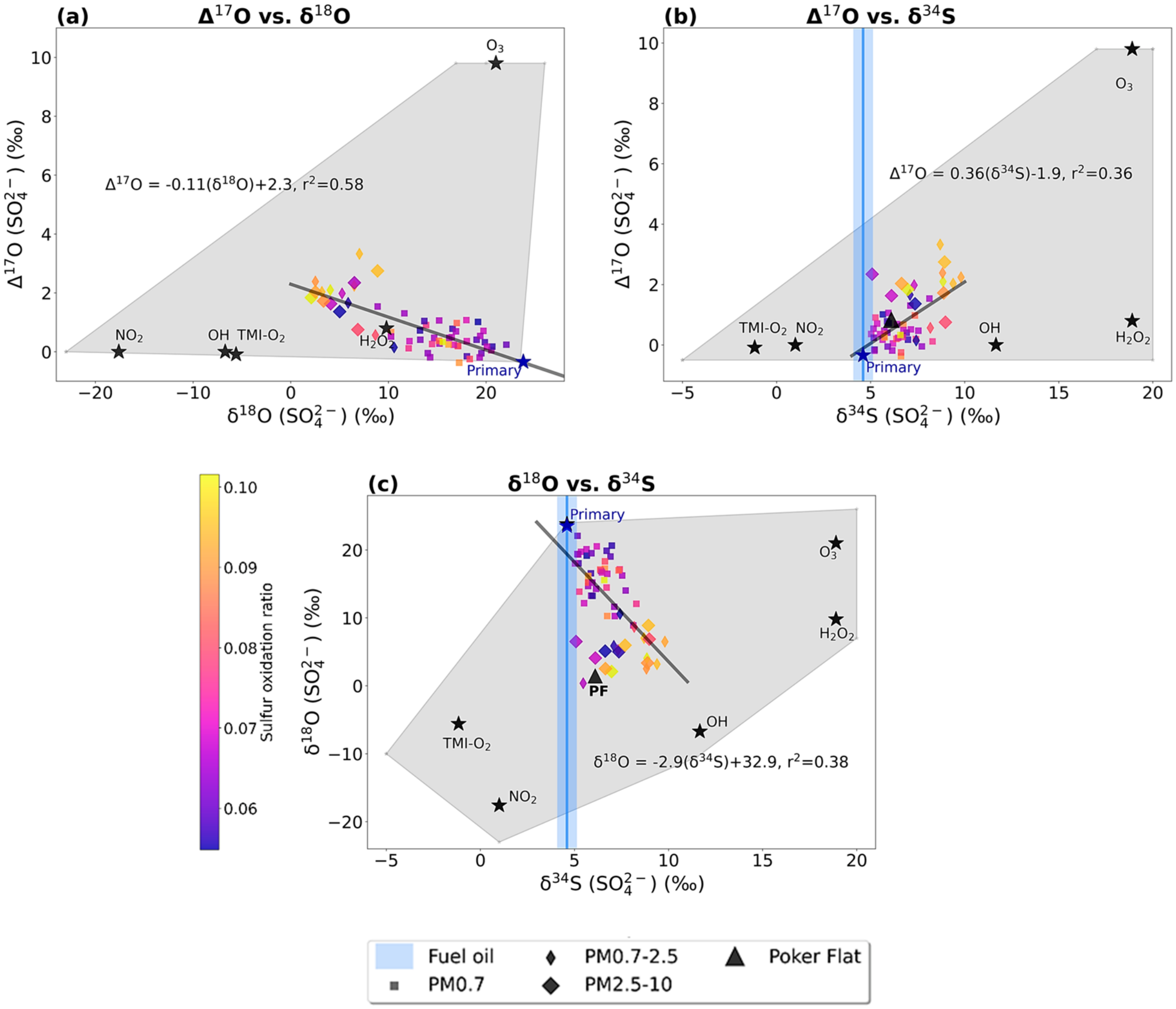

Figure 2. Regressions of (a) $\Delta^{17}O$ vs $\delta^{18}O$, (b) $\Delta^{17}O$ vs $\delta^{34}S$, and (c) $\delta^{18}O$ vs $\delta^{34}S$, where the solid black line is the linear least-squares regression line. The three size bins are depicted by the shape of the marker, as defined in the legend. The color bar shows the sulfur oxidation ratio (SOR) for each sample. Poker Flat measurements are depicted with black triangles. The isotopic composition of fuel oil is shown by a blue line. The gray shaded region shows the full possible range of $\delta^{18}O$, $\Delta^{17}O$, and $\delta^{34}S$ source signatures with the average source signature for each pathway plotted as a black star.

be minimal.[65] This is consistent with previous studies that assume primary sulfate from combustion retains the $\delta^{34}S$-(SO_4^{2-}) signature of the sulfur source.[66−68] We assume that Fairbanks is a closed system, where long-range transport of biogenic and volcanic sulfur can be neglected. This assumption is further supported by prior literature showing that the pollution layer is often confined lower than 20 meters in Fairbanks with the highest $PM_{2.5}$ concentrations below 3 meters.[11,12,19,69] On-road mobile sampling performed by Robinson et al. (2023) found the lowest $PM_{2.5}$ concentrations at the top of hills and asserted that residential neighborhoods were unequivocally the dominant PM source.

$$\begin{aligned}\delta^{34}S(SO_4^{2-})(‰) &= f_{primary} \times \delta^{34}S_{primary} + (1 - f_{primary}) \\ &\quad \times (\delta^{34}S_{emission} - (f_{H_2O_2}\cdot\varepsilon_{H_2O_2} + f_{O_3}\cdot\varepsilon_{O_3} \\ &\quad + f_{TMI-O_2}\cdot\varepsilon_{TMI-O_2} + f_{OH}\cdot\varepsilon_{OH} + f_{NO_2}\cdot\varepsilon_{NO_2})) \\ &\quad \times \left(\ln(1 - SOR)\cdot\frac{1 - SOR}{SOR}\right) \text{where } f_{primary} + f_{H_2O_2} \\ &\quad + f_{O_3} + f_{TMI-O_2} + f_{OH} + f_{NO_2} \\ &= 1 \qquad (8)\end{aligned}$$

We used a Markov Chain Monte Carlo (MCMC) method to estimate the fractional contribution of primary sulfate and five secondary sulfate formation pathways in the isotope mixing model.[70,71] We assumed that the observed $\delta^{18}O(SO_4^{2-})$, $\Delta^{17}O(SO_4^{2-})$, and $\delta^{34}S(SO_4^{2-})$ follow a multivariate Gaussian distribution. We used a Dirichlet distribution as the prior for the fractional contributions such that each fraction is in the interval [0,1] and all fractions sum to 1. MCMC was used to calculate the fractional contributions of each sulfate formation pathway for each sample and estimate the uncertainty by providing a 95% confidence interval.

3. RESULTS AND DISCUSSION

3.1. Ambient Sulfur Concentrations and Isotope Observations.

Figure 1 shows the concentrations of sulfur species contributing to PM mass in Fairbanks between January 18th and February 25th, 2022. Sulfate concentrations range from 1 to 5 $\mu g\ m^{-3}$ and contributes 85 (±9%) of total PM sulfur (sulfate + total S(IV), including HMS and non-HMS S(IV)) by mass throughout most of the campaign (Figure 1a). Non-HMS S(IV) and HMS on average contribute 6 (±3)%

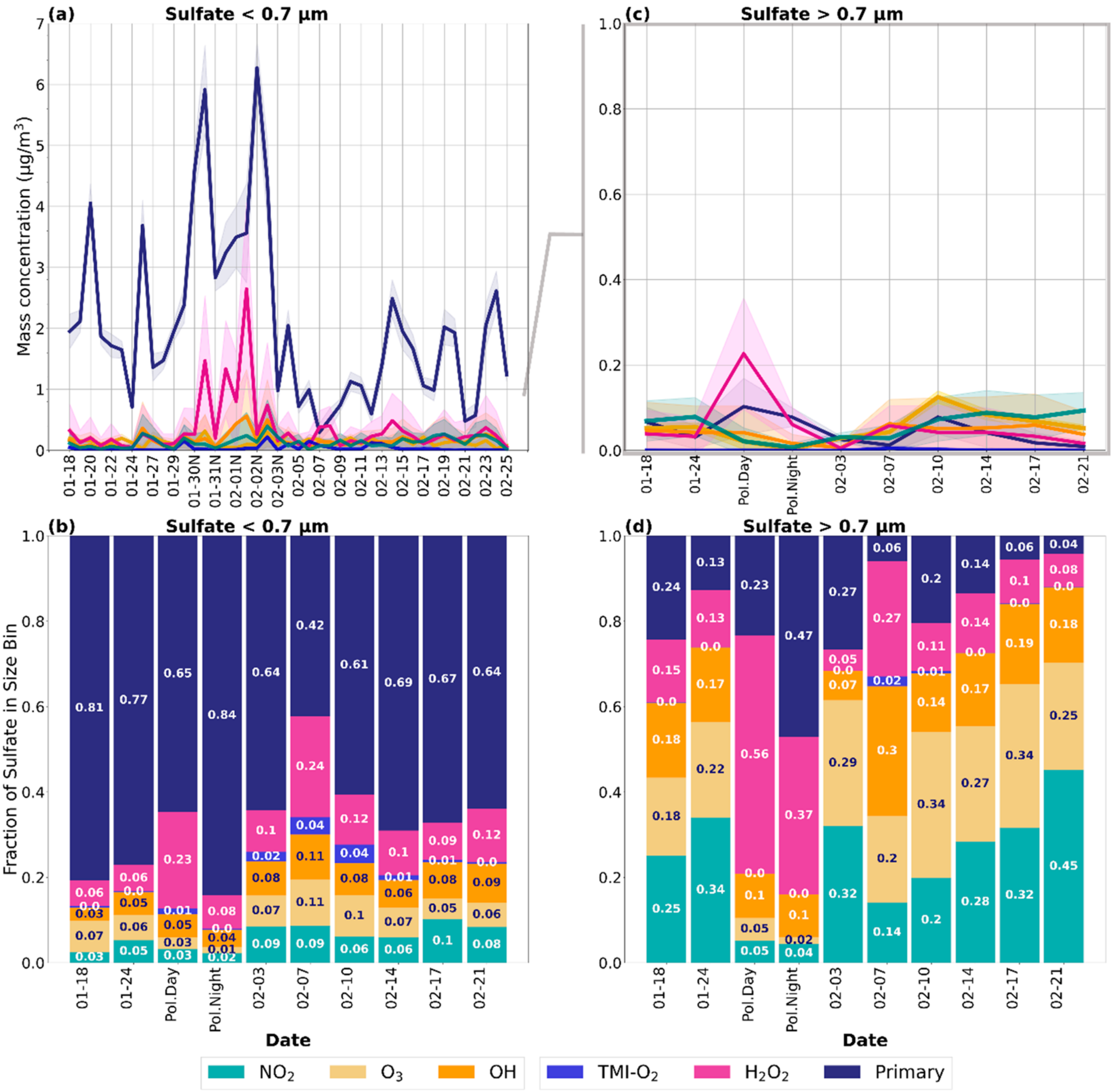

Figure 3. Time series of the estimated contributions of primary sulfate (navy) and secondary sulfate formation via the NO_2 (green), O_3 (gold), OH (orange), TMI-O_2 (light blue), and H_2O_2 (pink) pathways. Mass concentrations and average fractional contributions for $PM_{0.7}$ sulfate are presented in (a) and (b), respectively. Likewise, (c) and (d) show mass concentrations and fractional contributions of $PM_{0.7-2.5}$ and $PM_{2.5-10}$ sulfate combined as $PM_{>0.7}$ μm. The line graphs (a and c) show the estimated mass concentration for each sulfate formation pathway, and the shading represents the 95% confidence interval. The difference in scale for the *y*-axis for (a) and (c) should be noted. The bar charts (b and d) summarize the median fraction for each pathway and period during the campaign. "Day" and "Pol. Night" correspond to the daytime and nighttime samples collected during the ultrapolluted period between January 30th and February 2nd.

and 9 (±6)% of sulfur PM mass, respectively. Sulfur PM and SO_2 concentrations were highest from January 29th and February 3rd, when temperatures averaged −25 °C and were as low as −30 °C. During this period, 23.5 h averaged sulfate concentrations were as high as 7.4 μg m^{-3} and averaged 5.6 μg m^{-3} (Figure 1a). The mass concentrations of S(IV) relative to sulfate were also highest during this period: combined, HMS + non-HMS S(IV) contributed 26% (±8%) sulfur PM mass. The average sulfur oxidation ratio is low during the ultrapolluted period (7 ± 2%) and was similar to the average SOR throughout the campaign (8 ± 4%; Figure 1a). Total sulfate concentrations are not correlated with SOR ($r^2 = 0.02$, p-value > 0.1), but are positively associated with SO_2 ($r^2 = 0.44$, p-value < 0.01; Figure S13).

Figure 1 also shows the oxygen and sulfur isotopic measurements of sulfate in PM. The $PM_{0.7}$ size bin has substantially higher $\delta^{18}O$ and lower $\Delta^{17}O$ (+16.2 ± 3.1‰ and +0.43 ± 0.42‰, respectively) compared to $PM_{>0.7}$ (+5.2 ± 2.5‰ and +1.8 ± 1.2‰ for $PM_{0.7-2.5}$ and $PM_{2.5-10}$, respectively), suggesting a larger fraction of primary sulfate in the smaller size bin (Figures 1b,c). At times, $PM_{0.7}$ $\delta^{18}O$ and $\Delta^{17}O$ observations approach the source signature of primary sulfate (+23.5‰ and −0.35‰, respectively; Table 1). $\delta^{34}S(SO_4^{2-})$ of $PM_{>0.7}$ (+7.7 ± 1.3‰) is more enriched than $PM_{0.7}$ sulfate (+6.4 ± 1.1‰; Figure 1d). There is no relationship between surface temperature at 3 m and $\delta^{34}S(SO_4^{2-})$ observations, suggesting that increased temperatures and enhanced vertical mixing does not have a detectable effect on sulfur isotope composition due to surface mixing of sulfur from coal-fired powerplants. This is consistent with findings in prior literature that suggest that source emissions from powerplants are likely minor contributors of atmospheric sulfate in Fairbanks.[11,12,19] Bulk PM collected at Poker Flat has a $\delta^{34}S$ = +6.1‰, which is similar to Fairbanks. Poker Flat has much lower $\delta^{18}O$ values (−1.1‰) and enriched $\Delta^{17}O$ (+0.85‰), suggesting that secondary sulfate is dominant at this clean location outside Fairbanks. HMS and non-HMS S(IV) concentrations at Poker Flat were below the detection limit.

Figure 2 shows relationships among observed $\delta^{18}O$, $\Delta^{17}O$, and $\delta^{34}S$ in Fairbanks PM plotted adjacent to the isotopic source signatures of the six sulfate formation pathways. The $\Delta^{17}O$ and $\delta^{18}O$ measurements are negatively correlated (Figure 2a; $r^2 = 0.58$, p-value < 0.01). The negative correlation is the opposite of the relationship observed in regions where secondary sulfate dominates due to enrichment in $\Delta^{17}O$ and $\delta^{18}O$ from O_3 and H_2O_2 oxidation.[40,72] A negative relationship between $\Delta^{17}O$ and $\delta^{18}O$ is expected when primary sulfate is significant, indicating a varying influence of primary (high $\delta^{18}O$, low $\Delta^{17}O$) and secondary (low $\delta^{18}O$, high $\Delta^{17}O$) sulfate. The positive correlation ($r^2 = 0.36$, p-value < 0.01) between $\Delta^{17}O$ and $\delta^{34}S$ suggests enrichment in the sulfur isotopes composition with increasing secondary sulfate formation by H_2O_2 and O_3 oxidation of S(IV) (Figure 2b), the only formation pathways leading to $\Delta^{17}O$ > 0.0‰. This is consistent with the fact that these two sulfate formation pathways lead to the largest enrichment in $\delta^{34}S$ (Table 1). In Figure 2c, the negative correlation between $\delta^{18}O$ and $\delta^{34}S$ (r^2 = 0.38, p-value < 0.01) also suggests that secondary sulfate formation leads to lighter $\delta^{18}O$ values and enriched $\delta^{34}S$.

3.2. Sources and Formation of $PM_{0.7}$ Sulfate.

Figure 3 shows the mass concentrations and fractional contributions of the six sulfate formation pathways (primary, O_3, H_2O_2, TMI-O_2, OH, and NO_2) calculated in the isotope mixing model for $PM_{0.7}$ and $PM_{>0.7}$ (see Supporting Information, section 1.4). Primary sulfate is the dominant source of sulfate for $PM_{0.7}$ particles throughout the campaign contributing 2.1 ± 1.4 $\mu g \cdot m^{-3}$ (69 ± 15% of $PM_{0.7}$ sulfate) on average. During the polluted period between January 30th and February 2nd, the fraction of primary sulfate is higher at nighttime (84 ± 9%) compared to daytime (65 ± 8%; p-value < 0.05). The daily-mean primary fraction during the polluted period is not significantly different from other periods in the campaign (p-value = 0.23), though the average mass concentration of primary sulfate was more than twice as high (4.0 ± 1.3 $\mu g \cdot m^{-3}$) compared to other periods (1.6 ± 1.0 $\mu g \cdot m^{-3}$; Figure 3a,b). Widespread use of residential heating oil creates a different pollution regime compared to pollution derived from coal-fired powerplants due the larger amount of direct fine mode primary sulfate emissions (<100 nm).[41,73−76] This study's top-down approach shows that CMAQ emissions inventories in Fairbanks likely underestimate residential sources of primary sulfate PM.

The dominant formation pathway for secondary sulfate in the $PM_{0.7}$ size bin is H_2O_2, which contributes up to 2.6 ± 1.4 $\mu g \cdot m^{-3}$ (37 ± 6% of total $PM_{0.7}$ sulfate) during the polluted period and 0.4 ± 0.3 $\mu g \cdot m^{-3}$ (14 ± 8%) on average throughout the campaign. The difference in the fraction of H_2O_2-derived sulfate in January (7 ± 4%) compared to February (14 ± 8%) is statistically significant (p-value < 0.01), likely due to increased photochemical activity and enhanced vertical mixing in February.

During the polluted period, HMS concentrations (1.1 ± 0.5 $\mu g \cdot m^{-3}$) are comparable to secondary sulfate (1.5 ± 1.0 $\mu g \cdot m^{-3}$), and at times exceed secondary sulfate concentrations (Figure S20). At night during the polluted period, average HMS concentrations (1.0 ± 0.2 $\mu g \cdot m^{-3}$) exceed secondary sulfate (0.79 ± 0.40 $\mu g \cdot m^{-3}$). During the day, secondary sulfate concentrations (2.1 ± 0.9 $\mu g \cdot m^{-3}$) are higher than HMS (1.3 ± 0.7 $\mu g \cdot m^{-3}$), largely due to H_2O_2-derived sulfate, which is responsible for 1.4 ± 0.8 $\mu g \cdot m^{-3}$ of secondary sulfate. Overall, the atmospheric formation of HMS during the most polluted period of the campaign rivals the abundance of secondary sulfate.

Ozone (O_3) contributes 6 ± 4% of sulfate in the $PM_{0.7}$ size bin on average, except during the polluted period where O_3 concentrations are low (<1 ppb) and O_3 contribution to particulate sulfate is less than 4% (Figure S22). O_3 is likely the most important secondary oxidant during the January 24th "heat wave", contributing 13 (±4)% of $PM_{0.7}$, where the average ambient temperature and O_3 concentrations were −0.14 °C and 18.3 ppb, respectively (Figure S22). The increased fractions of O_3-derived sulfate on February 9th, 12th, and 17th correspond with relatively high O_3 concentrations in Fairbanks (>20 ppb on average). The fraction of O_3-derived sulfate in the $PM_{0.7}$ size bin is moderately correlated with ambient O_3 concentrations (r^2 = 0.40, p-value < 0.01; Figure S22).

The fractional contributions of OH, NO_2, and TMI-O_2, shown in Figure 3, are more uncertain since their oxygen isotopic signatures are similar (Table 1). We used the $\delta^{34}S$ observations and known sulfur isotope fractionation factors (eqns. 5−7, Table 1) in the model to help distinguish between these three pathways. On average, NO_2 contribution to $PM_{0.7}$ sulfate (6 ± 4%) is similar to that of the O_3-derived sulfate and is higher in February (7 ± 4%) compared to January (3 ± 2%). NO_2 may be the dominant secondary oxidant directly after the polluted period (February 3rd to February 5th) and for several days in mid to late February (February 9th and February 18th) based on the 95% confidence intervals (Figure 3a). NO_2-oxidation contributes up to 18 (±16)% of sulfate in the $PM_{0.7}$ size bin on February 22. The maximum OH contribution to sulfate 16 (±15)% was also observed February 22, signifying enhanced photochemical activity on that day.

On average, OH-derived sulfate contributes 6 ± 3% of $PM_{0.7}$ sulfate, and, like H_2O_2 and NO_2, it is higher in February (8 ± 3%) compared to January (4 ± 2%). The increase in OH, H_2O_2, and NO_2 production of sulfate in February is likely due to increased solar intensity and longer days (8.5 h of daylight in February vs 6 h in January), leading to enhanced photolysis rates. NO_2 and OH-derived sulfate are moderately correlated (r^2 = 0.40, p-value < 0.01), likely due to the photochemical production of the oxidants themselves (Figure S21). NO_2 oxidation is also correlated with O_3-derived sulfate (r^2 = 0.61, p-value < 0.01), as expected due to their similar pH dependencies (Figure S21). O_3-derived sulfate is relatively constant throughout the campaign (6 ± 3% in January and 7 ± 4% in February), showing less sensitivity to differences in temperature and hours of daylight and more sensitivity to ambient O_3 concentrations and aerosol pH.

The TMI-O_2 pathway (1 ± 2%) is only a minor contributor to $PM_{0.7}$ sulfate. This is consistent with the fact that average total water-soluble iron and manganese on the filters used for isotope analysis are <5 $ng \cdot m^{-3}$ combined and do not exceed 25 $ng \cdot m^{-3}$ combined (Figure S23). Though the model used in this study is a statistical model and not processed-based, the model results are consistent with the pH-dependence of NO_2 and O_3 oxidation of S(IV), the increase in photochemical oxidation in February, and the low solubility of transition metals in Fairbanks, showing that this methodology is useful in interpreting isotope observations with a statistically robust range of uncertainty.

3.3. Sources and Formation of $PM_{>0.7}$ Sulfate. The combined $PM_{0.7-2.5}$ and $PM_{2.5-10}$ size bins, hereafter referred to as $PM_{>0.7}$, only contribute approximately 0.3 ± 0.1 $\mu g \cdot m^{-3}$ (10 ± 5% of total sulfate mass), but show a noteworthy difference in isotopic composition compared to $PM_{0.7}$ sulfate. Primary sulfate is a smaller portion of sulfate in the larger compared to smaller size bins, contributing 16 ± 11% of sulfate in $PM_{>0.7}$. This is consistent with the size of primary sulfate from fuel oil combustion, which is typically <0.1 μm (Figure 3c,d).[34] On average, the main secondary oxidants for $PM_{>0.7}$ sulfate are H_2O_2 (12 ± 18%), O_3 (22 ± 4%), and NO_2 (25 ± 15%) (Figure 3c,d). During late January through early February, the combined O_3 and NO_2 pathways contribute 55 ± 11% of sulfate in $PM_{>0.7}$ (Figure 3c,d). Depending on the abundance of ambient H_2O_2, these pathways are only dominant at pH > 4−5, suggesting aerosol pH within or above this range.

During the ultrapolluted period, primary sulfate is 23 ± 15% of sulfate in $PM_{>0.7}$ during the day and 47 ± 13% at night. As with $PM_{0.7}$ particles, H_2O_2 is the dominant secondary oxidant for $PM_{>0.7}$ during this ultrapolluted period, contributing nearly as much as primary sulfate during the day at 56 ± 22% and 37 ± 24% at night. The combined NO_2 and O_3 pathways contribute 10 ± 8% of $PM_{>0.7}$ sulfate during the daytime and 6 ± 4% at night. The decrease in the level of oxidation of O_3 and NO_2 during the polluted period is likely due to low ambient concentrations of O_3 and may signify a lower pH that inhibits NO_2 oxidation. TMI-O_2 oxidation is insignificant (<1%), further suggesting limited metal solubility.

3.4. Atmospheric Implications. Sulfate is the most abundant PM sulfur species contributing 85 ± 9% of total PM sulfur (sulfate + total S(IV)) by mass throughout most of the campaign. During the ultra-polluted period, the fraction of HMS and non-HMS S(IV) relative to sulfate is the highest of the entire measurement period, contributing 26% (±8%) of PM sulfur mass. It is unclear whether the partially oxidized S(IV) in Fairbanks is primary or secondary in this study, though investigating the sources and speciation of unoxidized sulfur PM warrants further attention. For sulfur control measures, switching to an ultralow sulfur diesel (ULSD) heating oil (15 ppmv sulfur) would likely reduce emissions of primary sulfate and SO_2, but more research is needed to understand how these measures may impact aerosol pH, secondary sulfate formation, and air quality overall. It is also important to acknowledge the economic impacts of increased fuel oil costs, since this financial burden may motivate residents to rely more heavily on woodburning and worsen air quality overall.

The dominance of primary sulfate demonstrated in this study may also highlight a bias in air quality modeling. Missing sulfate is often attributed to incomplete chemistry but could instead be due to dated emission factors or incomplete emission inventories due to the challenge of estimating residential and commercial space heating. These findings are applicable in regions with high rates of fuel oil use for space heating that have not mandated ULSD oil, places with nonexistent or rudimentary sulfur controls on their coal or oil-fired power plants, and over the ocean where high sulfur ship fuel is used. More work is also needed to quantify isotopic fractionation factors at ionic strengths representative of aerosol liquid water. This will improve assumptions in future sulfate isotope studies since literature values are based on bulk solutions meant to simulate cloud water.

ASSOCIATED CONTENT

Supporting Information

The Supporting Information is available free of charge at https://pubs.acs.org/doi/10.1021/acsestair.3c00023.

Experimental methods for sample preparation, isotope analysis, and isotope corrections. It also includes assumptions, code, and performance analysis for the Bayesian isotope mixing model. Finally, there are additional model results based on the assumption that all H_2O_2 formation occurs in particles via the $HOOH_{pm}$ pathways (PDF)

Code for the Bayesian isotope mixing model used in this study, including source signature calculations (PDF)

AUTHOR INFORMATION

Corresponding Authors

Allison Moon − *Department of Atmospheric Sciences, University of Washington, Seattle, Washington 98195, United States;* orcid.org/0000-0002-1648-4869; Email: allimoon@uw.edu

Becky Alexander − *Department of Atmospheric Sciences, University of Washington, Seattle, Washington 98195, United States;* Email: beckya@uw.edu

Authors

Ursula Jongebloed − *Department of Atmospheric Sciences, University of Washington, Seattle, Washington 98195, United States*

Kayane K. Dingilian − *School of Earth and Atmospheric Sciences, Georgia Institute of Technology, Atlanta, Georgia 30332, United States;* Present Address: K.K.D.: Division of Chemistry and Chemical Engineering, California Institute of Technology, Pasadena, CA 91125, United States

Andrew J. Schauer − *Department of Earth and Space Sciences, University of Washington, Seattle, Washington 98195, United States*

Yuk-Chun Chan − *Department of Atmospheric Sciences, University of Washington, Seattle, Washington 98195, United States;* orcid.org/0000-0003-4884-7481

Meeta Cesler-Maloney − *Department of Chemistry and Biochemistry, and Geophysical Institute, University of Alaska Fairbanks, Fairbanks, Alaska 99775-6160, United States*

William R. Simpson − *Department of Chemistry and Biochemistry, and Geophysical Institute, University of Alaska Fairbanks, Fairbanks, Alaska 99775-6160, United States*

Rodney J. Weber − *School of Earth and Atmospheric Sciences, Georgia Institute of Technology, Atlanta, Georgia 30332, United States;* orcid.org/0000-0003-0765-8035

Ling Tsiang − *Department of Atmospheric Sciences, University of Washington, Seattle, Washington 98195, United States;* Present Address: L.T.: Department of Atmospheric and Oceanic Sciences, University of California, Los Angeles, CA 90095, United States.

Fouad Yazbeck − *Department of Atmospheric Sciences, University of Washington, Seattle, Washington 98195, United States*
Shuting Zhai − *Department of Atmospheric Sciences, University of Washington, Seattle, Washington 98195, United States*
Alanna Wedum − *Department of Atmospheric Sciences, University of Washington, Seattle, Washington 98195, United States;* Present Address: A.W.: Department of Climate and Space Sciences and Engineering, University of Michigan, Ann Arbor, MI 48109, United States.
Alexander J. Turner − *Department of Atmospheric Sciences, University of Washington, Seattle, Washington 98195, United States*
Sarah Albertin − *IGE, Univ. Grenoble Alpes, CNRS, INRAE, IRD, Grenoble INP, 38000 Grenoble, France*
Slimane Bekki − *LATMOS/IPSL, Sorbonne Université, UVSQ, CNRS, 75005 Paris, France*
Joël Savarino − *IGE, Univ. Grenoble Alpes, CNRS, INRAE, IRD, Grenoble INP, 38000 Grenoble, France*
Konstantin Gribanov − *Climate and Environment Physics Laboratory, Ural Federal University, 620002 Yekaterinburg, Russia*
Kerri A. Pratt − *Department of Chemistry and Department of Earth and Environmental Sciences, University of Michigan, Ann Arbor, Michigan 48109, United States;* orcid.org/0000-0003-4707-2290
Emily J. Costa − *Department of Chemistry, University of Michigan, Ann Arbor, Michigan 48109, United States*
Cort Anastasio − *Department of Land, Air, and Water Resources, University of California, Davis, California 95616, United States;* orcid.org/0000-0002-5373-0459
Michael O. Sunday − *Department of Land, Air, and Water Resources, University of California, Davis, California 95616, United States*
Laura M. D. Heinlein − *Department of Land, Air, and Water Resources, University of California, Davis, California 95616, United States*
Jingqiu Mao − *Department of Chemistry and Biochemistry, and Geophysical Institute, University of Alaska Fairbanks, Fairbanks, Alaska 99775-6160, United States;* orcid.org/0000-0002-4774-9751

Complete contact information is available at:
https://pubs.acs.org/10.1021/acsestair.3c00023

Notes

The authors declare no competing financial interest.

■ ACKNOWLEDGMENTS

A.M. and B.A. were supported by NOAA Grant NA20OAR4310295. We acknowledge James R. Campbell at UAF for his help with heating oil collection. We acknowledge Yuhan Yang for contributing water-soluble metal concentrations. U.J. acknowledges National Science Foundation Division of Polar Programs (PLR) Grants PLR 1904128 and PLR 629363. W.R.S. and M.C-M. were supported by the NSF Navigating the New Arctic Program (Grant No. 1927750). S.A., S.B., and J.S. were supported by the Agence Nationale de la Recherche (ANR) via Contract ANR-21-CE01-0017 CASPA. R.J.W. and K.D. were supported by the NSF Atmospheric Geoscience Program (Grant No. AGS-2029730) and the NSF Navigating the New Arctic Program (Grant No. NNA-1927778). K.G. was supported by the Russian Science Foundation (Grant No. 21-17-00135). E.J.C. and K.A.P. were supported by the NSF Atmospheric Chemistry and Physical and Dynamic Meteorology (Grant No. AGS-2037091), NSF Navigating the New Arctic (Grant No. RISE-1927831), and the Univ. of Michigan, Dept. of Chemistry. L.M.D.H., M.O.S., and C.A. were supported by the National Science Foundation (Grant No. AGS-2109011). J.M. was supported by the NSF Atmospheric Geoscience Program (Grant No. AGS-2029747) and the NSF Navigating the New Arctic Program (Grant No. ICER-1927750).

■ REFERENCES

(1) Beelen, R.; Hoek, G.; Raaschou-Nielsen, O.; Stafoggia, M.; Andersen, Z. J.; Weinmayr, G.; Hoffmann, B.; Wolf, K.; Samoli, E.; Fischer, P. H.; Nieuwenhuijsen, M. J.; Xun, W. W.; Katsouyanni, K.; Dimakopoulou, K.; Marcon, A.; Vartiainen, E.; Lanki, T.; Yli-Tuomi, T.; Oftedal, B.; Schwarze, P. E.; Nafstad, P.; De Faire, U.; Pedersen, N. L.; Östenson, C.-G.; Fratiglioni, L.; Penell, J.; Korek, M.; Pershagen, G.; Eriksen, K. T.; Overvad, K.; Sørensen, M.; Eeftens, M.; Peeters, P. H.; Meliefste, K.; Wang, M.; Bueno-de-Mesquita, H. B.; Sugiri, D.; Krämer, U.; Heinrich, J.; de Hoogh, K.; Key, T.; Peters, A.; Hampel, R.; Concin, H.; Nagel, G.; Jaensch, A.; Ineichen, A.; Tsai, M.-Y.; Schaffner, E.; Probst-Hensch, N. M.; Schindler, C.; Ragettli, M. S.; Vilier, A.; Clavel-Chapelon, F.; Declercq, C.; Ricceri, F.; Sacerdote, C.; Galassi, C.; Migliore, E.; Ranzi, A.; Cesaroni, G.; Badaloni, C.; Forastiere, F.; Katsoulis, M.; Trichopoulou, A.; Keuken, M.; Jedynska, A.; Kooter, I. M.; Kukkonen, J.; Sokhi, R. S.; Vineis, P.; Brunekreef, B. Natural-Cause Mortality and Long-Term Exposure to Particle Components: An Analysis of 19 European Cohorts within the Multi-Center ESCAPE Project. *Environ. Health Perspect.* **2015**, *123* (6), 525−533.

(2) Dedoussi, I. C.; Eastham, S. D.; Monier, E.; Barrett, S. R. H. Premature Mortality Related to United States Cross-State Air Pollution. *Nature* **2020**, *578* (7794), 261−265.

(3) Hoek, G.; Krishnan, R. M.; Beelen, R.; Peters, A.; Ostro, B.; Brunekreef, B.; Kaufman, J. D. Long-Term Air Pollution Exposure and Cardio- Respiratory Mortality: A Review. *Environ. Health* **2013**, *12* (1), 43.

(4) Waidyatillake, N. T.; Campbell, P. T.; Vicendese, D.; Dharmage, S. C.; Curto, A.; Stevenson, M. Particulate Matter and Premature Mortality: A Bayesian Meta-Analysis. *Int. J. Environ. Res. Public. Health* **2021**, *18* (14), 7655.

(5) Philip, S.; Martin, R. V.; van Donkelaar, A.; Lo, J. W.-H.; Wang, Y.; Chen, D.; Zhang, L.; Kasibhatla, P. S.; Wang, S.; Zhang, Q.; Lu, Z.; Streets, D. G.; Bittman, S.; Macdonald, D. J. Global Chemical Composition of Ambient Fine Particulate Matter for Exposure Assessment. *Environ. Sci. Technol.* **2014**, *48* (22), 13060−13068.

(6) Snider, G.; Weagle, C. L.; Murdymootoo, K. K.; Ring, A.; Ritchie, Y.; Stone, E.; Walsh, A.; Akoshile, C.; Anh, N. X.; Balasubramanian, R.; Brook, J.; Qonitan, F. D.; Dong, J.; Griffith, D.; He, K.; Holben, B. N.; Kahn, R.; Lagrosas, N.; Lestari, P.; Ma, Z.; Misra, A.; Norford, L. K.; Quel, E. J.; Salam, A.; Schichtel, B.; Segev, L.; Tripathi, S.; Wang, C.; Yu, C.; Zhang, Q.; Zhang, Y.; Brauer, M.; Cohen, A.; Gibson, M. D.; Liu, Y.; Martins, J. V.; Rudich, Y.; Martin, R. V. Variation in Global Chemical Composition of $PM_{2.5}$: Emerging Results from SPARTAN. *Atmospheric Chem. Phys.* **2016**, *16* (15), 9629−9653.

(7) Liu, T.; Chan, A. W. H.; Abbatt, J. P. D. Multiphase Oxidation of Sulfur Dioxide in Aerosol Particles: Implications for Sulfate Formation in Polluted Environments. *Environ. Sci. Technol.* **2021**, *55* (8), 4227−4242.

(8) Ye, C.; Lu, K.; Song, H.; Mu, Y.; Chen, J.; Zhang, Y. A Critical Review of Sulfate Aerosol Formation Mechanisms during Winter Polluted Periods. *J. Environ. Sci.* **2023**, *123*, 387−399.

(9) Guo, H.; Weber, R. J.; Nenes, A. High Levels of Ammonia Do Not Raise Fine Particle pH Sufficiently to Yield Nitrogen Oxide-Dominated Sulfate Production. *Sci. Rep.* **2017**, *7* (1), 12109.

(10) American Lung Association. https://www.lung.org/research/sota/city-rankings/msas/fairbanks-ak (accessed 2023-09-12).

(11) Cesler-Maloney, M.; Simpson, W. R.; Miles, T.; Mao, J.; Law, K. S.; Roberts, T. J. Differences in Ozone and Particulate Matter Between Ground Level and 20 m Aloft Are Frequent During Wintertime Surface-Based Temperature Inversions in Fairbanks, Alaska. *J. Geophys. Res. Atmospheres* **2022**, *127* (10), 1−17.

(12) Tran, H. N. Q.; Mölders, N. Investigations on Meteorological Conditions for Elevated PM2.5 in Fairbanks, Alaska. *Atmospheric Res.* **2011**, *99* (1), 39−49.

(13) Kotchenruther, R. A. Source Apportionment of PM2.5 at Multiple Northwest U.S. Sites: Assessing Regional Winter Wood Smoke Impacts from Residential Wood Combustion. *Atmos. Environ.* **2016**, *142*, 210−219.

(14) Wang, Y.; Hopke, P. K. Is Alaska Truly the Great Escape from Air Pollution? - Long Term Source Apportionment of Fine Particulate Matter in Fairbanks, Alaska. *Aerosol Air Qual. Res.* **2014**, *14* (7), 1875−1882.

(15) Ward, T.; Trost, B.; Conner, J.; Flanagan, J.; Jayanty, R. K. M. Source Apportionment of PM2.5 in a Subarctic Airshed - Fairbanks, Alaska. *Aerosol Air Qual. Res.* **2012**, *12* (4), 536−543.

(16) Ye, L.; Wang, Y. Long-Term Air Quality Study in Fairbanks, Alaska: Air Pollutant Temporal Variations, Correlations, and PM2.5 Source Apportionment. *Atmosphere* **2020**, *11* (11), 1203.

(17) *Alaska Department of Environmental Conservation (DEC) Division of Air Quality Technical Analysis Modeling Report for Phase 1, 2 and 3*; Alaska Department of Environmental Conservation, 2023.

(18) Campbell, J. R.; Battaglia, M.; Dingilian, K.; Cesler-Maloney, M.; St Clair, J. M.; Hanisco, T. F.; Robinson, E.; DeCarlo, P.; Simpson, W.; Nenes, A.; Weber, R. J.; Mao, J. Source and Chemistry of Hydroxymethanesulfonate (HMS) in Fairbanks, Alaska. *Environ. Sci. Technol.* **2022**, *56* (12), 7657−7667.

(19) *Alaska Department of Environmental Conservation (DEC) State Air Quality Control Plan Emission Inventory Data*; Alaska Department of Environmental Conservation, 2019; Vol. *II: III.D.7.6*.

(20) Shakya, K. M.; Peltier, R. E. Investigating Missing Sources of Sulfur at Fairbanks, Alaska. *Environ. Sci. Technol.* **2013**, *47* (16), 9332−9338.

(21) Coykendall, L. H. Formation *and* Control *of* Sulfur Oxides *in* Boilers. *J. Air Pollut. Control Assoc.* **1962**, *12* (12), 567−591.

(22) Chin, M.; Rood, R. B.; Lin, S.-J.; Müller, J.-F.; Thompson, A. M. Atmospheric Sulfur Cycle Simulated in the Global Model GOCART: Model Description and Global Properties. *J. Geophys. Res. Atmospheres* **2000**, *105* (D20), 24671−24687.

(23) *AP 42, Fifth ed., Vol. I Chapter 1: External Combustion Sources*; United States Environmental Protection Agency, 1998.

(24) Alexander, B.; Park, R. J.; Jacob, D. J.; Gong, S. Transition Metal-Catalyzed Oxidation of Atmospheric Sulfur: Global Implications for the Sulfur Budget. *J. Geophys. Res.* **2009**, *114* (D2), D02309.

(25) Shao, J.; Chen, Q.; Wang, Y.; Lu, X.; He, P.; Sun, Y.; Shah, V.; Martin, R. V.; Philip, S.; Song, S.; Zhao, Y.; Xie, Z.; Zhang, L.; Alexander, B. Heterogeneous Sulfate Aerosol Formation Mechanisms during Wintertime Chinese Haze Events: Air Quality Model Assessment Using Observations of Sulfate Oxygen Isotopes in Beijing. *Atmospheric Chem. Phys.* **2019**, *19* (9), 6107−6123.

(26) Moch, J. M.; Dovrou, E.; Mickley, L. J.; Keutsch, F. N.; Liu, Z.; Wang, Y.; Dombek, T. L.; Kuwata, M.; Budisulistiorini, S. H.; Yang, L.; Decesari, S.; Paglione, M.; Alexander, B.; Shao, J.; Munger, J. W.; Jacob, D. J. Global Importance of Hydroxymethanesulfonate in Ambient Particulate Matter: Implications for Air Quality. *J. Geophys. Res. Atmospheres* **2020**, *125* (18), 1−14.

(27) Munger, J. W.; Tiller, C.; Hoffmann, M. R. Identification of Hydroxymethanesulfonate in Fog Water. *Science* **1986**, *231* (4735), 247−249.

(28) Olson, T. M.; Hoffmann, M. R. On the Kinetics of Formaldehyde-S(IV) Adduct Formation in Slightly Acidic Solution. *Atmospheric Environ. 1967* **1986**, *20* (11), 2277−2278.

(29) Song, S.; Ma, T.; Zhang, Y.; Shen, L.; Liu, P.; Li, K.; Zhai, S.; Zheng, H.; Gao, M.; Moch, J. M.; Duan, F.; He, K.; McElroy, M. B. Global Modeling of Heterogeneous Hydroxymethanesulfonate Chemistry. *Atmospheric Chem. Phys.* **2021**, *21* (1), 457−481.

(30) Cheng, Y.; Zheng, G.; Wei, C.; Mu, Q.; Zheng, B.; Wang, Z.; Gao, M.; Zhang, Q.; He, K.; Carmichael, G.; Pöschl, U.; Su, H. Reactive Nitrogen Chemistry in Aerosol Water as a Source of Sulfate during Haze Events in China. *Sci. Adv.* **2016**, *2* (12), No. e1601530.

(31) Ma, T.; Furutani, H.; Duan, F.; Kimoto, T.; Jiang, J.; Zhang, Q.; Xu, X.; Wang, Y.; Gao, J.; Geng, G.; Li, M.; Song, S.; Ma, Y.; Che, F.; Wang, J.; Zhu, L.; Huang, T.; Toyoda, M.; He, K. Contribution of Hydroxymethanesulfonate (HMS) to Severe Winter Haze in the North China Plain. *Atmospheric Chem. Phys.* **2020**, *20* (10), 5887−5897.

(32) Zhang, H.; Xu, Y.; Jia, L. Hydroxymethanesulfonate Formation as a Significant Pathway of Transformation of SO2. *Atmos. Environ.* **2023**, *294*, 119474.

(33) Hua, W.; Chen, Z. M.; Jie, C. Y.; Kondo, Y.; Hofzumahaus, A.; Takegawa, N.; Chang, C. C.; Lu, K. D.; Miyazaki, Y.; Kita, K.; Wang, H. L.; Zhang, Y. H.; Hu, M. Atmospheric Hydrogen Peroxide and Organic Hydroperoxides during PRIDE-PRD'06, China: Their Concentration, Formation Mechanism and Contribution to Secondary Aerosols. *Atmospheric Chem. Phys.* **2008**, *8* (22), 6755−6773.

(34) He, P.; Alexander, B.; Geng, L.; Chi, X.; Fan, S.; Zhan, H.; Kang, H.; Zheng, G.; Cheng, Y.; Su, H.; Liu, C.; Xie, Z. Isotopic Constraints on Heterogeneous Sulfate Production in Beijing Haze. *Atmospheric Chem. Phys.* **2018**, *18* (8), 5515−5528.

(35) Shen, X.; Lee, T.; Guo, J.; Wang, X.; Li, P.; Xu, P.; Wang, Y.; Ren, Y.; Wang, W.; Wang, T.; Li, Y.; Carn, S. A.; Collett, J. L. Aqueous Phase Sulfate Production in Clouds in Eastern China. *Atmos. Environ.* **2012**, *62*, 502−511.

(36) Schmale, J.; Arnold, S. R.; Law, K. S.; Thorp, T.; Anenberg, S.; Simpson, W. R.; Mao, J.; Pratt, K. A. Local Arctic Air Pollution: A Neglected but Serious Problem. *Earths Future* **2018**, *6* (10), 1385−1412.

(37) Seinfeld, J. H.; Pandis, S. N. *Atmospheric Chemistry and Physics: From Air Pollution to Climate Change*, 2nd ed.; J. Wiley: Hoboken, N.J, 2006.

(38) Tao, W.; Su, H.; Zheng, G.; Wang, J.; Wei, C.; Liu, L.; Ma, N.; Li, M.; Zhang, Q.; Pöschl, U.; Cheng, Y. Aerosol pH and Chemical Regimes of Sulfate Formation in Aerosol Water during Winter Haze in the North China Plain. *Atmospheric Chem. Phys.* **2020**, *20* (20), 11729−11746.

(39) Kroopnick, P.; Craig, H. Atmospheric Oxygen: Isotopic Composition and Solubility Fractionation. *Science* **1972**, *175* (4017), 54−55.

(40) Dominguez, G.; Jackson, T.; Brothers, L.; Barnett, B.; Nguyen, B.; Thiemens, M. H. Discovery and Measurement of an Isotopically Distinct Source of Sulfate in Earth's Atmosphere. *Proc. Natl. Acad. Sci. U. S. A.* **2008**, *105* (35), 12769−12773.

(41) Holt, B. D.; Kumar, R. Oxygen-18 Study of High-Temperature Air Oxidation of SO2. *Atmospheric Environ. 1967* **1984**, *18* (10), 2089−2094.

(42) Holt, B. D.; Kumar, R.; Cunningham, P. T. Oxygen-18 Study of the Aqueous-Phase Oxidation of Sulfur Dioxide. *Atmospheric Environ. 1967* **1981**, *15* (4), 557−566.

(43) Holt, B. D.; Cunningham, P. T.; Engelkemeir, A. G.; Graczyk, D. G.; Kumar, R. Oxygen-18 Study of Nonaqueous-Phase Oxidation of Sulfur Dioxide. *Atmospheric Environ. 1967* **1983**, *17* (3), 625−632.

(44) Aggarwal, P. K.; Alduchov, O. A.; Froehlich, K. O.; Araguas-Araguas, L. J.; Sturchio, N. C.; Kurita, N. Stable Isotopes in Global Precipitation: A Unified Interpretation Based on Atmospheric Moisture Residence Time. *Geophys. Res. Lett.* **2012**, *39* (11), 1−6.

(45) Aggarwal, P. K.; Alduchov, O.; Araguás Araguás, L.; Dogramaci, S.; Katzlberger, G.; Kriz, K.; Kulkarni, K. M.; Kurttas, T.; Newman, B. D.; Purcher, A. New Capabilities for Studies Using Isotopes in the Water Cycle. *Eos Trans. Am. Geophys. Union* **2007**, *88* (49), 537−538.

(46) Lee, C. C.-W.; Thiemens, M. H. The δ^{17}O and δ^{18}O Measurements of Atmospheric Sulfate from a Coastal and High Alpine Region: A Mass-Independent Isotopic Anomaly. *J. Geophys. Res. Atmospheres* **2001**, *106* (D15), 17359−17373.

(47) Lyons, J. R. Transfer of Mass-Independent Fractionation in Ozone to Other Oxygen-Containing Radicals in the Atmosphere. *Geophys. Res. Lett.* **2001**, *28* (17), 3231−3234.

(48) Morin, S.; Savarino, J.; Bekki, S.; Gong, S.; Bottenheim, J. W. Signature of Arctic Surface Ozone Depletion Events in the Isotope Anomaly (Δ¹⁷O) of Atmospheric Nitrate. *Atmospheric Chem. Phys.* **2007**, *7* (5), 1451−1469.

(49) Sofen, E. D.; Alexander, B.; Kunasek, S. A. The Impact of Anthropogenic Emissions on Atmospheric Sulfate Production Pathways, Oxidants, and Ice Core $\Delta^{17}O(SO_4^{2-})$. *Atmospheric Chem. Phys.* **2011**, *11* (7), 3565−3578.

(50) Savarino, J.; Lee, C. C. W.; Thiemens, M. H. Laboratory Oxygen Isotopic Study of Sulfur (IV) Oxidation: Origin of the Mass-Independent Oxygen Isotopic Anomaly in Atmospheric Sulfates and Sulfate Mineral Deposits on Earth. *J. Geophys. Res. Atmospheres* **2000**, *105* (D23), 29079−29088.

(51) Harris, E.; Sinha, B.; Hoppe, P.; Crowley, J. N.; Ono, S.; Foley, S. Sulfur Isotope Fractionation during Oxidation of Sulfur Dioxide: Gas-Phase Oxidation by OH Radicals and Aqueous Oxidation by H_2O_2, O_3 and Iron Catalysis. *Atmospheric Chem. Phys.* **2012**, *12* (1), 407−423.

(52) Harris, E.; Sinha, B.; Hoppe, P.; Foley, S.; Borrmann, S. Fractionation of Sulfur Isotopes during Heterogeneous Oxidation of SO_2 on Sea Salt Aerosol: A New Tool to Investigate Non-Sea Salt Sulfate Production in the Marine Boundary Layer. *Atmospheric Chem. Phys.* **2012**, *12* (10), 4619−4631.

(53) Kok, G. L.; Gitlin, S. N.; Lazrus, A. L. Kinetics of the Formation and Decomposition of Hydroxymethanesulfonate. *J. Geophys. Res.* **1986**, *91* (D2), 2801.

(54) Schauer, A. J.; Kunasek, S. A.; Sofen, E. D.; Erbland, J.; Savarino, J.; Johnson, B. W.; Amos, H. M.; Shaheen, R.; Abaunza, M.; Jackson, T. L.; Thiemens, M. H.; Alexander, B. Oxygen Isotope Exchange with Quartz during Pyrolysis of Silver Sulfate and Silver Nitrate: Oxygen Isotope Exchange during Pyrolysis of Ag_2SO_4 and $AgNO_3$. *Rapid Commun. Mass Spectrom.* **2012**, *26* (18), 2151−2157.

(55) Geng, L.; Schauer, A. J.; Kunasek, S. A.; Sofen, E. D.; Erbland, J.; Savarino, J.; Allman, D. J.; Sletten, R. S.; Alexander, B. Analysis of Oxygen-17 Excess of Nitrate and Sulfate at Sub-Micromole Levels Using the Pyrolysis Method: Analysis of Oxygen-17 Excess of Nitrate and Sulfate. *Rapid Commun. Mass Spectrom.* **2013**, *27* (21), 2411−2419.

(56) Jongebloed, U. A.; Schauer, A. J.; Cole-Dai, J.; Larrick, C. G.; Wood, R.; Fischer, T. P.; Carn, S. A.; Salimi, S.; Edouard, S. R.; Zhai, S.; Geng, L.; Alexander, B. Underestimated Passive Volcanic Sulfur Degassing Implies Overestimated Anthropogenic Aerosol Forcing. *Geophys. Res. Lett.* **2023**, *50* (1), 1−12.

(57) Liu, T.; Abbatt, J. P. D. Oxidation of Sulfur Dioxide by Nitrogen Dioxide Accelerated at the Interface of Deliquesced Aerosol Particles. *Nat. Chem.* **2021**, *13* (12), 1173−1177.

(58) Wang, X.; Gemayel, R.; Hayeck, N.; Perrier, S.; Charbonnel, N.; Xu, C.; Chen, H.; Zhu, C.; Zhang, L.; Wang, L.; Nizkorodov, S. A.; Wang, X.; Wang, Z.; Wang, T.; Mellouki, A.; Riva, M.; Chen, J.; George, C. Atmospheric Photosensitization: A New Pathway for Sulfate Formation. *Environ. Sci. Technol.* **2020**, *54* (6), 3114−3120.

(59) Savarino, J.; Thiemens, M. H. Analytical Procedure to Determine Both δ18O and δ17O of H2O2 in Natural Water and First Measurements. *Atmos. Environ.* **1999**, *33* (22), 3683−3690.

(60) Vicars, W. C.; Savarino, J. Quantitative Constraints on the 17O-Excess (Δ17O) Signature of Surface Ozone: Ambient Measurements from 50°N to 50°S Using the Nitrite-Coated Filter Technique. *Geochim. Cosmochim. Acta* **2014**, *135*, 270−287.

(61) Faust, B. C.; Anastasio, C.; Allen, J. M.; Arakaki, T. Aqueous-Phase Photochemical Formation of Peroxides in Authentic Cloud and Fog Waters. *Science* **1993**, *260* (5104), 73−75.

(62) Ye, C.; Chen, H.; Hoffmann, E. H.; Mettke, P.; Tilgner, A.; He, L.; Mutzel, A.; Brüggemann, M.; Poulain, L.; Schaefer, T.; Heinold, B.; Ma, Z.; Liu, P.; Xue, C.; Zhao, X.; Zhang, C.; Zhang, F.; Sun, H.; Li, Q.; Wang, L.; Yang, X.; Wang, J.; Liu, C.; Xing, C.; Mu, Y.; Chen, J.; Herrmann, H. Particle-Phase Photoreactions of HULIS and TMIs Establish a Strong Source of H_2O_2 and Particulate Sulfate in the Winter North China Plain. *Environ. Sci. Technol.* **2021**, *55* (12), 7818−7830.

(63) Harris, E.; Sinha, B.; Hoppe, P.; Ono, S. High-Precision Measurements of ^{33}S and ^{34}S Fractionation during SO_2 Oxidation Reveal Causes of Seasonality in SO_2 and Sulfate Isotopic Composition. *Environ. Sci. Technol.* **2013**, *47* (21), 12174−12183.

(64) Au Yang, D.; Bardoux, G.; Assayag, N.; Laskar, C.; Widory, D.; Cartigny, P. Atmospheric SO2 Oxidation by NO2 Plays No Role in the Mass Independent Sulfur Isotope Fractionation of Urban Aerosols. *Atmos. Environ.* **2018**, *193*, 109−117.

(65) Urey, H. C. The Thermodynamic Properties of Isotopic Substances. *J. Chem. Soc. Resumed* **1947**, 562.

(66) Sinha, B. W.; Hoppe, P.; Huth, J.; Foley, S.; Andreae, M. O. Sulfur Isotope Analyses of Individual Aerosol Particles in the Urban Aerosol at a Central European Site (Mainz, Germany). *Atmospheric Chem. Phys.* **2008**, *8* (23), 7217−7238.

(67) Jongebloed, U. A.; Schauer, A. J.; Hattori, S.; Cole-Dai, J.; Larrick, C. G.; Salimi, S.; Edouard, S. R.; Geng, L.; Alexander, B. Sulfur Isotopes Quantify the Impact of Anthropogenic Activities on Industrial-Era Arctic Sulfate in a Greenland Ice Core. *Environ. Res. Lett.* **2023**, *18* (7), 074020.

(68) Han, X.; Guo, Q.; Liu, C.; Fu, P.; Strauss, H.; Yang, J.; Hu, J.; Wei, L.; Ren, H.; Peters, M.; Wei, R.; Tian, L. Using Stable Isotopes to Trace Sources and Formation Processes of Sulfate Aerosols from Beijing, China. *Sci. Rep.* **2016**, *6* (1), 29958.

(69) Robinson, E. S.; Cesler-Maloney, M.; Tan, X.; Mao, J.; Simpson, W.; DeCarlo, P. F. Wintertime Spatial Patterns of Particulate Matter in Fairbanks, AK during ALPACA 2022. *Environ. Sci. Atmospheres* **2023**, *3* (3), 568−580.

(70) Broecker, W. S.; Oversby, V. M. *Chemical Equilibria in the Earth*; International Series in the Earth and Planetary Sciences; McGraw-Hill: New York, 1971.

(71) Salvatier, J.; Wiecki, T. V.; Fonnesbeck, C. Probabilistic Programming in Python Using PyMC3. *PeerJ. Comput. Sci.* **2016**, *2*, No. e55.

(72) Lee, C. C.-W.; Savarino, J. H.; Cachier, H.; Thiemens, M. H. Sulfur (32S, 33S, 34S, 36S) and Oxygen (16O,17O,18O) Isotopic Ratios of Primary Sulfate Produced from Combustion Processes. *Tellus B* **2002**, *54* (3), 193−200.

(73) Homolya, J. B.; Lambert, S. Characterization of Sulfate Emissions from Nonutility Boilers Firing Low-S Residual Oils in New York City. *J. Air Pollut. Control Assoc.* **1981**, *31* (2), 139−143.

(74) Linak, W. P.; Miller, C. A.; Wendt, J. O. L. Comparison of Particle Size Distributions and Elemental Partitioning from the Combustion of Pulverized Coal and Residual Fuel Oil. *J. Air Waste Manag. Assoc.* **2000**, *50* (8), 1532−1544.

(75) Homolya, J. B.; Fortune, C. R. The Measurement of the Sulfuric Acid and Sulfate Content of Particulate Matter Resulting from the Combustion of Coal and Oil. *Atmospheric Environ. 1967* **1978**, *12* (12), 2511−2514.

(76) Hays, M. D.; Beck, L.; Barfield, P.; Lavrich, R. J.; Dong, Y.; Vander Wal, R. L. Physical and Chemical Characterization of Residential Oil Boiler Emissions. *Environ. Sci. Technol.* **2008**, *42* (7), 2496−2502.

Supporting information for

Primary Sulfate Is the Dominant Source of Particulate Sulfate During Winter in Fairbanks, Alaska

Allison Moon[a*], Ursula Jongebloed[a], Kayane K. Dingilian[b], Andrew J. Schauer[c], Yuk-Chun Chan[a], Meeta Cesler-Maloney[d], William R. Simpson[d], Rodney J. Weber[b], Ling Tsiang[a], Fouad Yazbeck[a], Shuting Zhai[a], Alanna Wedum[a], Alexander J. Turner[a], Sarah Albertin[e], Slimane Bekki[f], Joël Savarino[e], Konstantin Gribanov[g], Kerri A. Pratt[h], Emily J. Costa[h], Cort Anastasio[i], Michael O. Sunday[i], Laura M. D. Heinlein[i], Jingqiu Mao[d], Becky Alexander[a*]

[a] *Department of Atmospheric Sciences and* [c] *Department of Earth and Space Sciences, University of Washington, Seattle, Washington, 98195, United States*

[b] *School of Earth and Atmospheric Sciences, Georgia Institute of Technology, Atlanta, Georgia 30332, USA*

[d] *Department of Chemistry, Biochemistry, and Geophysical Institute, University of Alaska Fairbanks, Fairbanks, AK 99775-6160*

[e] *IGE, Univ. Grenoble Alpes, CNRS, INRAE, IRD, Grenoble INP, 38000 Grenoble, France*

[f] *LATMOS/IPSL, Sorbonne Université, UVSQ, CNRS, 75005 Paris, France*

[g] *Climate and Environment Physics Laboratory, Ural Federal University, 620002, Yekaterinburg, Russia*

[h] *Department of Chemistry & Department of Earth & Environmental Sciences, University of Michigan, Ann Arbor, Michigan 48109 USA*

[i] *Department of Land, Air, & Water Resources, University of California, Davis, CA 95616 United States*

*Email: allimoon@uw.edu, beckya@uw.edu

TABLE OF CONTENTS

1. Experimental methods

1.1 Filter sample collection and gas-phase observations in Fairbanks

Prior to the field campaign, filters were soaked for 3 hours in 18 MΩ-cm water with a ratio of 2 liters of water per filter. After soaking, filters were rinsed in a secondary bin before drying completely in a glassware oven at 60°C. Filters were then combusted at 500°C for 8 hours and stored wrapped in aluminum foil in air-tight polyethylene bags.

Exhaust from the TE-5170 was directed through a high-quality HEPA filter located approximately 3 m away from the TE-5170 flow inlet to ensure that its exhaust was not being sampled. The TE-5028 calibration kit with a digital manometer was used approximately every 240 hours of sampling and an $r^2 > 0.99$ was achieved for each flow rate calibration. Before each calibration, 1-min TE-5170 samples with no airflow through the filter were collected and used as blanks for filter analysis. Flow rates (m^3/min) were corrected for daily fluctuations in temperature (1-min resolution averaged to 1-hr) and atmospheric pressure (1-min resolution averaged to 1-hr) and used to calculate the total air volume collected for each sample. Size-resolved bins were determined by calculating the particle size cut-off (*Dp,50*) at 50% collection efficiency using the corrected flow rate in each sample (equation S1). Equation S1 shows the calculation of particle size cut-offs:

$$Dp{,}50 = \sqrt{St} \cdot w \cdot \frac{\sqrt{(9 \cdot n \cdot L)}}{C \cdot Pp \cdot Q} \qquad \textbf{(S1)}$$

Where *St* is Stoke's number, which depends on jet throat length and jet Reynold's number, *w* is slot width (cm), *n* is gas viscosity (1.8×10^{-4} gm cm^{-1} sec-1 at 25 ˚C, 760 mmHg), *L* is slot length (cm), *Pp* is particle mass density (gm cc^{-1}), *C* is cunningham slip correction (*C*=1 for large *Dp*), and *Q* is flow rate (CFM) (Table S1). The average daily flow rate (*Q*) was calculated as the average flow rate per minute multiplied by the number of minutes. The total sample volume that resulted was also used to calculate the ambient concentrations of sulfur species after filter measurement via ion chromatography. Filters were combined to form three-size bins: particles < 0.7 µm ($PM_{0.7}$), 0.7-2.5 µm ($PM_{0.7\text{-}2.5}$), and 2.5-10 µm ($PM_{2.5\text{-}10}$) (Figure S1).

Table S1. Particle size cut-off variables used in equation S1

Stage	St	W	n	L	Pp	C
1	0.6	0.396	0.00018	11.049	1	1.02
2	0.58	0.163	0.00018	13.77	1	1.06
3	0.52	0.0914	0.00018	12.3952	1	1.11
4	0.69	0.0457	0.00018	12.3952	1	1.17

In-situ gas phase SO_2 (Thermo Scientific 43C) and O_3 (Thermo Scientific 49C) were measured from an inlet at 3m above the valley floor at the CTC site. The in-situ analyzers were both calibrated roughly weekly using an EPA certified mixed standard of 5.190 millimol mol^{-1} SO_2 that was diluted with an Environics 9100 calibration system to cover the ambient SO_2 mixing ratio range (from zero to ~125 nmol mol^{-1}). The same calibrator generated O_3 for calibration of the O_3 analyzer (from zero to ~200 nmol mol^{-1}). Calibration standard gases were diluted in zero air and were delivered to the instruments at overflow during multi-point calibrations. The average instrument zero and a zero-intercept linear correlation slope were determined for each calibration and linearly interpolated temporally between calibrations as correction factors for the raw instrument measurements.

1.2 Ion chromatography to measure HMS, non-HMS S(IV) and SO_4^{2-}

Recent work has shown that hydroxymethanesulfonate (HMS) can contribute 25-30% of total sulfur by mass in cold, dark, and polluted conditions, and may have been mistaken for sulfate.[1–3] This is because most ion chromatography and mass spectrometry methods cannot tell HMS, non-HMS S(IV), and SO_4^{2-} apart due to instability in solution and matrix effects between sulfur species.[4–7] At pH > 6, HMS decomposes into sulfite and is rapidly oxidized to form sulfate.[1,3,6] This creates a positive measurement bias for sulfate in ion chromatographic methods with strongly basic eluents (e.g., KaOH, NaOH).[6]

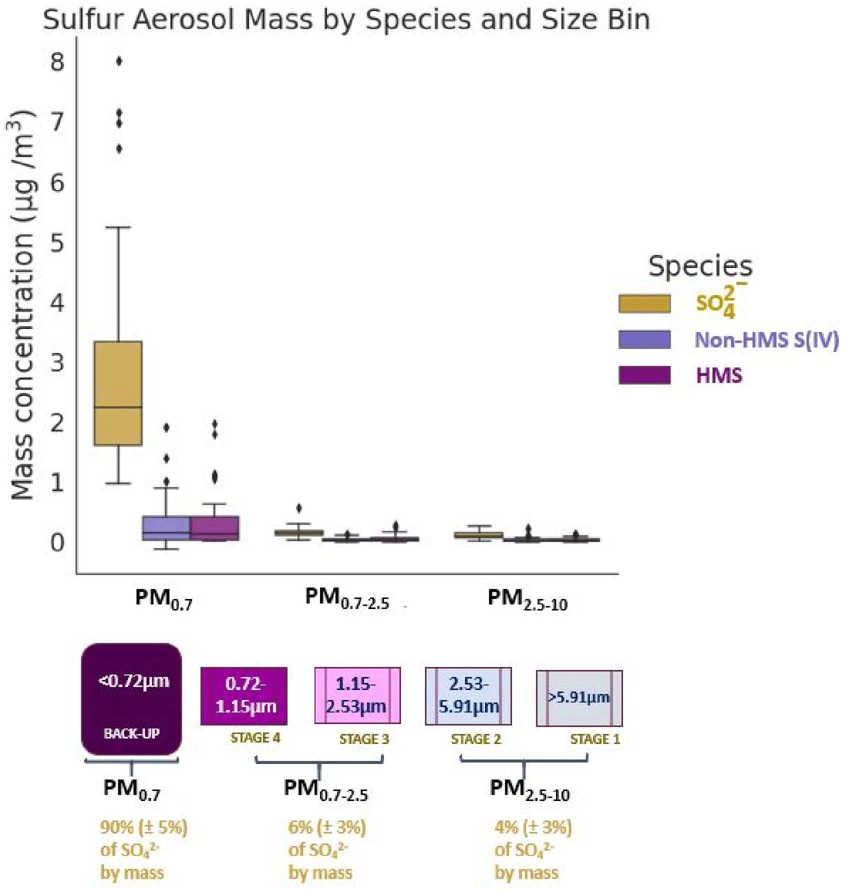

Figure S1. Average size cut-offs for the 4-stage cascade impactor and back-up filter. Filters were grouped into three size bins for isotope measurements: $PM_{0.7}$ for PM < 0.7µm (left), $PM_{0.7\text{-}2.5}$ for 0.7 < PM < 2.5µm (middle), and $PM_{2.5\text{-}10}$ for PM > 2.5 µm (right). Size resolved boxplots of SO_4^{2-} (gold), non-HMS S(IV) (blue), and HMS (purple) mass concentrations are shown along with outliers plotted as black diamonds.

Table S2: Sampling periods for $PM_{0.7\text{-}2.5}$ and $PM_{2.5\text{-}10}$ size bins

Period	Sample duration	Start date (MM/DD/YY) and local time	Stop date (MM/DD/YY) and local time
Period 1	24 hr	01/17/22 2:00 pm	01/24/22 9:00 am
Period 2	24 hr	01/24/22 9:30 am	01/29/22 9:00 am
Period 3 Polluted day	8 hr	01/29/22 9:30 am	02/02/22 5:00 pm
Period 4 Polluted night	16 hr	01/29/22 5:30 pm	02/03/22 9:00 am
Period 5	24 hr	02/03/22 9:30 am	02/06/22 9:00 am
Period 6	24 hr	02/06/22 9:30 am	02/09/22 9:00 am
Period 7	24 hr	02/09/22 9:30 am	02/13/22 9:00 am
Period 8	24 hr	02/13/22 9:30 am	02/17/22 9:00 am
Period 9	24 hr	02/17/22 9:30 am	02/18/22 9:00 am
Period 10	24 hr	02/21/22 9:30 am	02/26/2022 9:00 am
PF220208	7 days		
PF220221	7 days		

Dates of blanks collection (MM/DD/YY): 01/25/22, 02/02/22, 02/8/22, 02/20/22.

1.3 Isotopic analysis

1.3.1 Oxygen isotope measurements

For isotope analysis at the University of Washington IsoLab, filter samples (including blank filters collected in Fairbanks) were extracted into 18 MΩ-cm water and then filtered through a 0.2μm Polyethersulfone (PES) syringe filter to remove insoluble species. The filtrate was neutralized by converting the anions to sodium-form with an offline cation-exchange resin (AG 50W-X8 Resin from Bio-Rad) before removing organics from the sample matrix by adding 30% H_2O_2 and drying in a MiVac Duo concentrator as described in Schauer et al. (2012).[8] To isolate sulfate ions from the inorganic mixture, samples were rehydrated and pre-concentrated in a Dionex 4 x 50mm Ionpac AS19 guard column before being pumped into a Dionex ICS-2000 as described in Geng et al. (2013).[9] A 60-minute multi-step eluent gradient of KOH (5mM, 10mM, 15mM, 25mM) separated anions through a 4mm Dionex IonPac AS19 analytical column and Dionex ADRS 600 4mm suppressor at a flow rate of 1 mL/min. Sulfate fractions were isolated with a Foxy

Jr. fraction collector using automated peak detection software. Blanks received identical treatment in all sample preparation through the ion separation step. Sulfate measured in the Dionex ion chromatograph for the blank filters collected in Fairbanks was far below the detection limit for both mass spectrometers, suggesting that any minor contamination of sulfate during sample preparation could not alter the isotopic composition of the samples.

All isotope samples were prepared for silver salt pyrolysis using Ag^+-charged cation-exchange resin to convert sulfate to $Ag_2SO_{4,}$ as described in Geng et al. (2013).[9] Sulfur and oxygen isotope measurements were obtained by splitting each sample into two separate containers, silver capsules for sulfur isotopes and quartz cups for oxygen isotopes, drying the samples in the capsules to form solid Ag_2SO_4, and measuring both on the same day. Oxygen isotope measurements were performed on a Finnegan MAT 253 isotope ratio mass spectrometer using the silver salt pyrolysis technique as detailed in Schauer et al. (2012) and Geng et al. (2013).[8,9] Briefly, Ag_2SO_4 in quartz capsules is pyrolyzed at 1000˚C in a Temperature Conversion/Elemental Analyzer (TC/EA) with a helium gas carrier flow rate of 30 mL/min to form Ag(s), SO_2(g), and O_2(g). SO_2 gas is sequestered in a stainless-steel trap submerged in liquid nitrogen while non-condensable gasses are separated with a 3-m gas chromatography column. A substantial flow rate reduction in a gasbench allows for *m/z* isotope measurements of $^{32}O_2$, $^{33}O_2$, and $^{34}O_2$ gas following VSMOW-calibrated reference gas measurements prior to every sample peak. $\delta^{18}O$ and $\delta^{17}O$ are calculated as:

$$\delta^{x}O = \frac{R^{x}_{SA}}{R^{x}_{VSMOW}} - 1 \tag{2}$$

where R^{x}_{SA} is the ${}^{x}O/{}^{16}O$atomic abundance ratio of the sample, R^{x}_{VSMOW} is the same ratio of Vienna Standard Mean Ocean Water (VSMOW), and x = 17 or 18. $\Delta^{17}O$ is calculated with equation 1 in the main text. $\delta^{18}O$ and $\Delta^{17}O$ measurements obtained in quartz capsules were corrected for isotopic exchange with quartz using known values for oxygen isotope exchange during pyrolysis, which was constrained in prior work by Schauer et al. (2012) and replicated here (equations S3 and S4 from Figure S2).

$$\delta^{18}\mathrm{Ogold} \; = \; (\delta^{18}\mathrm{Oquartz} * 1.06) - 1.00 \tag{3}$$

$$\Delta^{17}\mathrm{Ogold} \; = \; (\Delta^{17}\mathrm{Oquartz} * 1.18) + 0.06 \tag{4}$$

$$\text{where } (\Delta^{17}\mathrm{Oquartz} \; = \delta^{17}\mathrm{Oquartz} - 0.52 * \delta^{18}\mathrm{Oquartz})$$

Isotope standards included an IAEA-N-1 stable isotope reference material for $\delta^{18}O$, an isotopically uniform selenite sample, three inter-laboratory calibrated $\Delta^{17}O$ standards (Sulf-α, Sulf-β, and Sulf-ε), and five newly synthesized standards (s-bravo, s-charlie, s-delta, s-echo, and s-foxtrot) prepared at the University of Washington.[9] The five new standards were synthesized to replenish supply of standards and are published here for posterity. Five new standards (s-bravo, s-charlie, s-delta, s-echo, and s-foxtrot) were synthesized and incorporated in the quartz capsule corrections for the $\delta^{18}O$ and $\Delta^{17}O$ measurements. Briefly, 12.5 g of reagent Na_2SO_3 was dissolved in a 100 mL volumetric flask with 3.5, 7.5, 12, 25, and 50 mL of ^{17}O-enriched water (20 μL of 90% ^{17}O water diluted to 1 L from Cambridge Isotope Laboratories, Andover, MA, USA), respectively. Solutions were left to equilibrate overnight before H_2O_2 was added the next afternoon in a fume hood. Solutions were stirred in a fume hood for 24 hours and placed in a 60°C oven until all water evaporated and the product Na_2SO_4 was crystallized. Standards were ground with a mortar and pestle and stored in a desiccator. The measured $\delta^{18}O$ and $\Delta^{17}O$ values in quartz and gold are shown in Table S3 A correction for oxygen isotopic exchange with quartz was performed for the raw measured values of $\delta^{18}O$ using 11 standards analyzed in both quartz and gold cups (Figure S2). The new corrections for isotopic exchange with quartz compared well with previous values from Schauer et al. (2012) and are plotted together in figure S2(a-b).[8]

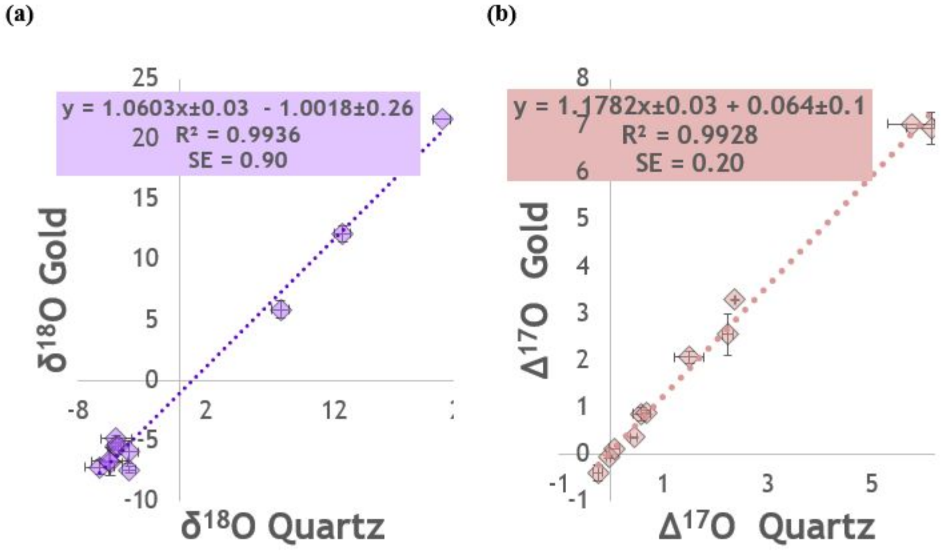

Figure S2(a) Average $\delta^{18}O$ measurements in quartz and gold capsules for each standard. The regression equation used for $\delta^{18}O$ quartz correction is shown in inset. **(b)** Average $\Delta^{17}O$ measurements in quartz and gold capsules for each standard. The regression equation used for $\Delta^{17}O$ quartz correction is shown in inset.

Table S3. Average measured $\delta^{18}O$ and $\Delta^{17}O$ values for standards and one sample used for corrections for oxygen isotopic exchange with quartz during Ag_2SO_4 pyrolysis.

Standard	$\delta^{18}O_{quartz}$ (±σ)	$\delta^{18}O_{gold}$ (±σ)	$\Delta^{17}O_{quartz}$ (±σ)	$\Delta^{17}O_{gold}$ (±σ)
sulf-alpha	-6.25 (±1.2)	-7.16 (±0.60)	0.59 (±0.16)	0.86 (±0.15)

sulf-beta	-5.41 (±0.90)	-6.78 (±1.1)	1.5 (±0.28)	2.07 (±0.12)
sulf-epsilon	-5.52 (±1.40)	-6.71 (±1.2)	5.76 (±0.44)	7.04 (±0.17)
selenite	12.65 (±0.66)	12.18 (±0.66)	-0.04 (±0.04)	-0.06 (±0.04)
IAEA-N-1	7.83 (±0.68)	5.88 (±0.73)	-0.25 (±0.09)	-0.39 (±0.18)
s-bravo	-4.97 (±1.23)	-4.83 (±0.29)	0.44 (±0.07)	0.36 (±0.01)
s-charlie	-4.98 (±0.62)	-5.48 (±0.31)	0.67 (±0.09)	0.89 (±0.04)
s-delta	-3.95 (±0.51)	-7.39 (±0.24)	2.24 (±0.11)	2.55 (±0.45)
s-echo	-4.81 (±0.21)	-5.44 (0.67)	2.38 (±0.02)	3.29 (±0.05)
s-foxtrot	-4.01 (±0.77)	-5.89 (±0.94)	6.14 (±0.46)	6.95 (±0.34)
A220130	20.41 (±0.68)	21.65	0.07 (±0.1)	0.12

1.3.2 Sulfur isotope measurements

Sulfur isotope composition ($^{64}SO_2$ and $^{66}SO_2$) was measured using a separate Finnegan MAT 253 isotope ratio mass spectrometer with the same configuration as Jongebloed et al. (2023).[10] To optimize combustion yield, the silver capsules were folded and packed with vanadium pentoxide and elemental tin powder before being converted to SO_2(g) in the Thermo Scientific high-temperature conversion elemental analyzer (TC/EA). δ^{34}S is calculated as:

$$\delta^{34}S = \frac{R^{34}_{SA}}{R^{x}_{VCDT}} - 1 \tag{5}$$

where R^{34}_{SA} is the $^{34}S/^{32}S$ ratio of the sample, R^{x}_{VCDT} is the same ratio of Vienna Canyon Diablo Troilite (VCDT). δ^{34}S values were normalized to the VCDT scale using four in-house reference materials that are regularly calibrated against the international reference materials IAEA-S-1, IAEA-S-3, and NBS-127. The analytical error of the measurements estimated from duplicate sample analysis (performed on 30% of Fairbanks samples) and replicate measurements of standards in quartz and silver capsules was: ± 0.6‰, ± 0.2‰, and ± 0.8‰ for δ^{18}O, Δ^{17}O, and δ^{34}S, respectively. The fully propagated error including isotopic corrections for the three measurements are as follows: δ^{18}O (± 1.9‰), Δ^{17}O (± 0.4‰), and δ^{34}S (± 1.2‰).

Sulfur isotopic composition of residential home heating oils #1 and #2 purchased in Fairbanks was measured using the configuration from Jongebloed et al. (2023) with one modification: vanadium pentoxide was not packed in the tins with the sample because the fuel oil did not need an additional oxygen source.[10] 6μL of fuel oil was added to a 50 μL tin capsule packed with tin powder. Caution should be used when measuring $\delta^{34}S(S)$ using this method because fuel oil is flammable, resulting in explosive combustion in the TC/EA. . $\delta^{34}S(S)$ values are reported in Table S4 along with the fractional use of each fuel type in FNSB and the sulfur content of both heating oils. This yields a $\delta^{34}S(S)$ signature of 4.7±0.6‰, which was used as an emissions signature in the isotope mixing model.

Table S4. $\delta^{34}S(S)$ measurement of Fairbanks fuel oil

Fuel oil Type	Sulfur content (ppmv)	Quantity of fuel oil combusted	Fraction of total fuel oil used in Fairbanks (ADEC, 2019)	Estimated contribution to fuel oil-derived sulfur based on sulfur content and domestic use	Measured $\delta^{34}S(S)$	**Weighted average $\delta^{34}S(S)$**
Fuel oil #1	896	6 μL	33%	15%	3.7±0.6‰	**4.7±0.6‰**
Fuel oil #2	2,566	6 μL	67%	85%	4.9±0.1‰	

1. 4 HMS and non-HMS S(IV) correction for $\delta^{18}O$, $\Delta^{17}O$, and $\delta^{34}S$ isotope measurements

1. 4.1 HMS and non-HMS S(IV) correction for oxygen isotopes

HMS decomposes in non-acidic conditions and thus during ion chromatography using basic eluants (e.g., KOH as used in this study).[1,6,11] Prior to the ion chromatography step, HMS is known to decompose to formaldehyde and bisulfite during sample storage and as it is extracted in water in an equilibrium reaction (scheme 1 from Figure S3).[1,2,6] Furthermore, in this method, the sample matrix is immediately neutralized in the offline cation-exchange step by stripping the anions of hydrogen ions and replacing them with sodium ions (section I.3). The 60-minute multi-step eluent gradient of KOH (5mM, 10mM, 15mM, 25mM) used in the IC separation step further induces HMS decomposition.

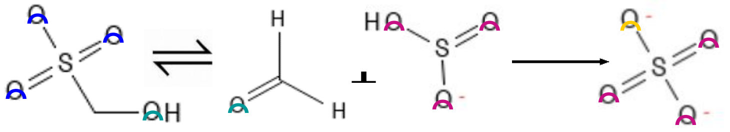

$$HOCH_2SO_3 \rightleftharpoons HCHO + (H)SO_3^- \rightarrow SO_4^{2-} \qquad \textbf{(Scheme 1)}$$

Figure S3. Decomposition of hydroxymethanesulfonate ($HOCH_2SO_3$) during sample preparation. HMS formed in Fairbanks has three oxygens from dissolved S(IV) (blue) and one oxygen from HCHO (green). S(IV) formed during decomposition of HMS in the laboratory equilibrates with laboratory water (pink) before it obtains its forth oxygen (yellow) from either dissolved O_2 or H_2O_2, depending on when the HMS decomposes (before or after addition of H_2O_2).

Laboratory experiments were performed to determine whether the neutralization step induces further HMS decomposition in addition to the IC separation step first observed by Dovrou et al (2019).[6] Three solutions were tested: 100% HMS (2μmol HMS dissolved in 10mL Milli-Q), 50% HMS, 50% Na_2SO_4 (1μmol HMS + 1μmol $Na_2SO_4^{2-}$ dissolved in 10mL Milli-Q), and 100% SO4 (2μmol $Na_2SO_4^{2-}$ dissolved in 10mL Milli-Q). The neutralized samples were prepared by dissolving the reagents $HOCH_2SO_3Na$ and Na_2SO_4 in laboratory water, converting the solutions to sodium form as described in section S1.3, and then measuring them on the IC with the 60-minute multi-step eluent gradient detailed above. The non-neutralized samples were prepared by dissolving the reagents and measuring them on the IC with the same eluent gradient but without the neutralization step. Solution preparation and IC measurement were performed on the same day to be consistent with field sample extraction. The percent yield of sulfate formed from decomposition of HMS during IC increased for all the neutralized HMS-containing samples relative to the non-neutralized samples, signifying that neutralization prior to IC analysis further facilitates HMS decomposition (Figure S4). The mixture with 50% HMS and 50% sulfate had an

IC yield consistent with sulfate alone, indicating complete decomposition of HMS followed by conversion of S(IV) to sulfate (Figure S4).

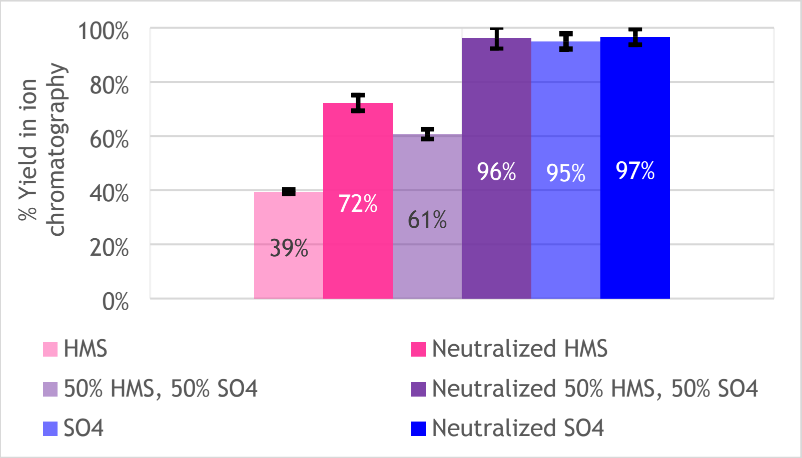

Figure S4. Average percent yield of sulfate measured via ion chromatography with two sample treatments: one where solutions (100% HMS, 50% HMS and 50% SO_4^{2-} , and 100% SO_4^{2-}) are prepared and then measured on the IC and the other where solutions are prepared and the sample is converted to sodium form before being measured on the IC. The error bars are the standard deviation of the percent yield from 3 measurements for each experimental treatment.

Non-HMS S(IV) species (HSO_3^- and SO_3^{2-}) are converted to sulfate when dissolved in water and oxidized by H_2O_2. Laboratory tests with synthetic mixtures of HMS and S(IV) confirm that both of these species are converted to sulfate during sample processing. Thus, the isotopic composition of the sulfate measured is the isotopic composition of the combined sulfate, HMS, and non-HMS

S(IV) in each sample. To obtain the isotopic composition of sulfate in the samples apart from HMS and S(IV), we corrected the isotope measurements using the measured fraction of HMS and non-HMS S(IV) species relative to sulfate as described below. Sulfate formed from HMS decomposition and S(IV) oxidation has $\Delta^{17}O = 0‰$ because the oxygen atoms of sulfite and bisulfite exchange with water and a fourth oxygen atom is added from the oxidation of S(IV) to sulfate after adding synthetic H_2O_2 (i.e., not formed in the atmosphere) to solution.[12] $\Delta^{17}O$ measurements were corrected by dividing the measured $\Delta^{17}O$ value by the fraction of sulfate in each sample, which were measured at Georgia Tech and described in section 1.2 (equations S6 and S7).

$$\Delta^{17}O\left(SO_4^{2-}\right)_{\text{measured}} = f_{SO_4} \cdot \Delta^{17}O_{SO_4} + f_{S(IV)} \cdot \Delta^{17}O_{S(IV)} + f_{HMS} \cdot \Delta^{17}O_{HMS} \quad (6)$$

$$\text{where } \Delta^{17}O_{S(IV)} = \Delta^{17}O_{HMS} = 0 \text{ and } f_{SO_4} + f_{S(IV)} + f_{HMS} = 1$$

$$\Delta^{17}O\left(SO_4^{2-}\right) = \Delta^{17}O\left(SO_4^{2-}\right)_{\text{measured}} / f_{SO_4} \quad (7)$$

The $\delta^{18}O$ of non-HMS S(IV) from the Fairbanks filter samples undergoes oxygen isotopic exchange with lab water after dissolution and during sample processing. This means that its oxygen isotopic composition will be independent of the source of S(IV) and instead is determined by the oxygen isotopic composition of lab water and the oxidants present during sample processing. Laboratory tests using dissolved reagent grade Na_2SO_3 and subjecting it to full sample processing yielded $\delta^{18}O$ = -1.1± 0.2‰ (n = 3). This value is used in equation 8 to correct the $\delta^{18}O$ measurements.

In non-acidic conditions, HMS decomposes in an equilibrium reaction into HCHO and $(H)SO_3^-$ (scheme 1 in Figure S3).[13] The HSO_3^- then equilibrates with the laboratory water, and the $\delta^{18}O$ of the resulting sulfate depends on whether the HSO_3^- is oxidized by H_2O_2 or O_2. Full-process treatment of HMS yielded $\delta^{18}O = 4.1 \pm 2.0‰$ (n = 4), indicating that the sulfate that results from decomposed HMS is more enriched than non-HMS S(IV) during the sample preparation process. We hypothesize that S(IV) resulting from HMS decomposition after the H_2O_2 oxidation step (e.g., during IC separation) is oxidized by isotopically heavy atmospheric molecular oxygen catalyzed by trace metals in the samples. Thus, this more enriched value is used to correct the $\delta^{18}O$ measurements in equation 8.

We prepared full-process standards with ratios of HMS, S(IV), and SO_4^{2-} similar to our observations in Fairbanks (Figure S5). The measured $\delta^{18}O$ and $\Delta^{17}O$ of these mixtures are linearly proportional and reflect the amount of HMS and S(IV) in the sample ($r^2 = 0.9968$). This is consistent with the mechanism shown in Figure S3 and the experiment shown in Figure S4 where it was determined that HMS undergoes total decomposition during the sample preparation process.

Most importantly, the relationship between $\delta^{18}O$ and $\Delta^{17}O$ is linear regardless of the amount of S(IV) and HMS within the mixture. This suggests that differences in the equilibrium reaction of HMS due to varying concentrations does not elicit a detectable effect on $\delta^{18}O$ and $\Delta^{17}O$ composition. Equation S8 was used to correct $\delta^{18}O(SO_4^{2-})_{measured}$ values for S(IV) and HMS to yield the $\delta^{18}O$ of sulfate $\delta^{18}O(SO_4^{2-})$ (equation S9).

$$\delta^{18}O(SO_4^{2-})_{measured} = f_{SO_4} \cdot \delta^{18}O_{SO_4} + f_{S(IV)} \cdot \delta^{18}O_{S(IV)} + f_{HMS} \cdot \delta^{18}O_{HMS} \quad \textbf{(8)}$$

where $\delta^{18}O_{S(IV)} = -1.1‰$ and $\delta^{18}O_{HMS} = 4.1‰$

$$\delta^{18}O(SO_4^{2-}) = \delta^{18}O(SO_4^{2-})_{measured} / f_{SO_4} \quad \textbf{(9)}$$

The total fraction of S(IV) and HMS in the samples collected in Fairbanks ranged from 0-17% and 0-20%, respectively, for $PM_{0.7}$ particles and 7-34% and 4-27%, respectively, for $PM_{>0.7}$ particles. The maximum fraction of HMS + S(IV) occurred during the highly polluted period from Jan 31st - Feb 3rd. Fractions outside of the polluted period ranged from 0-10% for S(IV) and 0-11% for HMS for $PM_{0.7}$ particles and 7-34% for S(IV) and 0-20% for HMS for $PM_{>0.7}$ particles. During the polluted period the $\delta^{18}O$ correction for combined S(IV) and HMS ranged between -0.54 and 0.81‰. For the rest of the campaign the correction for combined S(IV) and HMS ranged between -0.7 and 0.6‰. The $\delta^{18}O$ corrections for S(IV) and HMS throughout the campaign are smaller than our propagated error in $\delta^{18}O$ (±1.9‰).

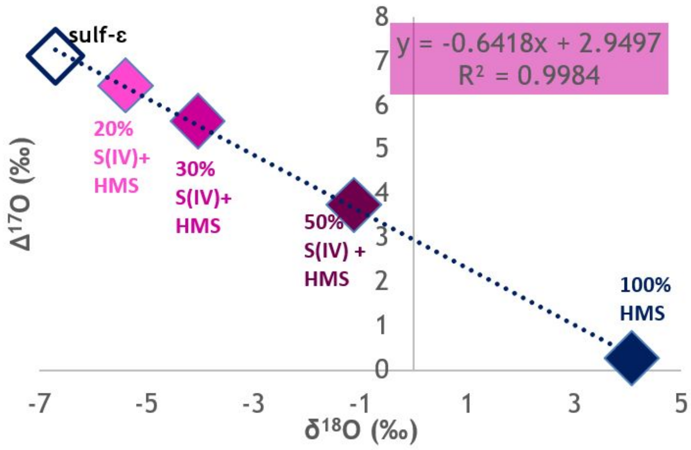

Figure S5. Measured $\Delta^{17}O$ and $\delta^{18}O$ of different mixtures of sulfate (sulf-e standard) and equal amounts of HMS and S(IV). The oxygen isotopic composition of sulf-e is shown in Table S3. All four mixtures were treated with the full sample preparation process (converted to sodium-form, treated twice with H2O2, and measured via IC) before the isotopic composition was measured. The molar fractions in the standards prepared are as follows:

(1) Sulf-e = 100% sulf-e;

(2) 20% S(IV) + HMS = 10% S(IV) + 10% HMS + 80% sulf-e;

(3) 30% S(IV) + HMS = 15% S(IV) + 15% HMS + 70% sulf-e;

(4) 50% S(IV) + HMS = 25% S(IV) + 25% HMS + 50% sulf-e;

(5) 100% HMS

1. 4.2 HMS and non-HMS S(IV) correction for sulfur isotopes

We assume negligible isotopic fractionation during high-temperature combustion of fuel oil so that $\delta^{34}S(SO_2)$ and $\delta^{34}S$ of primary sulfate are equal to our direct measurements of fuel oil (+4.7±0.6‰). Potential fractionation of $\delta^{34}S$ during the conversion of HSO_3^- and SO_3^{2-} to HMS is unknown. Figure S6 shows $\delta^{34}S$ values of sulfate prior to being corrected for the fraction of non-HMS S(IV) and HMS in each sample. $\delta^{34}S$ of $PM_{0.7}$ during the polluted period between January 30th and February 3rd (where the temperature ranged between -25 to -30 ˚C) increases as the fractions of HMS and non-HMS S(IV) both increase. Figures S7(a-b) and S8 show that when the fraction of HMS + S(IV) is the highest, $\delta^{34}S$ is the most enriched. Moreover, the slope, intercept, and r^2 of the $PM_{0.7}$ regression in Figure S7(a) is consistent with the regression with $PM_{0.7}$, $PM_{0.7-2.5}$, and $PM_{2.5-10}$ $\delta^{34}S$ in Figure S7(b). Since these size bins have very different fractions of secondary sulfate, this consistency shows that the degree of $\delta^{34}S$ enrichment is related the fraction of non-HMS S(IV) and HMS within each sample.

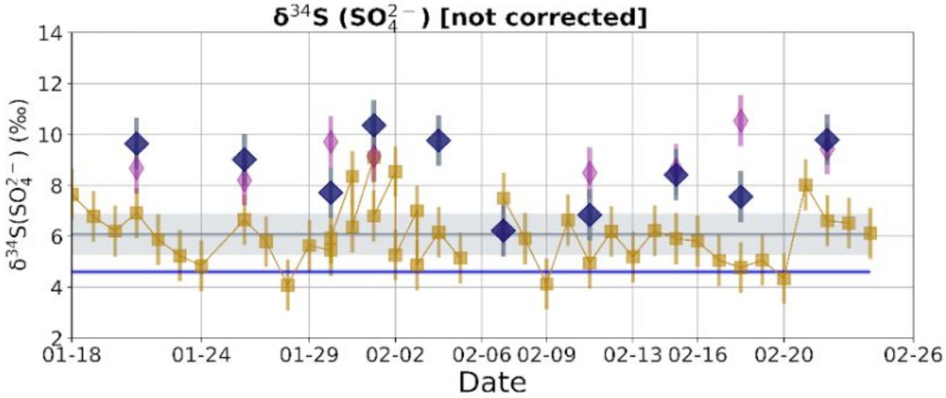

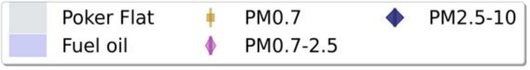

Figure S6. Time series of δ^{34}S that is not corrected for HMS+ non-HMS S(IV). Measurements are divided into three size bins: PM$_{0.7}$ (<0.7 μm) as squares, PM$_{2.5}$ (0.7-2.5 μm) as narrow diamonds, and (PM$_{2.5-10}$) (>2.5 μm) as wide diamonds. Daily PM$_{0.7-2.5}$ and PM$_{2.5-10}$ samples were combined into 10 periods as indicated by the vertical gridlines. A 2-week average of isotopic composition at Poker Flat is shown by the gray shading in a–c. The measured δ^{34}S source signature for Fairbanks fuel oil is shown by the blue line in c.

According to the principles of Rayleigh distillation, both lower temperatures and lower sulfur oxidation ratios will lead to larger δ^{34}S fractionation.[14] Both of these factors could theoretically lead to enrichment in δ^{34}S due to secondary oxidation being more pronounced during the polluted period, though it is also possible that the formation of sulfate from non-HMS S(IV) or HMS are responsible for this enrichment. δ^{18}O of PM$_{0.7}$ samples during the polluted period shows a very small contribution from secondary sulfate (11-33%), as evidenced by the high δ^{18}O observations (16.2±3.1‰) and model predictions detailed in section II.2 (Figure 1 in the main text). Simultaneously, Δ^{17}O values are at their lowest for the PM$_{0.7}$ size bin during this period (Figure S8), signifying secondary sulfate formation from O$_3$ and H$_2$O$_2$ oxidation (oxidants known to induce the largest enrichment in sulfur isotopes) are unlikely to explain the large $\delta^{34}S$ enrichment during the polluted period. This is reinforced by considering that the sulfur oxidation ratios are comparable to other periods during the campaign (Figure 1 in the main text) so fractionation due to varying SOR is unlikely to explain the $\delta^{34}S$ enrichment. Given the large contributions of non-HMS S(IV) and HMS and the small proportion of secondary sulfate during the polluted period, it is likely that the observed $\delta^{34}S$ enrichment is due to the sulfate formed from HMS and/or non-HMS S(IV) during sample processing. The fraction of HMS + non-HMS S(IV) to total sulfur species plotted in figure S7 is calculated using equation S10:

$$\text{Fraction non - HMS S(IV)} + \text{HMS} = \frac{[\text{HMS}] + [\text{non - HMS(IV)}]}{[\text{HMS}] + [\text{S(IV)}] + [\text{SO}_4^{2-}]} \quad \textbf{(10)}$$

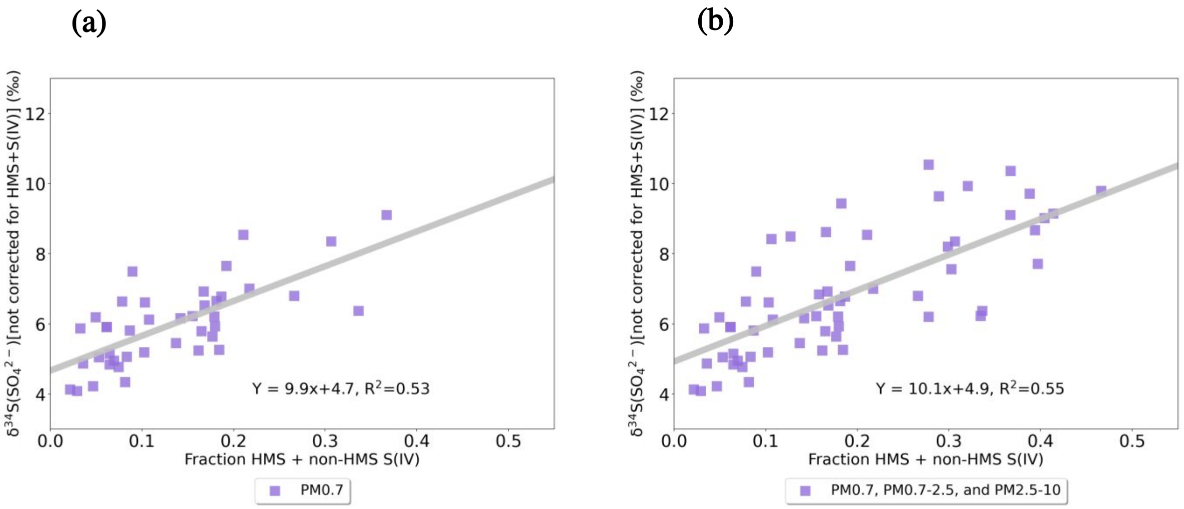

Figure S7. The relationship between the fraction of S(IV)+HMS in **(a)** PM$_{0.7}$and **(b)** PM$_{0.7}$, PM$_{0.7-2.5}$, and PM$_{2.5-10}$ .and δ^{34}S observations before HMS+S(IV) correction. The fraction of HMS+non-S(IV) is calculated with the according to equation S10.

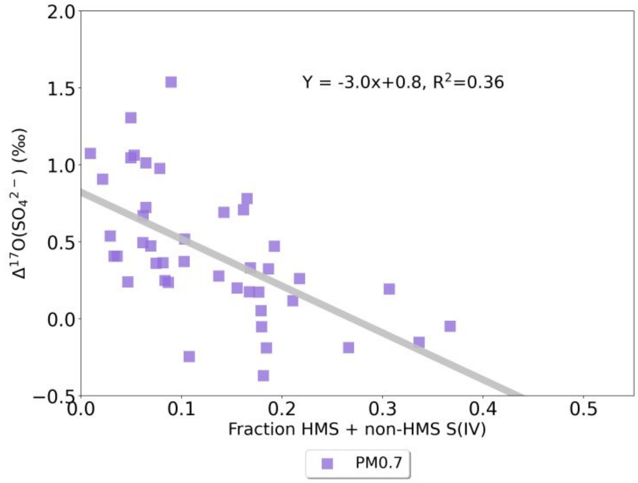

Figure S8. Relationship between $PM_{0.7}$ $\Delta^{17}O$ corrected for S(IV) and HMS and the fraction of S(IV) + HMS. The color bar indicates the average daily temperature in degrees Celsius. The fraction of HMS+S(IV) is calculated according to equation S10.

The difference between the modeled and observed $\delta^{34}S$ is linearly proportional to the fraction of HMS + non-HMS S(IV) ($R^2 = 0.59$, p-value <0.01) (Figure S9) The $PM_{0.7-2.5}$ and $PM_{2.5-10}$ values were not used to develop the correction equation because higher fractions of secondary sulfate in these samples make it difficult to disentangle the effects of $\delta^{34}S$ fractionation from secondary sulfate formation in the atmosphere vs. sulfate formed from HMS and non-HMS S(IV) during sample processing, though the relationship for the larger sample sizes is similar to $PM_{0.7}$.

The regression equation S11 from Figure S9 was used to determine the enrichment in $\delta^{34}S$ from decomposition of HMS and S(IV) in the samples:

$$\delta^{34}\mathrm{S}\left(\mathrm{SO}_4^{2-}\right)_{corr} = 7.3(\pm 0.60) \cdot f_{\mathrm{HMS+S(IV)}} - 1.3(\pm 0.14) \quad \textbf{(11)}$$

where $f_{HMS+S(IV)}$ is the measured fraction of HMS + S(IV) and $\delta^{34}S\left(SO_4^{2-}\right)_{corr}$ is the enrichment in $\delta^{34}S$ induced by the oxidation of S(IV) and HMS to sulfate. This assumes that the formation of sulfate from HMS and S(IV) during sample processing enriches measured $\delta^{34}S$ of sulfate relative to primary and secondary sulfate in the atmosphere. The enrichment during HMS formation alone cannot be quantitatively separated from total S(IV) as they are linearly proportional ($r^2 = 0.95$) (Figure S10). The error in the correction presented in Figure S9 was included in the fully propagated $\delta^{34}S$ error. The corrected $\delta^{34}S$ values were used as new inputs in the Bayesian mixing model to aid in estimates of the fractional contributions of different secondary sulfate formation pathways and are presented in Figures 1 and 2 of the main text.

Because total HMS and S(IV) concentrations relative to total sulfur aerosol are highest during the polluted period (11±3% and 27±6%, respectively), estimating the importance of the NO_2 and TMI-O_2 pathways based on the $\delta^{34}S$ measurements is most uncertain during this time period because the depletion in the $\delta^{34}S$ signature from these two reactions may be offset by enrichment from HMS + S(IV). This uncertainty does not substantially affect the findings of this paper as oxygen isotope measurements during the polluted period suggest that the TMI-O_2, NO_2, or OH pathways are not dominant contributors to sulfate composition (see section SII.2).

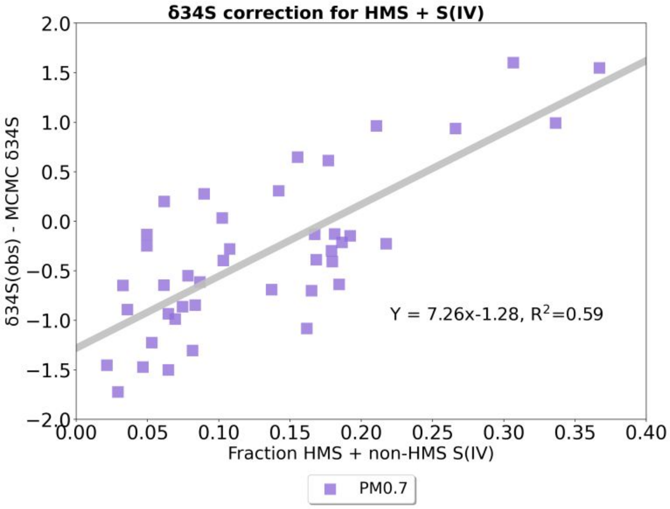

Figure S9. The difference between δ^{34}S(observations) and the MCMC δ^{34}S that was computed using the oxygen isotope observations, the average daily temperature, and the SOR versus the fraction of HMS + S(IV).

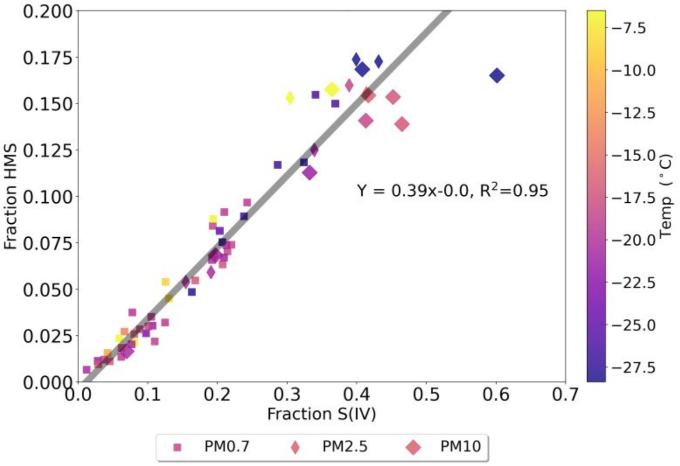

Figure S10. Relationship between the fraction of HMS and total S(IV) within each sample. The color bar shows the mean daily temperature during each sample collection in degrees Celsius.

2. Isotope observations during ALPACA

One challenge in using $\delta^{34}S(SO_4^{2-})$ to understand the sources and formation of atmospheric sulfate is that the fractionation due to secondary sulfate formation depends on the $\delta^{34}S(SO_2)$ signature, which may come from more than one source. While the measured $\delta^{34}S_{\text{fuel oil}}$ is a useful source signature of primary sulfate and fuel oil-derived SO_2, it's possible that enhanced vertical mixing, which is typically associated with warmer surface temperatures, may introduce coal-derived SO_2 to the surface. Furthermore, warmer temperatures reduce the need of fuel oil for home heating, so the relative ratios of the $\delta^{34}S(SO_2)$ signatures for fuel oil and coal may cause the source signature for coal to be important.

Figure S11 shows that there is no relationship between $\delta^{34}S$ and temperature, which indicates that coal-derived SO_2 does not induce a detectable effect in $\delta^{34}S$ composition, or that coal-derived SO_2 has a $\delta^{34}S$ value similar to fuel oil. If the $\delta^{34}S_{\text{emission}}$ signature is a mixture between coal and fuel oil-derived $SO_{2,}$ it would be most obvious during warmer periods when fuel oil consumption is lower and vertical mixing is higher.

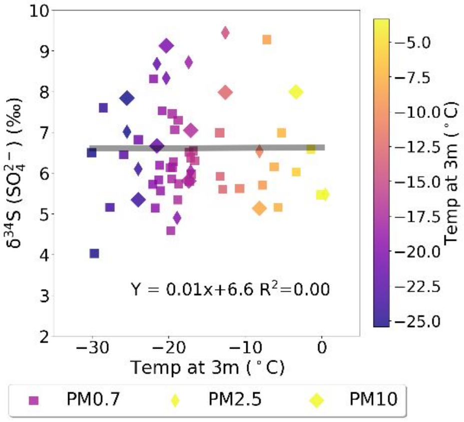

Figure S11. Relationship between $\delta^{34}S(SO_4^{2-})$ observations and temperature at 3m altitude in degrees Celsius.

Figure S12 shows that SO_2 and SO_4^{2-} concentrations are lower at temperatures >-18C. The difference in SO_2 and SO_4^{2-} concentrations during warmer periods is not reflected in the $\delta^{34}S(SO_4^{2})$ observations (Figure S11), signifying either that the sulfur isotope composition of coal-derived SO_2 is similar to fuel oil or that coal-derived SO_2 is not an important sulfur source at 3m.

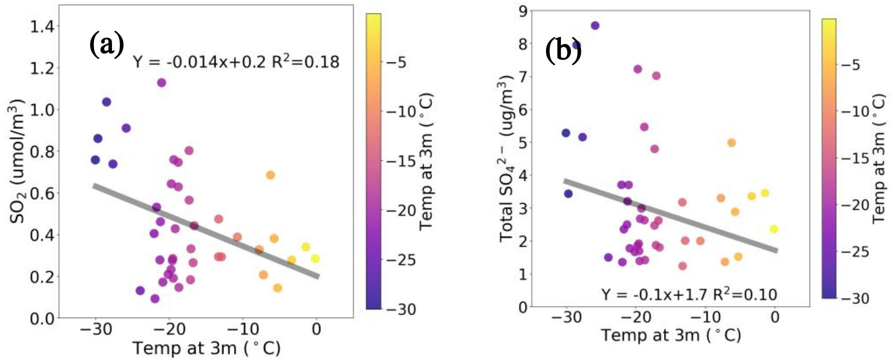

Figure S12. SO_2 **(a)** and SO_4^{2-} **(b)** observations versus temperature at 3m in degrees Celsius.

Figure S13 shows a positive relationship between SO_2 and SO_4^{2-} and no relationship between SO_4^{2-} and SOR. This is consistent with a regime dominated by primary sulfate, where sulfate concentrations are largely dependent on total emissions rather than atmospheric-chemistry driven oxidation of atmospheric SO_2.

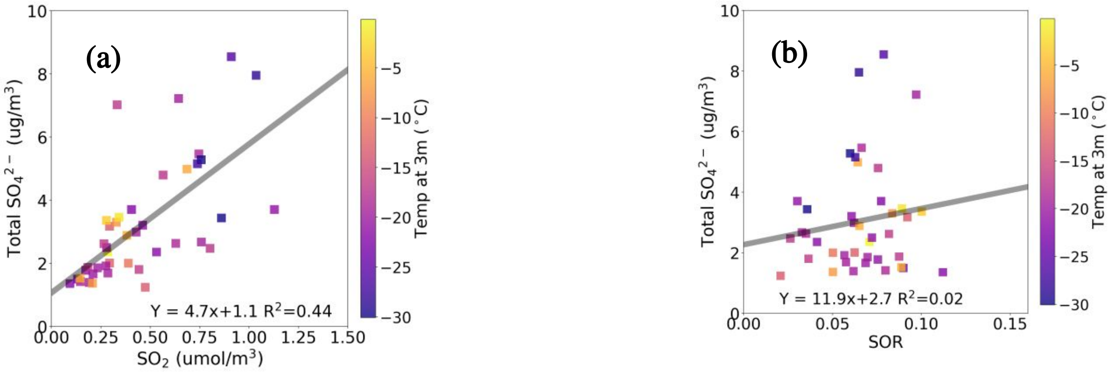

Figure S13. Relationship between observed SO_4^{2-} and SO_2 **(a)** and SOR **(b)**, where SOR is defined in equation 1 in the main text.

3. Bayesian Isotope Mixing Model Methods and Performance

3.1.1 $\delta^{18}O(H_2O_{(precip)})$ and $\delta^{18}O(H_2O_{(l)})$ estimates for Fairbanks

The $\delta^{18}O$ of Fairbanks snow $\delta^{18}O(H_2O_{(precip)})$ was measured throughout the campaign with an average value of -24.8‰ (Table S5).

Table S5. $\delta^{18}O$ measurements (‰) from Fairbanks snow samples and laboratory water.

Sample ID	$\delta^{18}O_{VSMOW}$ (‰)	$\delta^{18}O_{error}$ (‰)
CTC_ 220127 snow	-21.9	0.026
CTC_220127_snow	-21.65	0.011
CTC_220130_snow	-22.87	0.017
CTC_220131_snow	-26.16	0.016
CTC_220202_snow	-27.63	0.018
CTC_220204_snow	-23.63	0.025
CTC_220207_snow	-23.12	0.007
CTC_220209_snow	-26.66	0.018
CTC_220211_snow	-27.22	0.013
CTC_220214_snow	-24.28	0.021
isolab_a	-10.35	0.028
isolab_b	-10.29	0.022
isolab_c	-10.28	0.021
alexanderlab_a	-10.21	0.022
alexanderlab_b	-10.18	0.012
alexanderlab_c	-10.18	0.019
Average $\delta^{18}O$ Water Fairbanks	-24.767	0.018
Average $\delta^{18}O$ Water Lab	-10.248	0.021

A regression between the $\delta^{18}O(H_2O_{(precip)})$ observations in Table S5 and the average daily ambient temperature at 3 m altitude yielded an r^2 of (0.60) (Figure S14(a)). These observations were compared with historical precipitation data sourced from the IAEA Water Isotope system from Alaska and Western Canada between 1953-2023. The relationship between $\delta^{18}O(H_2O_{(precip)})$ and ambient temperature in this study is consistent with historical data for this region (Figure S14b)).

The regression equation from Figure S14(b):

$$\delta^{18}O(H_2O_{(precip)}) = 0.43 \cdot T - 17.22 \qquad \textbf{(12)}$$

where *T* is temperature in degrees Celsius was used to calculate $\delta^{18}O(H_2O_{(precip)})$ as a function of daily mean ambient temperature during filter sample collection. Equation 12 represents a source of uncertainty in calculating the source signatures of $\delta^{18}O$ oxidation, as the relationship between $\delta^{18}O(H_2O_{(precip)})$ and temperature was not directly measured for each sulfate sample. For a given temperature, the error in $\delta^{18}O(H_2O_{(precip)})$ is ±0.35‰, which is the error in the intercept of Figure S14(b).

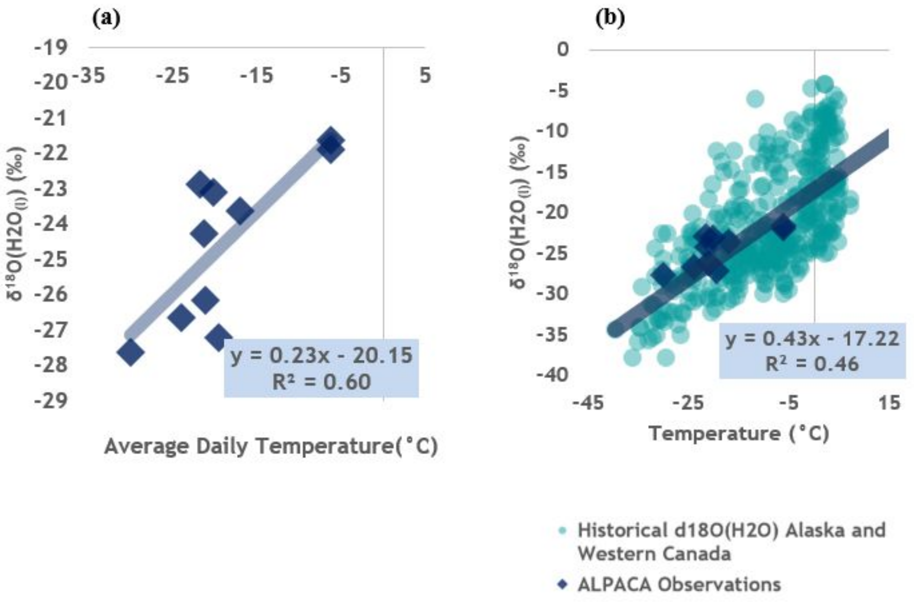

Figure S14. (a) $\delta^{18}O(H_2O_{(precip)})$ observations from Table S5 vs. the mean ambient temperature during sample collection in Fairbanks. The error bars for the $\delta^{18}O(H_2O_{(precip)})$ observations are smaller than the data points but are shown in Table S5. **(b)** $\delta^{18}O(H_2O_{(precip)})$ observations from Table S5 vs. the mean ambient temperature during sample collection plotted with historical precipitation data compiled from the IAEA water isotope system database from 1953-2023 from the Global Network of Isotopes in Precipitation (GNIP) Database accessible at: https://nucleus.iaea.org/wiser

Dissolved SO_2 equilibrates with liquid water so that the $\delta^{18}O(S(IV))$ signature is linearly dependent on the $\delta^{18}O$ of the solvent water ($r^2 = 0.992$) and more enriched by 7.8‰ on average (equation S13 from Figure S15).

$$\delta^{18}O(S(IV)) = 0.95 \cdot \delta^{18}O(H_2O_{(l)}) + 7.8 \quad \textbf{(13)}$$

Equation S13 was determined by using the observed relationship between δ^{18}O($H_2O_{(l)}$) and δ^{18}O (SO_4^{2-}) in laboratory experiments from Holt et al (1981) and correcting for the addition of one oxygen atom from molecular oxygen during metal-catalyzed oxidation of S(IV) to sulfate. For each sample in Fairbanks, equation S12 was used first to estimate the δ^{18}O($H_2O_{(precip)}$) as a function of average temperature during sample collection, and equation S13 was used to calculate the equilibrated δ^{18}O(S(IV)), assuming that the δ^{18}O($H_2O_{(precip)}$) is equal to the δ^{18}O($H_2O_{(l)}$) of aerosol water. This represents a source of uncertainty because the δ^{18}O($H_2O_{(l)}$) of aerosol water is unknown.

We dissolved reagent sodium sulfite (Na_2SO_3) in laboratory Milli-Q water (δ^{18}O($H_2O_{(l)}$)= -10.25‰ in Table S5) and measured the δ^{18}O(S(IV)) composition as described in section 1.4 but without adding H_2O_2. The resulting δ^{18}O(S(IV)) was -2.4‰. This is within analytical error (±0.8‰) of the expected δ^{18}O(S(IV)) value calculated from equation S13 (-1.9‰). Additionally, we hypothesized that the measured enrichment in δ^{18}O(HMS) (+4.1‰) was from metal-catalyzed oxidation of S(IV) via O_2 during sample processing (section I.4). Using the δ^{18}O(S(IV)) value from equation S13 and the δ^{18}O of molecular oxygen yielded 4.1‰ for δ^{18}O(HMS), which is the same as the measured value.

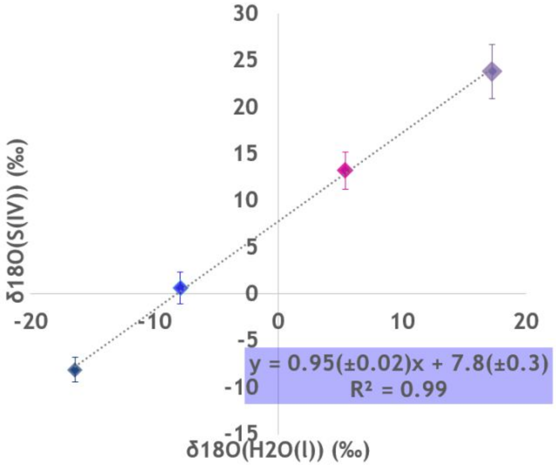

Figure S15. δ^{18}O(S(IV) as a function of the δ^{18}O of the solvent water (d18O(H2O(l)) from Holt (1981). Values for δ^{18}O(S(IV)) are corrected values of measured δ^{18}O(SO_4^{2-}) from Holt 1981, accounting for the oxidation of S(IV) to sulfate from metal-catalyzed oxidation by O_2 in their experiments.

3.2 δ^{18}O($H_2O_{(gas)}$) estimates for Fairbanks

The isotopic exchange of SO_2 with water vapor yields lighter δ^{18}O(SO_2) than liquid water exchange because δ^{18}O($H_2O_{(g)}$) is lighter than d18O(H2O(l)).[14] Bastrikov et al. (2014) measured δ^{18}O($H_2O_{(g)}$) continuously at the Kourovka astronomical observatory in Western Siberia (57.037°

N, 59.547° E; 300 m above sea level)) between April 2012 and August 2013.[22] Figure S16 shows measured $\delta^{18}O(H_2O_{(g)})$ as a function of temperature at 8 meters above the surface between April 2012 and August 2013 using a Picarro L2130-I wavelength-scanned cavity ring-down spectroscopy analyzer.[15] We use the equation S14 from Figure S16 to calculate $\delta^{18}O(H_2O_{(g)})$ as a function of daily-mean temperature during the ALPACA field campaign. The $\delta^{18}O(H_2O_{(g)})$ values from Figure S16 were compared with the $\delta^{18}O(H_2O_{(l)})$ values presented in Figure S14(a-b). On average, the $\delta^{18}O(H_2O_{(g)})$ signature was -11.3‰ lighter than $(H_2O_{(l)})$, which is consistent with estimates from Broecker and Oversby (1971). Equation S15 was derived from laboratory experiments in Holt et al (1983) was used to estimate $\delta^{18}O(SO_4^{2-})$ from gas-phase oxidation by OH. The average source signatures for $\delta^{18}O(SO_4^{2-})$ used in the model are displayed in Table 1 of the main text.

$$\delta^{18}O(H_2O_{(g)}) = 0.40 \cdot T - 26.0 \tag{14}$$

where T is in degrees Celsius

$$\delta^{18}O\left(SO_4^{2-}\right) = 0.71 \cdot \delta^{18}\mathrm{O}(\mathrm{H_2O_{(g)}}) \tag{15}$$

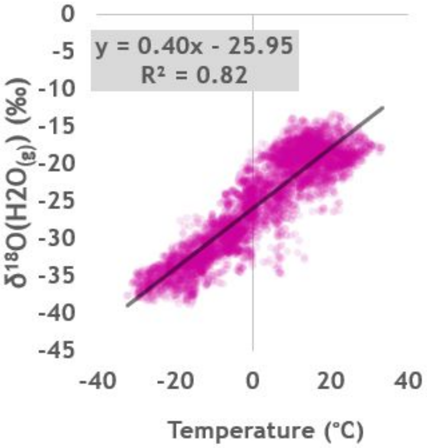

Figure S16. $\delta^{18}O(H_2O_{(g)})$ observations (2012-2013) vs. ambient temperature from Bastrikov et al. (2014).

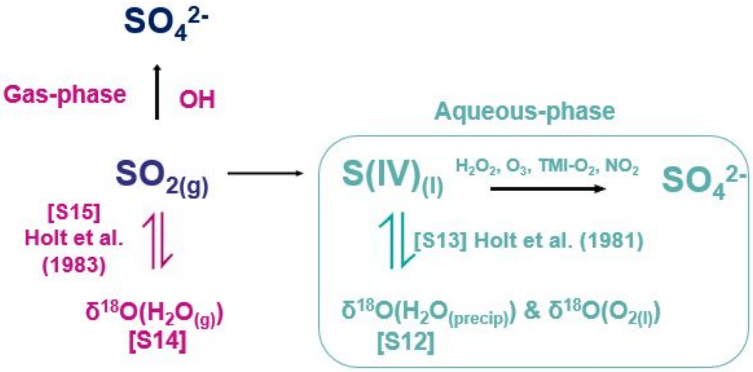

Figure S17. Schematic representation of the gas-phase (pink) and aqueous-phase (blue) equilibration of S(IV). $\delta^{18}O(H_2O_{(precip)})$ varies as a function of ambient temperature (equation S12). Dissolved SO_2 equilibrates with liquid water (equation S13), yielding a heavier $\delta^{18}O$(S(IV) signature than $\delta^{18}O(H_2O_{(l)})$. The $\delta^{18}O(H_2O_{(g)})$ values also vary as a function of temperature (equation S14), yielding a lighter $\delta^{18}O(H_2O_{(g)})$ signature than $\delta^{18}O(H_2O_{(l)})$. Equation S15 estimates the $\delta^{18}O(SO_4^{2-})$ signature from the oxidation of gas-phase SO_2 via OH using the $\delta^{18}O(H_2O_{(g)})$ values calculated with equation S14.[16]

3.3 Source Signatures for $\delta^{18}O(SO_4^{2-})$, $\Delta^{17}O(SO_4^{2-})$, and $\delta^{34}S(SO_4^{2-})$

$\delta^{18}O(SO_4^{2-})$ signature from aqueous-phase oxidation of atmospheric sulfate largely depends on the $\delta^{18}O(H_2O_{(l)})$ signature of the solvent water through isotopic exchange of S(IV) with water (equation S13). Sulfate formed from the NO_2 oxidation pathway has a light $\delta^{18}O$ signature of -17.2±1.6‰ because NO_2SO_3 decomposes and rapidly hydrolyzes to form SO_4^{2-} and HONO.[17–19] TMI-O2-derived sulfate is slightly heavier (-5.3±1.2‰) as the fourth oxygen is from dissolved O_2. The TMI-O_2 path includes both the oxidation of inorganic S(IV) by Fe and Mn as well as by excited triplet states of brown carbon as these produce sulfate with the same O isotopic signature.[20,21] Both H_2O_2 and O_3 oxidation result in a heavier signature ($\delta^{18}O(SO_4^{2-})$ = +10.0±0.8 and +21.3±1.2‰, respectively) because the oxidants themselves have relatively heavy $\delta^{18}O$ values (+22 to +52‰ and +130‰, respectively).[22,23] For H_2O_2, the oxidant supplies two of the four oxygen atoms of sulfate, leaving a smaller contribution from isotopically light water.[24] The H_2O_2 path includes hydrogen peroxide formed in the particle phase and gas phase; however, we expect the gas-phase path to be minor during the most polluted periods because the very high NO_x observed during the campaign may suppress formation of H_2O_2(g).[25,26] We assume that the aqueous-phase source signatures consist of a weighted average between the equilibrated S(IV) calculated in equations 12 and 13 ($\delta^{18}O(S(IV))$) and the oxidants that are transferred to form product sulfate ($\delta^{18}O_{oxidant}$). It is unknown whether there is additional fractionation during these reactions. This represents a source of uncertainty in calculating the source signatures of the H_2O_2, O_3, TMI-O_2, and NO_2 pathways.

Table S6. $\delta^{18}O(SO_4^{2-})$, $\Delta^{17}O(SO_4^{2-})$, and $\delta^{34}S(SO_4^{2-})$ isotopic assumptions used) in the Bayesian isotope mixing model

Pathway	**$\delta^{18}O(SO_4^{2-})$ (‰)** **Average ±1σ‰**	**$\Delta^{17}O(SO_4^{2-})$ (‰)[a]**	**$\varepsilon_{oxidant}$[b]**
Primary	**+23.5‰**	**-0.34‰**	$\delta^{34}S(SO_4^{2})_{primary}$ = +4.7‰, $\varepsilon_{primary}$=0.0
O_3	$\delta^{18}O(S(IV)) \cdot 0.75 + \delta^{18}O(O_3) \cdot 0.25$ = **+ 21.0±2.3‰** where $\delta^{18}O(S(IV))$ is calculated from equation S13 and $\delta^{18}O(O_3)$ = 130‰ from Vicars and Savarino (2014).[23]	**+9.8** (*Vicars and Savarino 2014*)(23)	Equation [S18] *(Harris et al. 2012 (a-c)(27))*
H_2O_2	$\delta^{18}O(S(IV)) \cdot 0.5 + \delta^{18}O(H_2O_2) \cdot 0.5$ = **+ 9.8±1.5‰** where $\delta^{18}O(S(IV))$ is calculated from equation S13 and $\delta^{18}O(H_2O_2)$ = 35.4‰ from Savarino and Thiemens (1999).[22]	**+0.81**	Equation [S18] *(Harris et al. 2012 (a-c) (27))*

TMI-O$_2$	$\delta^{18}O(S(IV)) \cdot 0.75 + \delta^{18}O(O_2) \cdot 0.25$ **= - 5.6±2.3‰** where $\delta^{18}O(S(IV))$ is calculated from equation S13 and $\delta^{18}O(O_2)$ = 23.5‰.[28]	**-0.09**	Equation [S19] *(Harris et al. 2012 (a-c) ([27])*
NO$_2$	$\delta^{18}O(S(IV)) \cdot 0.75 + \delta^{18}O(H_2O) \cdot 0.25$ **= - 17.6±3.1‰** where $\delta^{18}O(S(IV))$ is calculated from equation S13 and $\delta^{18}O(H_2O_{(l)})$*) is calculated with equation S12.[19]	**0.0**	+1.0 *(Yang et al. 2018)([29])*
OH	$\delta^{18}O(SO_4^{2-}) = 0.71(\delta^{18}O(H_2O_{(g)})) + 16.5$ - **6.71 ±2.11‰** where $\delta^{18}O(H_2O_{(g)})$ is calculated with equation S15.	**0.0**	Equation [S20] *(Harris et al. 2012 (a-c) ([27])*

[a] $\Delta^{17}O(SO_4^{2-}) = \delta^{17}O(SO_4^{2-}) - 0.52 \times \delta^{18}O(SO_4^{2-})$

[b] $\varepsilon_{oxidant}$ = sulfur isotopic fractionation factor where $\varepsilon_{oxidant} = (\alpha_{34\ oxidant} - 1) \times 1000$ and $\alpha_{34\ oxidant} = (^{34}S/^{32}S)_{products} / (^{34}S/^{32}S)_{reactants}$

$\Delta^{17}O(SO_4^{2-})$ refers to the enrichment of $\delta^{17}O(SO_4^{2-})$ relative to $\delta^{18}O(SO_4^{2-})$ (equation 1 in the main text) and has been used in many studies to estimate the importance of the H_2O_2 ($\Delta^{17}O(SO_4^{2-})$ = +0.8 ‰) and O_3 ($\Delta^{17}O(SO_4^{2-})$ = +9.8 ‰) formation pathways in various environments.[18,19,22,30] $\Delta^{17}O$ values greater than zero originate during the formation of ozone in the atmosphere.[23] The enriched $\Delta^{17}O(SO_4^{2-})$ from H_2O_2 oxidation is from a minor H_2O_2 formation pathway involving O_3 ($OH + O_3 \rightarrow HO_2 + O_2$).[22,31] It has been shown that photoformation of H_2O_2 can also occur in particles and on snow grains in the Arctic, hereafter referred to as

$HOOH_{(pm)}$.[2,32,33] Since Fairbanks is a cold, NO_x-rich environment, gas-phase H_2O_2 formation via $HO_2 + HO_2$ may be negligible because it cannot compete with $NO + HO_2$. This leaves the possibility that the majority of H_2O_2 may form in particles. In this case, the $\delta^{18}O(SO_4^{2-})$ and $\Delta^{17}O(SO_4^{2-})$ signatures of $HOOH_{(pm)}$-derived sulfate would be +4.1±1.5‰ and -0.17‰, respectively because the oxygen atoms of H_2O_2 are derived from dissolved O_2. Results of additional source signature calculations where all H_2O_2-derived sulfate is assumed to be the result of $HOOH_{(pm)}$ oxidation are shown in section 5.1 The OH and TMI-O_2 pathways have $\Delta^{17}O(SO_4^{2-})$ close to 0‰ (0‰ and -0.10 ‰ respectively) and the $\Delta^{17}O(SO_4^{2})$ of primary sulfate is -0.34 ‰.[28,34,35] The model incorporates mass balance equations S16 and S17, representing the $\delta^{18}O$ and $\Delta^{17}O$ observations with the known isotopic signatures for each respective oxidant (Table 1 of the main text).

$$\delta^{18}O\left(SO_4^{2-}\right) = f_{primary} \cdot \delta^{18}O_{primary} + f_{H_2O_2} \cdot \delta^{18}O_{H_2O_2} + f_{O_3} \cdot \delta^{18}O_{O_3} + f_{TMI-O_2} \cdot \delta^{18}O_{TMI-O_2} + f_{OH} \cdot \delta^{18}O_{OH} + f_{NO2} \cdot \delta^{18}O_{NO2} \quad \textbf{(16)}$$

where $f_{primary} + f_{H2O2} + f_{O3} + f_{TMI\text{-}O2} + f_{OH} + f_{NO2} = 1$

$$\Delta^{17}O\left(SO_4^{2-}\right) = f_{primary} \cdot \Delta^{17}O_{primary} + f_{H_2O_2} \cdot \Delta^{17}O_{H_2O_2} + f_{O_3} \cdot \Delta^{17}O_{O_3} + f_{TMI-O_2} \cdot \Delta^{17}O_{TMI-O_2} + f_{OH} \cdot \Delta^{17}O_{OH} + f_{NO2} \cdot \Delta^{17}O_{NO2} \quad \textbf{(17)}$$

where $f_{primary} + f_{H2O2} + f_{O3} + f_{TMI\text{-}O2} + f_{OH} + f_{NO2} = 1$

$\delta^{34}S(SO_4^{2-})$ measurements help determine secondary sulfate formation pathways because oxidants have different sulfur isotope fractionation factors during the oxidation of SO_2 to sulfate.[27] $\varepsilon_{oxidant}$ is the sulfur isotopic fractionation factor where $\varepsilon_{oxidant} = (\propto_{34oxidant} - 1) \times 1000$ and $\propto_{34\ oxidant} = (^{34}S/^{32}S)_{products} / (^{34}S/^{32}S)_{reactants}$. $\varepsilon_{oxidant}$ of H_2O_2, O_3, OH, and TMI-O_2 depends on ambient temperature during oxidation (equations S18-S20)[27].

$$\varepsilon_{H_2O_2\& O_3} - 1 = 16.51\ (\pm 0.15) - 0.085(\pm 0.4) \cdot T \quad (18)$$

$$\varepsilon_{TMI-O_2} - 1 = -5.039\ (\pm 0.044) - 0.237(\pm 0.004) \cdot T \quad (19)$$

$$\varepsilon_{OH} - 1 = 10.60\ (\pm 0.73) - 0.004(\pm 0.015) \cdot T \quad (20)$$

For average ambient temperature during Winter in Fairbanks, H_2O_2 and O_3 cause the greatest $\delta^{34}S(SO_4^{2-})$ fractionation ($\varepsilon_{H2O2\ \&\ O3} \approx +18‰$). Fractionation factors for OH and NO_2 are also positive ($\varepsilon_{OH} \approx +10.7‰$ and $\varepsilon_{NO2} \approx +1.0‰$).[29,36] Since the TMI-$O_2$ pathway is faster for lighter sulfur isotopes, it has a negative fractionation factor ($\varepsilon_{TMI\text{-}O2} \approx -1‰$).[36]. By principals of Rayleigh distillation, fractionation of sulfur isotopes is greater at low sulfur oxidation ratios.[14] During polluted periods in Fairbanks, sulfur emissions are mostly from ground sources and the sulfur isotope fractionation is at its highest due to low temperatures and sulfur oxidation ratios. This provides an ideal scenario for use of $\delta^{34}S$ measurements to differentiate sulfate formation pathways in Fairbanks. In these ways, combining $\delta^{18}O(SO_4^{2-})$, $\Delta^{17}O(SO_4^{2-})$, and $\delta^{34}S(SO_4^{2-})$ measurements provide complementary information about sources and formation of atmospheric sulfate.

Mass balance equation S21 incorporates a Rayleigh distillation model to calculate the $\delta^{34}S$ isotope fractionation factors (ε) for secondary sulfate as a function of the isotopic primary source signature ($\delta^{34}S_{emission}$), average ambient temperature during sample collection (equations S18-S20), and the secondary sulfur oxidation ratio (SOR_{2nd}) (calculated using equations S22 and S23). $\delta^{34}S_{emission}$ is assumed to be the same as primary sulfate since sulfur isotope fractionation from fuel oil combustion is expected to be minimal due to the high combustion temperature ($\delta^{34}S_{primary}$ = +4.7±0.6‰) (Tables 1 and S4). It should also be noted that the average daily temperature in Fairbanks (-30°C to 0.0°C) was at times colder than the lowest temperatures tested in laboratory experiments to estimate $\delta^{34}S$ fractionation factors (-25°C for H_2O_2, O_3, TMI-O_2, OH,) and -7°C for NO_2.[29,36] Yang et al. (2018) found that there was not a significant temperature difference for NO_2 fractionation at temperatures < 8°C, but this is still a source of uncertainty in estimating the fractional contribution of the NO_2 pathway.

$$\delta^{34}S\left(SO_4^{2-}\right) = f_{primary} \cdot \delta^{34}S_{primary} + (1 - f_{primary}) \cdot (\delta^{34}S_{emission} - (f_{H_2O_2} \cdot \varepsilon_{H_2O_2} + f_{O_3} \cdot \varepsilon_{O_3} + f_{TMI-O_2} \cdot \varepsilon_{TMI-O_2} + f_{OH} \cdot \varepsilon_{OH} + f_{NO2} \cdot \varepsilon_{NO_2})$$

$$\cdot\left(\ln(1-\mathrm{SOR_{2nd}})\cdot\frac{1-\mathrm{SOR_{2nd}}}{\mathrm{SOR_{2nd}}}\right) \text{ where } f_{primary}+f_{H2O2}+f_{O3}+f_{TMI\text{-}O2}+f_{OH}+f_{NO2}=1 \tag{21}$$

$$\mathrm{SO_{4\,secondary}^{2-}} = [\mathrm{SO_4^{2-}}]\cdot(1-\mathrm{f_{primary}}) \tag{22}$$

$$\mathrm{SOR_{2nd}} = \frac{[\mathrm{SO_{4\,secondary}^{2-}}]}{[\mathrm{SO_{4\,secondary}^{2-}}]+[\mathrm{SO_2}]} \tag{23}$$

3.4 Model Performance

Figure S18(a-f) show model performance compared to observations for $\delta^{18}O$(a-b), $\Delta^{17}O$(c-d), and $\delta^{34}S$ (e-f). In Figure S18(a-d), the r^2 for $\delta^{18}O$ and $\Delta^{17}O$ observations vs. model output are 0.999 and 0.992, respectively. Noteworthy differences between $\delta^{18}O$ model output vs. observations occur between Jan.19-31, which are attributed to a slight underestimate in primary sulfate since $\Delta^{17}O$ performs well during this period, suggesting that O_3 oxidation is not being underestimated (Figure S18(a)). For higher $\delta^{18}O$, the model slightly underpredicts $\delta^{18}O$ and thus primary sulfate (Figure S18(b)). Noteworthy differences between $\Delta^{17}O$ model output vs. observations occur during the polluted period from Jan. 31 through February 1. This slight disagreement is not present in model output when all H_2O_2 is assumed to come from the particle-phase formation pathway (HOOH(pm), where $\Delta^{17}O = 0.0$ ‰) vs. H_2O_2 formed in the gas-phase ($\Delta^{17}O = 0.8$‰) (see section 5 of supporting information). Due to the high NOx concentrations during the polluted period, it's possible that gas-phase formation of H_2O_2 is not an important oxidant source for sulfate formation, which would explain the small discrepancy in the model output $\Delta^{17}O$ and observations. Regardless of the source signatures used for H_2O_2, the fractional contribution for H_2O_2 is similar in the model output so this is likely not a large source of error in estimating the fractional contribution of sulfate formed through H_2O_2 oxidation.

In Figure S18(e-f), the r^2 for $\delta^{34}S$ observations vs. MCMC output is 0.81. MCMC $\delta^{34}S$ is generally higher than the observations, though most of the 95% confidence intervals overlap with observations (noteworthy differences are Jan. 23-29, Feb. 6, and Feb. 25). For the disagreement in early January, this is likely due to an underestimate in primary sulfate shown in Figure S18(a-b). MCMC $\delta^{34}S$ is lower than $\delta^{34}S$ observations during the polluted period, particularly during the daytime on January 31st. Given the good MCMC agreement with oxygen observations these discrepancies in the $\delta^{34}S$ portion of the model is likely only a minor source of error in the final estimates for the fractional contributions of the six sulfate formation pathways.

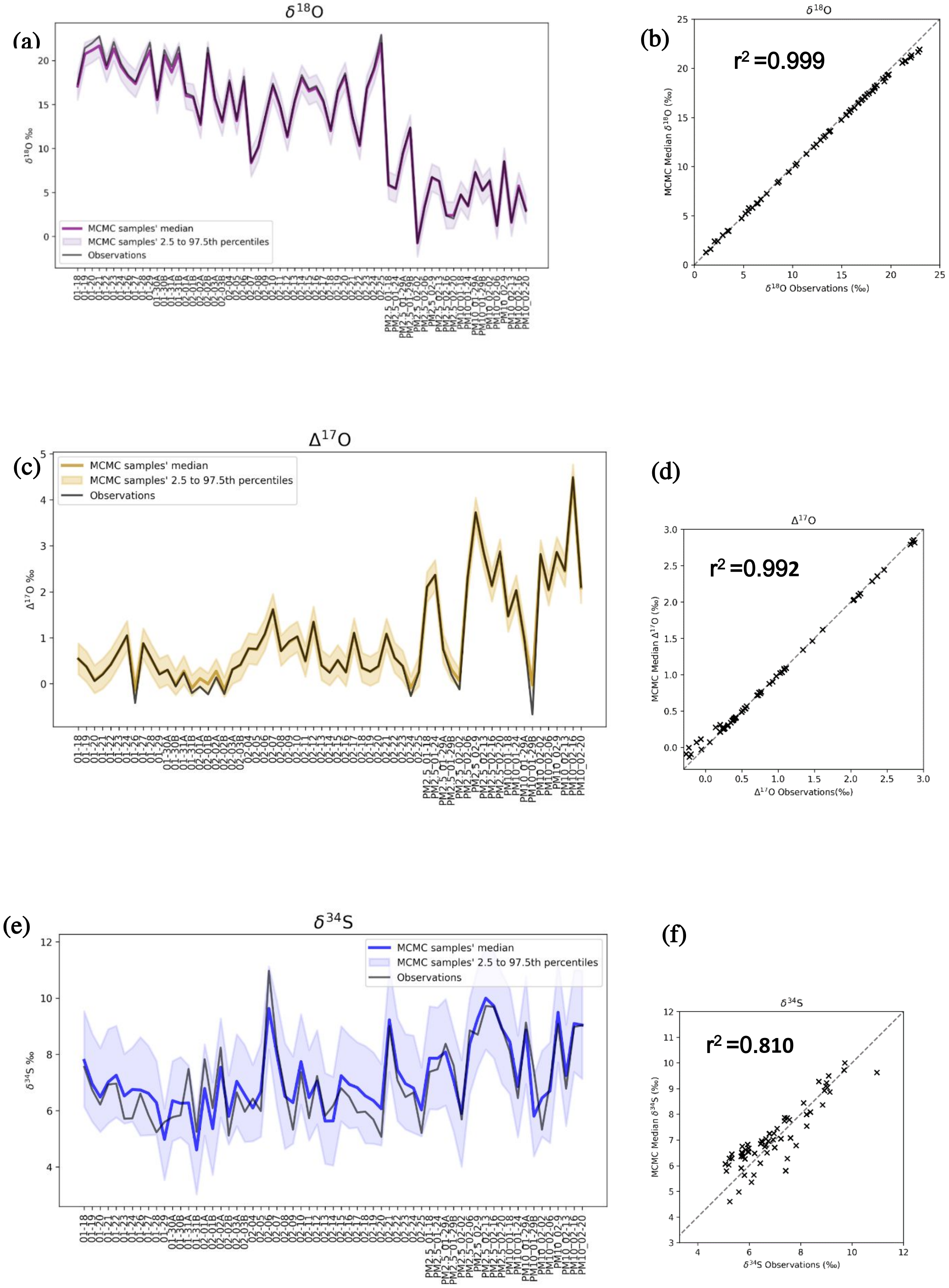
(a)
δ18O
δ18O ‰
MCMC samples' median
MCMC samples' 2.5 to 97.5th percentiles
Observations
(b)
δ18O
r² =0.999
MCMC Median δ18O (‰)
δ18O Observations (‰)
(c)
Δ17O
Δ17O ‰
MCMC samples' median
MCMC samples' 2.5 to 97.5th percentiles
Observations
(d)
Δ17O
r² =0.992
MCMC Median Δ17O (‰)
Δ17O Observations(‰)
(e)
δ34S
δ34S ‰
MCMC samples' median
MCMC samples' 2.5 to 97.5th percentiles
Observations
(f)
δ34S
r² =0.810
MCMC Median δ34S (‰)
δ34S Observations (‰)

Figure S18(a). Calculated MCMC median (purple) and observed (black) δ^{18}O values throughout the campaign. The shading represents the 95% confidence interval in the model's ability to reproduce observations. **(b) .** Linear least-squares regression of δ^{18}O observations vs. MCMC output. **Figure S18(c).** Calculated MCMC median (gold) and observed (black) Δ^{17}O values throughout the campaign. The shading represents the 95% confidence interval in the model's ability to reproduce observations. **(d)(.** Linear least-squares regression of Δ^{17}O observations vs. MCMC output. **Figure S18(e).** Calculated MCMC median (gold) and observed (black) δ^{34}S values throughout the campaign. The shading represents the 95% confidence interval in the model's ability to reproduce observations.**(f).** Linear least-squares regression of δ^{34}S observations vs. MCMC output.

4. Bayesian Isotope Mixing Model Results

4. 1 Time series of fractional contributions of primary and secondary sulfate

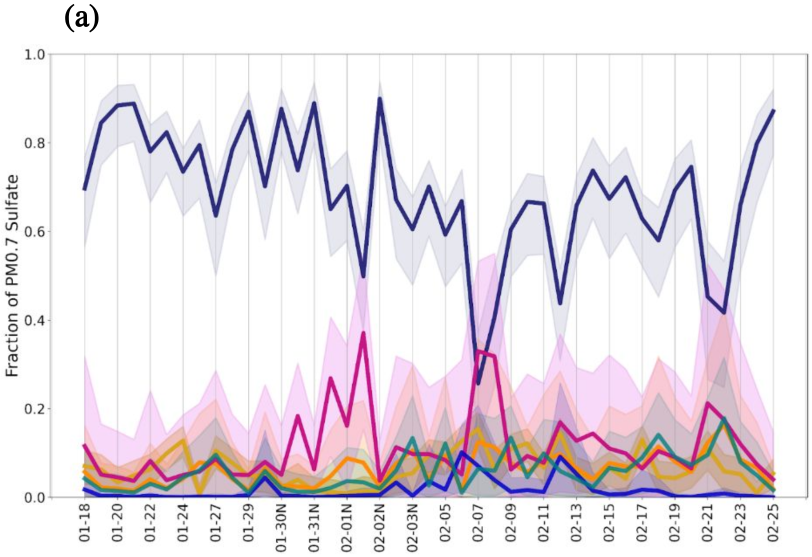

Figure S19 (a-c). MCMC median modeled fractions for the sources and formation pathways of Fairbanks for $PM_{0.7}$ sulfate **(a)**, $PM_{0.7\text{-}2.5}$ sulfate **(b),** and $PM_{2.5\text{-}10}$ sulfate **(c).** The shading represents the 95% confidence interval for each sulfate formation pathway.

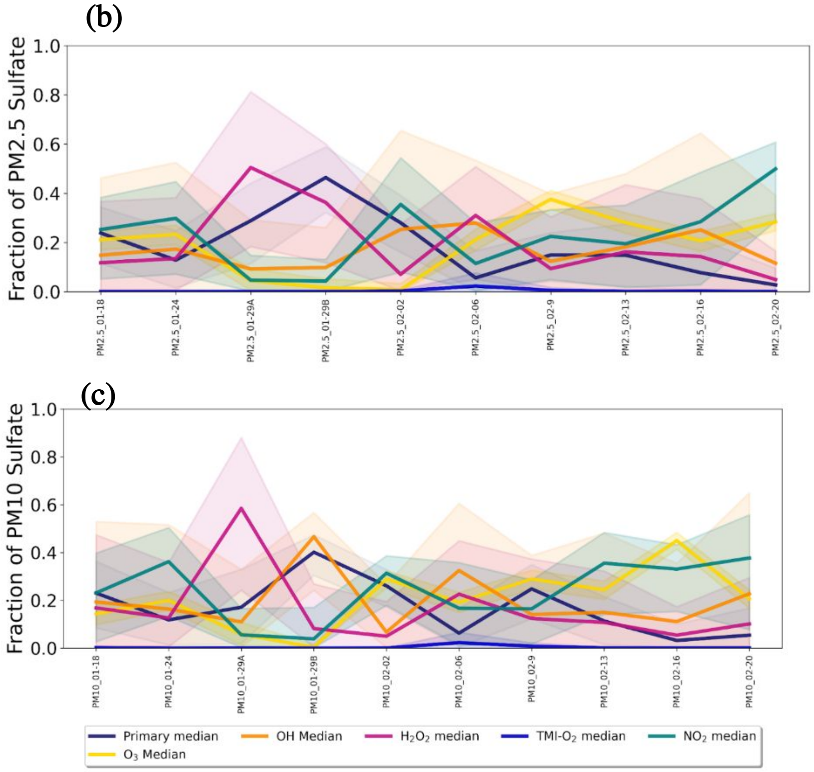

4. 2 Secondary Sulfate and HMS mass concentrations

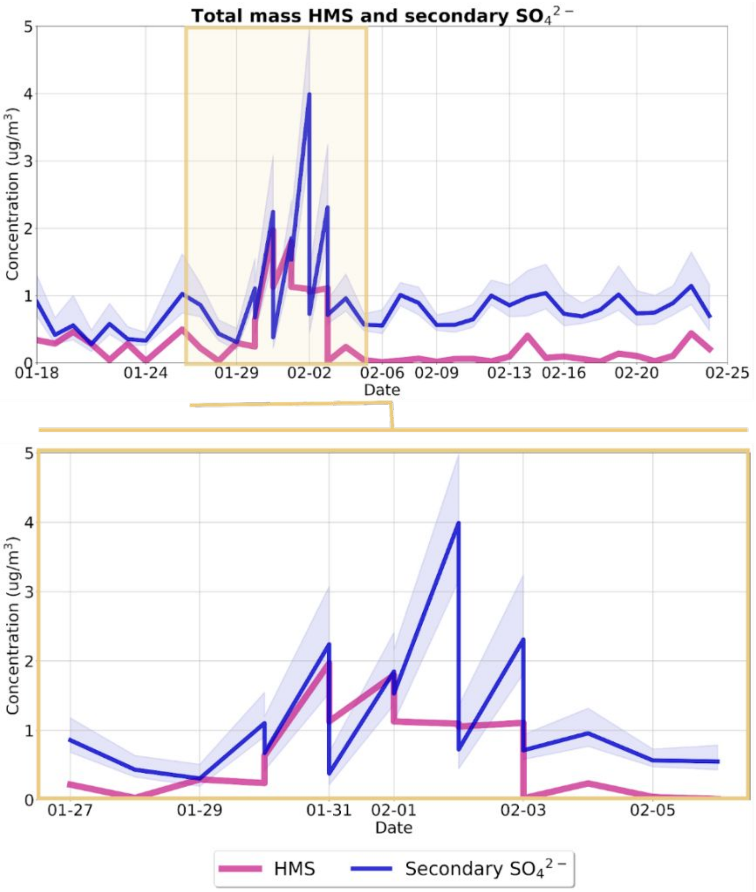

Figure S20. Mass concentrations of total secondary sulfate (blue) and HMS (pink) throughout the campaign. The blue shading shows the 95% confidence interval for secondary sulfate from the MCMC model.

4. 3 Linear regressions of secondary sulfate formation pathways

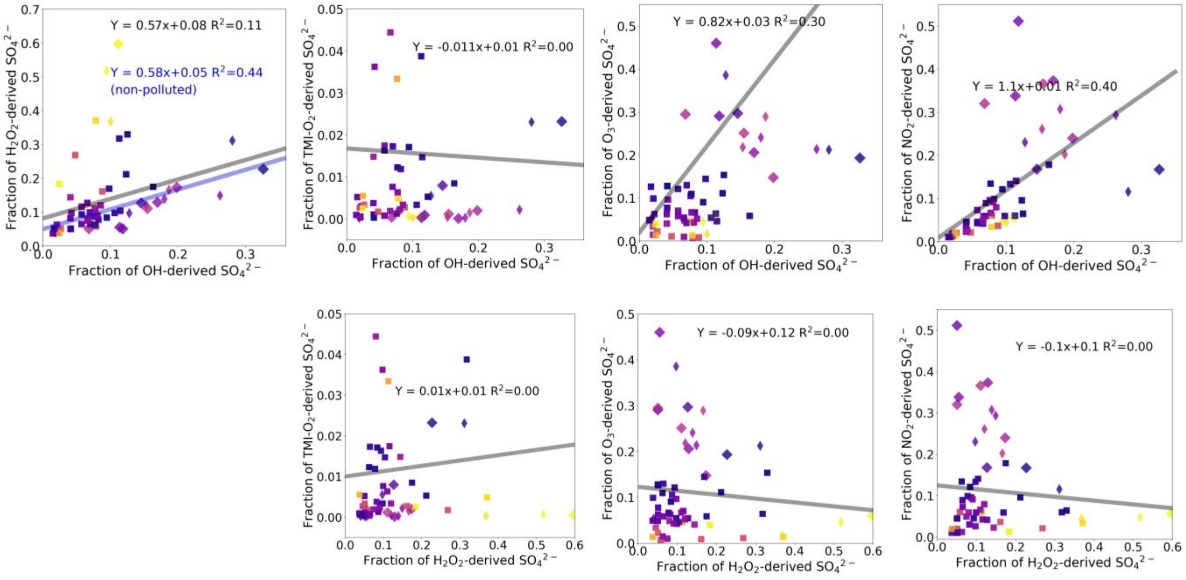

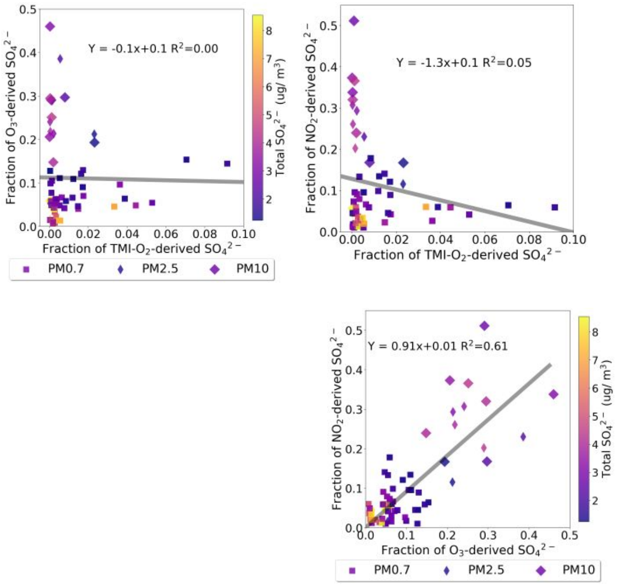

Figure S21. Linear regressions of secondary oxidation pathways for sulfate formation in Fairbanks.

Figure S21 shows linear regressions of secondary oxidation pathways for sulfate formation in Fairbanks. The NO_2 vs. OH regressions (r^2= 0.40, p-value <0.01) suggests association between the two photochemically-driven sulfate formation pathways. Sulfate from O_3 is also weakly associated with OH-derived sulfate (r^2= 0.30). There is no association between TMI- O_2 versus OH (r^2= 0.00), O_3 (r^2 = 0.00), or NO_2 (r^2 = 0.05), which indicates that the MCMC model can differentiate between these pathways despite their similar $\Delta^{17}O$ source signatures. O_3 and NO_2, which are both pH-sensitive sulfate formation pathways, are not associated with H_2O_2-derived sulfate (r^2= 0.00 for both). O_3 and NO_2 -derived sulfate show the strongest correlation among the secondary sulfate formation pathways (r^2= 0.61, p-value < 0.01), as expected due to their similar pH-dependencies.

The fraction of O_3-derived sulfate is moderately correlated with ambient O_3 concentrations with r^2= 0.40 for $PM_{0.7}$ and r^2 =0.30 for $PM_{>0.7}$ (figure S22(a-b)).

4. 4 Isotope mixing model results comparison with measured ambient O_3 and metal concentrations

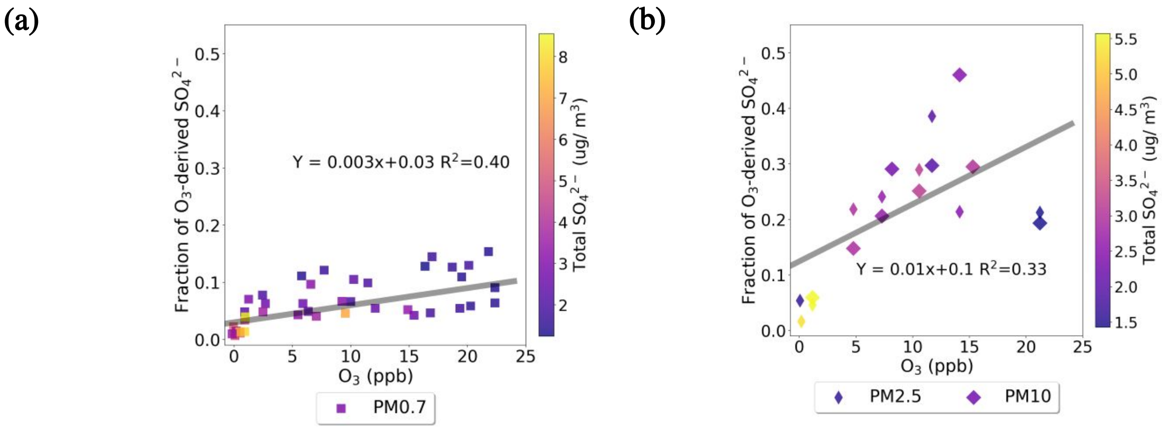

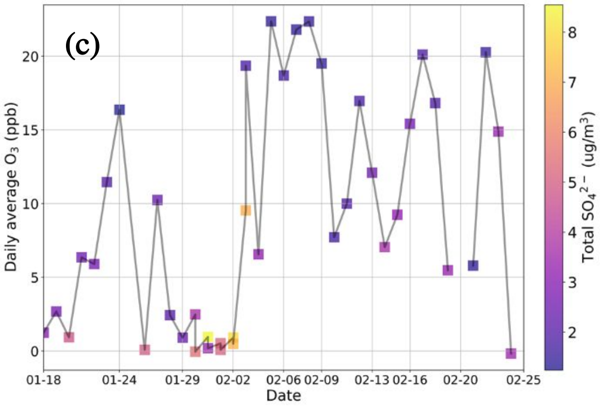

Figure S22(a). The relationship between the fraction of O_3-derived sulfate and ambient O_3 concentrations (ppb) for $PM_{0.7}$ particles. **(b).** The relationship between the fraction of O_3-derived sulfate vs. ambient O_3 concentrations (ppb) for $PM>_{0.7}$ particles. **(c).** Time series of ambient O_3 concentrations (ppb) throughout the campaign.

Water-soluble metal concentrations were measured with the same tecnique as Yang and Weber (2022).[37] Briefly, filters collected at CTC were divided and shipped to the Georgia Institute of Technology. Two 1-inch punches were taken from the filters and extracted in 12mL of 18 MΩ cm^{-1} water before 30 minutes of sonication (Ultrasonic Cleanser, VWR International LLC, West Chester, PA, USA). Water-soluble metals were filtered through a 0.45 μm PTFE syringe filter (Fisherbrand™). Metals were measured using inductively coupled plasma mass spectrometry (ICP-MS, Agilent 7500a series, Agilent Technologies, Inc., CA, USA). Boxplots of bulk water-soluble manganese and iron concentrations are plotted in Figure S23.

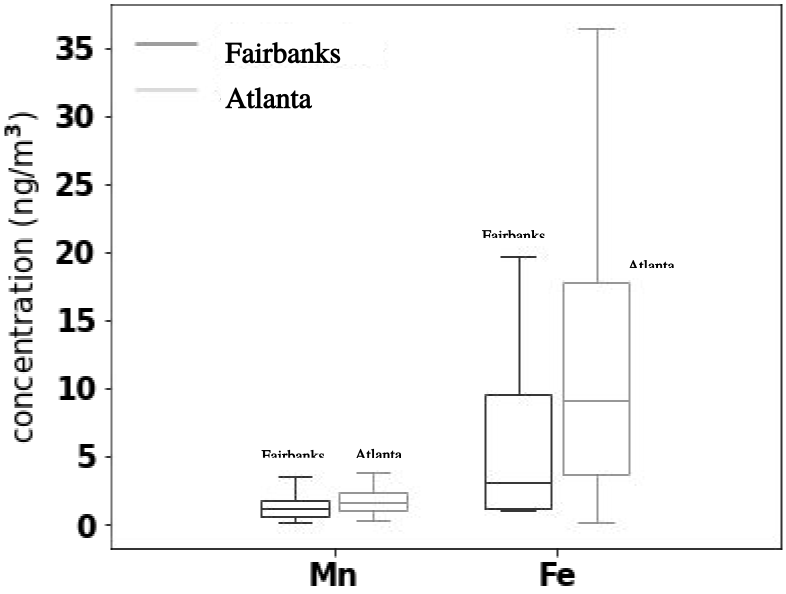

Figure S23. Bulk aerosol water-soluble metal concentrations in (ng/m^3) for Atlanta (silver) and Fairbanks (black) for manganese (left) and iron (right).

5. Additional Markov Chain Monte Carlo Simulations

5.1 Mechanisms for H_2O_2 formation in particles via the $HOOH_{pm}$ pathway.

In this section, we explore the assumption that all H_2O_2 is formed in particles via the $HOOH_{pm}$ pathway rather than via the gas-phase reaction $HO_2 + HO_2 \rightarrow H_2O_2 + O_2$.

We describe three possible reaction sequences to form HOOH(pm). In all three reaction sequences, both oxygen atoms of HOOH(pm) are derived from dissolved molecular oxygen. Sulfate that forms from oxidation by HOOH(pm) will derive two oxygen atoms from sulfite and two from dissolved oxygen (see Table S7 for MCMC assumptions).

Brown carbon-mediated formation of HOOH in particles is summarized in scheme 2 (reactions 1-5). Aromatic carbonyls (ArCHO), as representative brown carbon compounds, absorb light to form excited triplet states (scheme 2, reaction 1). The triplets are then reduced by phenols (ArOH), which are abundant in wood smoke, to form a ketyl radical (scheme 2, reaction 2). The ketyl radical reacts with O_2 (dissolved oxygen) to form an aromatic peroxyl radical, and subsequently, aqueous $HOO^{\cdot}$ and the parent ArCHO compound (scheme 2, reaction 3). This is then followed by the self-disproportionation of aqueous $HOO^{\cdot}$ to form HOOH (scheme 2, reaction 4), and Cu(I)-catalyzed reduction of aqueous $HOO^{\cdot}$ to HOOH (scheme2, reaction 5).

Scheme 2: Brown carbon-mediated formation of HOOH in particles from Anastasio et al., 1997[38]

$$\mathrm{ArCHO} \xrightarrow{hv} {}^{3*}[\mathrm{ArCHO}]\ (\text{excited state triplet})\ [\text{Scheme 2, reaction 1}]$$

$$^{3}[\mathrm{ArCHO}]^{*} + \mathrm{ArOH} \rightarrow \mathrm{ArC}^{\cdot}(\mathrm{H})\mathrm{OH} + \mathrm{ArO}^{\cdot}\ [\text{Scheme 2, reaction 2}]$$

$$\mathrm{ArC}^{\cdot}(\mathrm{H})\mathrm{OH} + \mathrm{O_2} \rightarrow \mathrm{ArC}^{\cdot}(\mathrm{H})(\mathrm{OO}^{\cdot})\mathrm{OH} \rightarrow \mathrm{ArCHO} + HOO^{\cdot}\ [\text{Scheme 2, reaction 3}]$$

$$\mathrm{HOO}^{\cdot} + \mathrm{HOO}^{\cdot} \rightarrow \mathrm{HOOH} + \mathrm{O_2}\ [\text{Scheme 2, reaction 4}]$$

$$\mathrm{HOO}^{\cdot} + \mathrm{Cu}^{+} \xrightarrow{\mathrm{H+}} \mathrm{HOOH} + \mathrm{O_2}\ [\text{Scheme 2, reaction 5}]$$

Scheme 3: $^{3}C^{*} + S(IV)$Mechanisms (Wang et al. 2020):Electron transfer to T^{*}

$$\mathrm{HSO_3^-} + {}^{*}\mathrm{T} \rightarrow \mathrm{HSO_3^{\cdot}} + \mathrm{T}^{\cdot -}\quad [\text{Scheme 3, reaction 1}]$$

$$\mathrm{HSO^{\cdot}_{3(aq)}} \rightarrow \mathrm{SO_3^-} + \mathrm{H}^{+}\quad (\text{rapid equilibrium})\ [\text{Scheme 3, reaction 2}]$$

$O_2 + SO_3^- \rightarrow SO_5^-$ [Scheme 3, reaction 3]

$SO_5^- + SO_5^- \rightarrow 2\ SO_4^- + O_2$ [Scheme 3, reaction 4]

$SO_4^- + HSO_3^- \rightarrow SO_3^- + H^+ + SO_4^{2-}$ [Scheme 3, reaction 5]

Scheme 4: $^3C^* + S(IV)$ Mechanisms (Wang et al. 2020):Hydrogen transfer to T^*

$HSO_3^- + {}^*T \rightarrow SO_3^- + HT^\cdot$ [Scheme 4, reaction 1]

$SO_{3(aq)}^- + O_{2(aq)} \rightarrow SO_5^-$ [Scheme 4, reaction 2]

$SO_5^- + SO_5^- \rightarrow 2SO_4^- + O_2$ [Scheme 4, reaction 4]

$SO_4^- + HSO_3^- \rightarrow SO_3^- + H^+ + SO_4^{2-}$ [Scheme 4, reaction 5]

Table S7. $\delta^{18}O(SO_4^{2-})$, $\Delta^{17}O(SO_4^{2-})$, and $\delta^{34}S(SO_4^{2-})$ isotopic assumptions used in Markov-Chain Monte Carlo (MCMC) isotope mixing model using the HOOH(pm) source signatures

Pathway	**$\delta^{18}O(SO_4^{2-})$ (‰)** **Average ±1σ‰**	**$\Delta^{17}O(SO_4^{2-})$ (‰)**[a]	**$\varepsilon_{oxidant}$**[b]
Primary	**+23.5‰**	**-0.34‰**	$\delta^{34}S(SO_4^{2})_{primary}$ = +4.7‰, $\varepsilon_{primary}$=0.0
O_3	$\delta^{18}O(S(IV))\cdot 0.75+\delta^{18}O(O_3)\cdot 0.25$ **= + 21.0±2.3‰** where $\delta^{18}O(S(IV))$ is calculated from equation S13 and $\delta^{18}O(O_3)$ = 130‰ from Vicars and Savarino (2014).[23]	**+9.8** (*Vicars and Savarino 2014*)(23)	Equation [S18] *(Harris et al. 2012 (a-c)* [27]
HOOH(pm)	$\delta^{18}O(S(IV))\cdot 0.5+\delta^{18}O(HOOH(pm))\cdot 0$ **= + 4.1 ± 1.5‰** where $\delta^{18}O(S(IV))$ is calculated from equation S13 and $\delta^{18}O(HOOH(pm))$ = 23.5‰ from schemes 2-4.[22]	**-0.17**	Equation [S18] *(Harris et al. 2012 (a-c)* [27]

TMI-O_2	$\delta^{18}O(S(IV)) \cdot 0.75 + \delta^{18}O(O_2) \cdot 0.25$ **= - 5.6±2.3‰** where $\delta^{18}O(S(IV))$ is calculated from equation S13 and $\delta^{18}O(O_2)$ = 23.5‰.[28]	**-0.09**	Equation [S19] *(Harris et al. 2012 (a-c)*[27]
NO_2	$\delta^{18}O(S(IV)) \cdot 0.75 + \delta^{18}O(H_2O\,) \cdot 0.25$ **= - 17.6±3.1‰** where $\delta^{18}O(S(IV))$ is calculated from equation S13 and $\delta^{18}O(H_2O_{(l)})$*) is calculated with equation S12.[19]	**0.0**	+1.0 *(Yang et al. 2018)*[29]
OH	$0.71(\delta^{18}O(H_2O_{(g)})) + 16.5$ **-6.71 ±2.11‰** where $\delta^{18}O(H_2O_{(g)})$ is calculated with equation S15.	**0.0**	Equation [S20] *(Harris et al. 2012 (a-c)*[27]

[a] $\Delta^{17}O(SO_4^{2-}) = \delta^{17}O(SO_4^{2-}) - 0.52 \times \delta^{18}O(SO_4^{2-})$

[b] $\varepsilon_{oxidant}$ = sulfur isotopic fractionation factor where $\varepsilon_{oxidant} = (\alpha_{34\ oxidant} - 1) \times 1000$ and $\alpha_{34\ oxidant} = (^{34}S/^{32}S)_{products} / (^{34}S/^{32}S)_{reactants}$

5.2 Model performance for $HOOH_{pm}$ simulation

There is not a statistically significant difference between MCMC-estimated fractional contributions from the six sulfate formation pathways regardless of the H_2O_2 signature used (Tables S8 and S9). The r^2 of the least-squares regression comparing model output to the $\delta^{18}O(SO_4^{2-})$ observations is about the same when the HOOH(pm) signature from Table S7 is used (Figures S18(b) and S25(b)). For $\Delta^{17}O(SO_4^{2-})$, there is slightly better agreement for MCMC output and observations for the HOOH(pm) simulation (r^2 = 0.995, Figure S25(d)) compared to when assuming gas-phase production of H_2O_2 (r^2 = 0.991, Figure S18(d)). Due to the high NOx concentrations during the polluted period, it is likely that the gas-phase formation of H_2O_2 is minor, which would explain why there is slightly better agreement with $\Delta^{17}O$ model output and observations when the HOOH(pm) signature is used. Model performance for $\delta^{34}S$ is the same for both simulations, as expected given that sulfur isotope fractionation is the same regardless of whether the H_2O_2 is formed in the gas or particle phase.

(a)

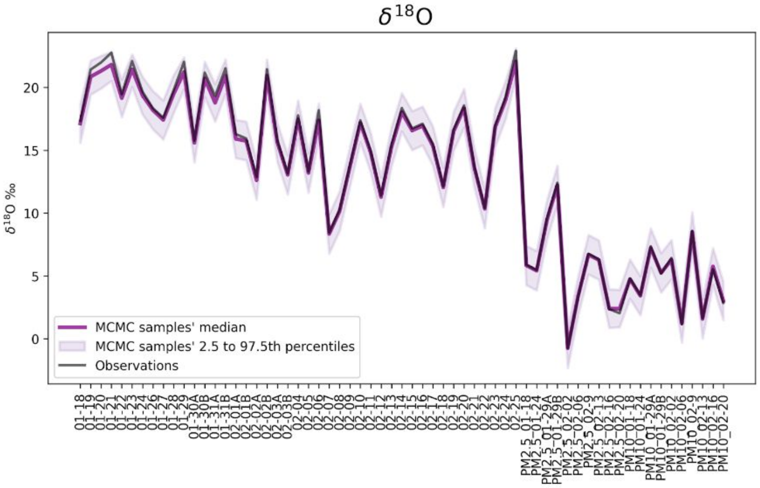

(b)

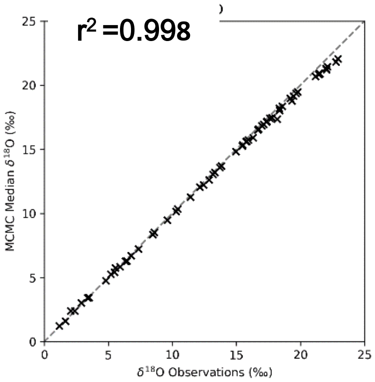

(c)

(d)

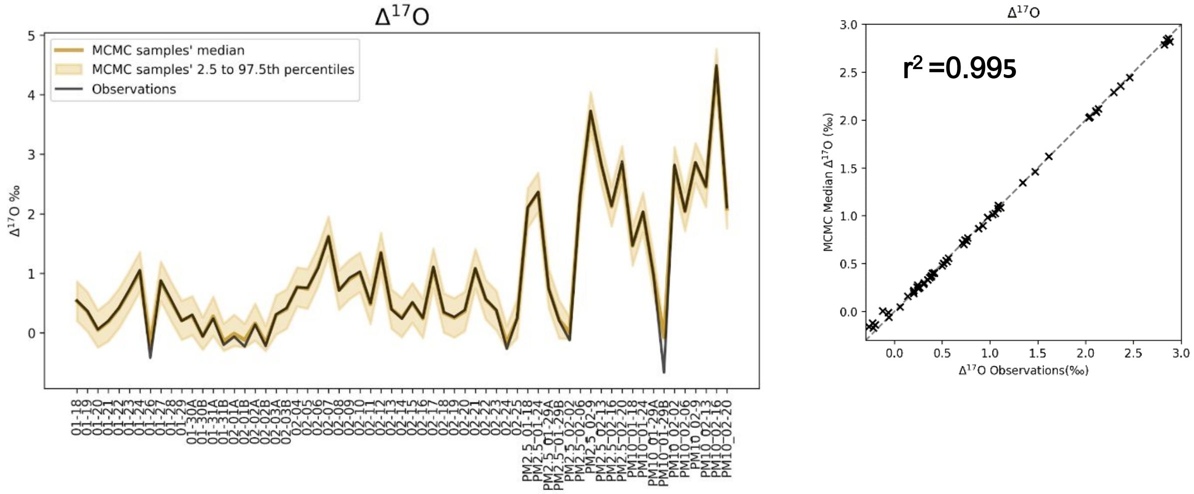

(e)

(f)

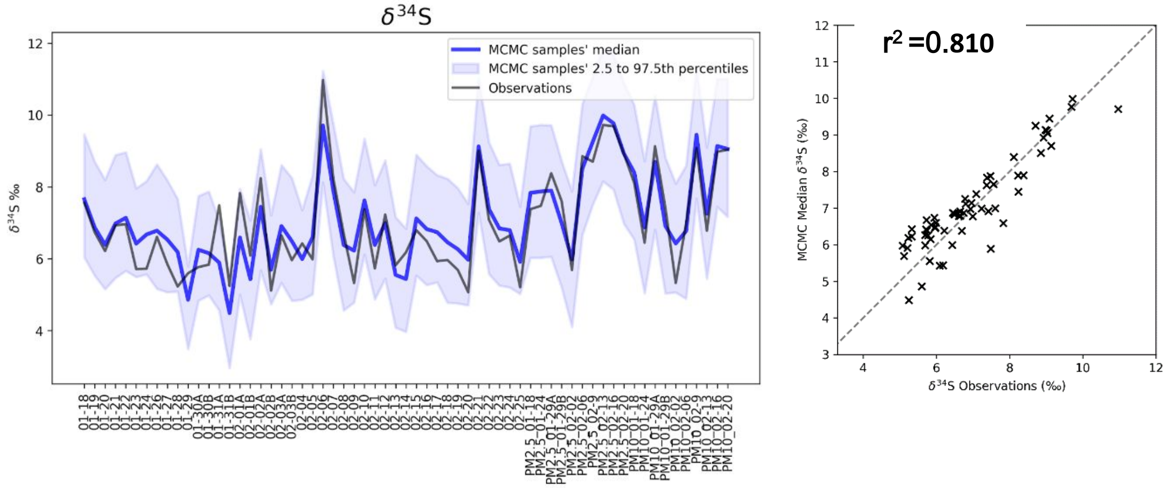

Figure S24(a). Calculated MCMC median (purple) and observed (black) δ^{18}O values throughout the campaign when all H_2O_2 is formed in the particle phase. The shading represents the 95%

confidence interval in the model's ability to reproduce observations. **(b).** Linear least-squares regression of $\delta^{18}O$ observations vs. MCMC output when all H_2O_2 is formed in the particle phase.

(c). Calculated MCMC median (purple) and observed (black) $\Delta^{17}O$ values throughout the campaign when all H_2O_2 is formed in the particle phase. The shading represents the 95% confidence interval in the model's ability to reproduce observations. **(d).** Linear least-squares regression of $\Delta^{17}O$ observations vs. MCMC output when all H_2O_2 is formed in the particle phase.

(e). Calculated MCMC median (purple) and observed (black) $\delta^{34}S$ values throughout the campaign when all H_2O_2 is formed in the particle phase. The shading represents the 95% confidence interval in the model's ability to reproduce observations. **(f).** Linear least-squares regression of $\delta^{34}S$ observations vs. MCMC output when all H_2O_2 is formed in the particle phase.

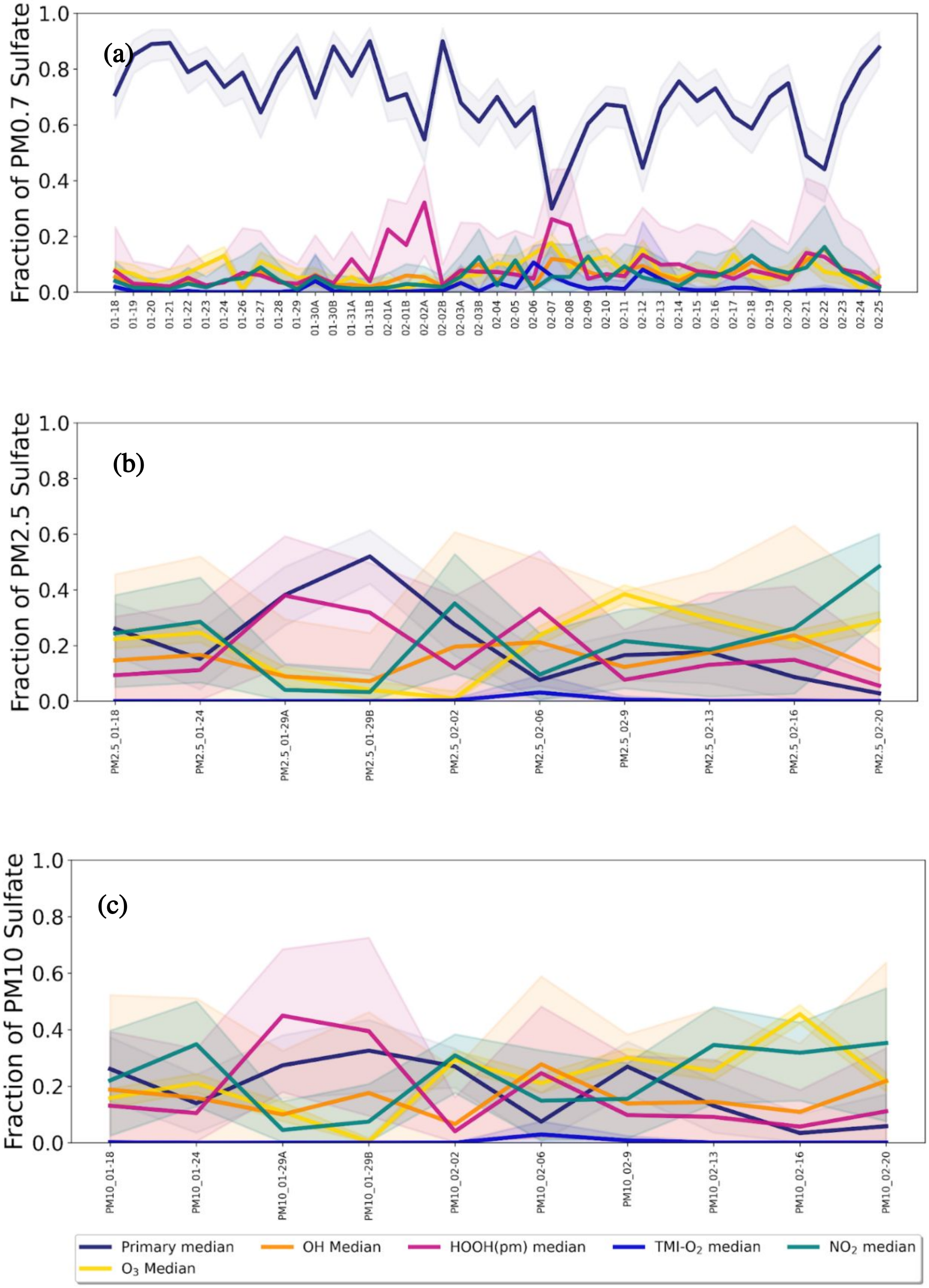

Figure S25 (a-c). MCMC median modeled fractions for the sources and formation pathways of Fairbanks for $PM_{0.7}$ sulfate **(a)**, $PM_{0.7\text{-}2.5}$ sulfate **(b),** and $PM_{2.5\text{-}10}$ sulfate **(c)** using source signatures from Table S7. The shading represents the 95% confidence interval for each sulfate formation pathway.

Table S8. Two-sample T-test for MCMC output using H_2O_2 or HOOH(pm) isotopic signatures for $PM_{0.7}$ sulfate

Statistic	**MCMC assumption**	**Fraction primary**	**Fraction OH**	**Fraction H_2O_2**	**Fraction TMI-O_2**	**Fraction O_3**	**Fraction NO_2**

Average± Stdev	H_2O_2	69±14% n=43	6±4% n=43	11±8% n=43	2±2% n=43	6±4% n=43	6±4% n=43
Average	HOOH(pm)	70±11% n=43	6±2% n=43	9±5% n=43	2±1% n=43	7±3% n=43	6±2% n=43
Significant Difference?		no	no	no	no	no	no
p-value		0.14	1.00	0.17	1.00	0.19	1.00

Table S9. Two-sample T-test for MCMC output using H_2O_2 or HOOH(pm) isotopic signatures for $PM_{>0.7}$ sulfate

Statistic	**MCMC assumption**	**Fraction primary**	**Fraction OH**	**Fraction H_2O_2**	**Fraction TMI-O_2**	**Fraction O_3**	**Fraction NO_2**
Average± Stdev	H_2O_2	18±12% n=18	16±6% n=18	20±15% n=18	0±1% n=18	22±10% n=18	24±12% n=18
Average	HOOH(pm)	21±14% n=18	15±5% n=18	17±12% n=18	0±1% n=18	24±10% n=18	23±12% n=18
Significant Difference?		no	no	no	no	no	no
p-value		0.14	1.00	0.17	1.00	0.19	1.00

References

(1) Ma, T.; Furutani, H.; Duan, F.; Kimoto, T.; Jiang, J.; Zhang, Q.; Xu, X.; Wang, Y.; Gao, J.; Geng, G.; Li, M.; Song, S.; Ma, Y.; Che, F.; Wang, J.; Zhu, L.; Huang, T.; Toyoda, M.; He, K. Contribution of Hydroxymethanesulfonate (HMS) to Severe Winter Haze in the North China Plain. *Atmospheric Chem. Phys.* **2020**, *20* (10), 5887–5897. https://doi.org/10.5194/acp-20-5887-2020.

(2) Moch, J. M.; Dovrou, E.; Mickley, L. J.; Keutsch, F. N.; Liu, Z.; Wang, Y.; Dombek, T. L.; Kuwata, M.; Budisulistiorini, S. H.; Yang, L.; Decesari, S.; Paglione, M.; Alexander, B.; Shao, J.; Munger, J. W.; Jacob, D. J. Global Importance of Hydroxymethanesulfonate in Ambient Particulate Matter: Implications for Air Quality. *J. Geophys. Res. Atmospheres* **2020**, *125* (18). https://doi.org/10.1029/2020JD032706.

(3) Song, S.; Ma, T.; Zhang, Y.; Shen, L.; Liu, P.; Li, K.; Zhai, S.; Zheng, H.; Gao, M.; Moch, J. M.; Duan, F.; He, K.; McElroy, M. B. Global Modeling of Heterogeneous Hydroxymethanesulfonate Chemistry. *Atmospheric Chem. Phys.* **2021**, *21* (1), 457–481. https://doi.org/10.5194/acp-21-457-2021.

(4) Neubauer, K. R.; Sum, S. T.; Johnston, M. V.; Wexler, A. S. Sulfur Speciation in Individual Aerosol Particles. *J. Geophys. Res. Atmospheres* **1996**, *101* (D13), 18701–18707. https://doi.org/10.1029/96JD01555.

(5) Whiteaker, J. R.; Prather, K. A. Hydroxymethanesulfonate as a Tracer for Fog Processing of Individual Aerosol Particles. *Atmos. Environ.* **2003**, *37* (8), 1033–1043. https://doi.org/10.1016/S1352-2310(02)01029-4.

(6) Dovrou, E.; Lim, C. Y.; Canagaratna, M. R.; Kroll, J. H.; Worsnop, D. R.; Keutsch, F. N. Measurement Techniques for Identifying and Quantifying Hydroxymethanesulfonate (HMS) in an Aqueous Matrix and Particulate Matter Using Aerosol Mass Spectrometry and Ion Chromatography. *Atmospheric Meas. Tech.* **2019**, *12* (10), 5303–5315. https://doi.org/10.5194/amt-12-5303-2019.

(7) Chapman, E. G.; Barinaga, C. J.; Udseth, H. R.; Smith, R. D. Confirmation and Quantitation of Hydroxymethanesulfonate in Precipitation by Electrospray Ionization-Tandem Mass Spectrometry. *Atmospheric Environ. Part Gen. Top.* **1990**, *24* (12), 2951–2957. https://doi.org/10.1016/0960-1686(90)90475-3.

(8) Schauer, A. J.; Kunasek, S. A.; Sofen, E. D.; Erbland, J.; Savarino, J.; Johnson, B. W.; Amos, H. M.; Shaheen, R.; Abaunza, M.; Jackson, T. L.; Thiemens, M. H.; Alexander, B. Oxygen Isotope Exchange with Quartz during Pyrolysis of Silver Sulfate and Silver Nitrate: Oxygen Isotope Exchange during Pyrolysis of Ag $_2$ SO $_4$ and AgNO $_3$. *Rapid Commun. Mass Spectrom.* **2012**, *26* (18), 2151–2157. https://doi.org/10.1002/rcm.6332.

(9) Geng, L.; Schauer, A. J.; Kunasek, S. A.; Sofen, E. D.; Erbland, J.; Savarino, J.; Allman, D. J.; Sletten, R. S.; Alexander, B. Analysis of Oxygen-17 Excess of Nitrate and Sulfate at Sub-Micromole Levels Using the Pyrolysis Method: Analysis of Oxygen-17 Excess of Nitrate and Sulfate. *Rapid Commun. Mass Spectrom.* **2013**, *27* (21), 2411–2419. https://doi.org/10.1002/rcm.6703.

(10) Jongebloed, U. A.; Schauer, A. J.; Cole-Dai, J.; Larrick, C. G.; Wood, R.; Fischer, T. P.; Carn, S. A.; Salimi, S.; Edouard, S. R.; Zhai, S.; Geng, L.; Alexander, B. Underestimated Passive Volcanic Sulfur Degassing Implies Overestimated Anthropogenic Aerosol Forcing. *Geophys. Res. Lett.* **2023**, *50* (1). https://doi.org/10.1029/2022GL102061.

(11) Kok, G. L.; Gitlin, S. N.; Lazrus, A. L. Kinetics of the Formation and Decomposition of Hydroxymethanesulfonate. *J. Geophys. Res.* **1986**, *91* (D2), 2801. https://doi.org/10.1029/JD091iD02p02801.

(12) Holt, B. D.; Kumar, R.; Cunningham, P. T. Oxygen-18 Study of the Aqueous-Phase Oxidation of Sulfur Dioxide. *Atmospheric Environ. 1967* **1981**, *15* (4), 557–566. https://doi.org/10.1016/0004-6981(81)90186-4.

(13) Dovrou, E.; Bates, K. H.; Moch, J. M.; Mickley, L. J.; Jacob, D. J.; Keutsch, F. N. Catalytic Role of Formaldehyde in Particulate Matter Formation. *Proc. Natl. Acad. Sci.* **2022**, *119* (6), e2113265119. https://doi.org/10.1073/pnas.2113265119.

(14) Broecker, W. S.; Oversby, V. M. *Chemical Equilibria in the Earth*; International Series in the earth and planetary sciences; McGraw-Hill: New York u.a, 1971.

(15) Bastrikov, V.; Steen-Larsen, H. C.; Masson-Delmotte, V.; Gribanov, K.; Cattani, O.; Jouzel, J.; Zakharov, V. Continuous Measurements of Atmospheric Water Vapour Isotopes in Western Siberia (Kourovka). *Atmospheric Meas. Tech.* **2014**, *7* (6), 1763–1776. https://doi.org/10.5194/amt-7-1763-2014.

(16) Holt, B. D.; Cunningham, P. T.; Engelkemeir, A. G.; Graczyk, D. G.; Kumar, R. Oxygen-18 Study of Nonaqueous-Phase Oxidation of Sulfur Dioxide. *Atmospheric Environ. 1967* **1983**, *17* (3), 625–632. https://doi.org/10.1016/0004-6981(83)90136-1.

(17) Liu, T.; Abbatt, J. P. D. Oxidation of Sulfur Dioxide by Nitrogen Dioxide Accelerated at the Interface of Deliquesced Aerosol Particles. *Nat. Chem.* **2021**, *13* (12), 1173–1177. https://doi.org/10.1038/s41557-021-00777-0.

(18) Shao, J.; Chen, Q.; Wang, Y.; Lu, X.; He, P.; Sun, Y.; Shah, V.; Martin, R. V.; Philip, S.; Song, S.; Zhao, Y.; Xie, Z.; Zhang, L.; Alexander, B. Heterogeneous Sulfate Aerosol Formation Mechanisms during Wintertime Chinese Haze Events: Air Quality Model Assessment Using Observations of Sulfate Oxygen Isotopes in Beijing. *Atmospheric Chem. Phys.* **2019**, *19* (9), 6107–6123. https://doi.org/10.5194/acp-19-6107-2019.

(19) He, P.; Alexander, B.; Geng, L.; Chi, X.; Fan, S.; Zhan, H.; Kang, H.; Zheng, G.; Cheng, Y.; Su, H.; Liu, C.; Xie, Z. Isotopic Constraints on Heterogeneous Sulfate Production in Beijing Haze. *Atmospheric Chem. Phys.* **2018**, *18* (8), 5515–5528. https://doi.org/10.5194/acp-18-5515-2018.

(20) Alexander, B.; Park, R. J.; Jacob, D. J.; Gong, S. Transition Metal-Catalyzed Oxidation of Atmospheric Sulfur: Global Implications for the Sulfur Budget. *J. Geophys. Res.* **2009**, *114* (D2), D02309. https://doi.org/10.1029/2008JD010486.

(21) Wang, X.; Gemayel, R.; Hayeck, N.; Perrier, S.; Charbonnel, N.; Xu, C.; Chen, H.; Zhu, C.; Zhang, L.; Wang, L.; Nizkorodov, S. A.; Wang, X.; Wang, Z.; Wang, T.; Mellouki, A.; Riva, M.; Chen, J.; George, C. Atmospheric Photosensitization: A New Pathway for Sulfate Formation. *Environ. Sci. Technol.* **2020**, *54* (6), 3114–3120. https://doi.org/10.1021/acs.est.9b06347.

(22) Savarino, J.; Thiemens, M. H. Analytical Procedure to Determine Both Δ18O and Δ17O of H2O2 in Natural Water and First Measurements. *Atmos. Environ.* **1999**, *33* (22), 3683–3690. https://doi.org/10.1016/S1352-2310(99)00122-3.

(23) Vicars, W. C.; Savarino, J. Quantitative Constraints on the 17O-Excess (Δ17O) Signature of Surface Ozone: Ambient Measurements from 50°N to 50°S Using the Nitrite-Coated Filter Technique. *Geochim. Cosmochim. Acta* **2014**, *135*, 270–287. https://doi.org/10.1016/j.gca.2014.03.023.

(24) Savarino, J.; Lee, C. C. W.; Thiemens, M. H. Laboratory Oxygen Isotopic Study of Sulfur (IV) Oxidation: Origin of the Mass-Independent Oxygen Isotopic Anomaly in Atmospheric Sulfates and Sulfate Mineral Deposits on Earth. *J. Geophys. Res. Atmospheres* **2000**, *105* (D23), 29079–29088. https://doi.org/10.1029/2000JD900456.

(25) Faust, B. C.; Anastasio, C.; Allen, J. M.; Arakaki, T. Aqueous-Phase Photochemical Formation of Peroxides in Authentic Cloud and Fog Waters. *Science* **1993**, *260* (5104), 73–75. https://doi.org/10.1126/science.8465202.

(26) Ye, C.; Chen, H.; Hoffmann, E. H.; Mettke, P.; Tilgner, A.; He, L.; Mutzel, A.; Brüggemann, M.; Poulain, L.; Schaefer, T.; Heinold, B.; Ma, Z.; Liu, P.; Xue, C.; Zhao, X.; Zhang, C.; Zhang, F.; Sun, H.; Li, Q.; Wang, L.; Yang, X.; Wang, J.; Liu, C.; Xing, C.; Mu, Y.; Chen, J.; Herrmann, H. Particle-Phase Photoreactions of HULIS and TMIs Establish a Strong Source of H_2O_2 and Particulate Sulfate in the Winter North China Plain. *Environ. Sci. Technol.* **2021**, *55* (12), 7818–7830. https://doi.org/10.1021/acs.est.1c00561.

(27) Harris, E.; Sinha, B.; Foley, S.; Crowley, J. N.; Borrmann, S.; Hoppe, P. Sulfur Isotope Fractionation during Heterogeneous Oxidation of SO<Sub>2</Sub> on Mineral Dust. *Atmospheric Chem. Phys.* **2012**, *12* (11), 4867–4884. https://doi.org/10.5194/acp-12-4867-2012.

(28) Dominguez, G.; Jackson, T.; Brothers, L.; Barnett, B.; Nguyen, B.; Thiemens, M. H. Discovery and Measurement of an Isotopically Distinct Source of Sulfate in Earth's Atmosphere. *Proc. Natl. Acad. Sci.* **2008**, *105* (35), 12769–12773. https://doi.org/10.1073/pnas.0805255105.

(29) Au Yang, D.; Bardoux, G.; Assayag, N.; Laskar, C.; Widory, D.; Cartigny, P. Atmospheric SO2 Oxidation by NO2 Plays No Role in the Mass Independent Sulfur Isotope Fractionation of

Urban Aerosols. *Atmos. Environ.* **2018**, *193*, 109–117. https://doi.org/10.1016/j.atmosenv.2018.09.007.

(30) Sofen, E. D.; Alexander, B.; Kunasek, S. A. The Impact of Anthropogenic Emissions on Atmospheric Sulfate Production Pathways, Oxidants, and Ice Core Δ<Sup>17</Sup>O(SO<Sub>4</Sub><Sup>2–</Sup>). *Atmospheric Chem. Phys.* **2011**, *11* (7), 3565–3578. https://doi.org/10.5194/acp-11-3565-2011.

(31) Lyons, J. R. Transfer of Mass-Independent Fractionation in Ozone to Other Oxygen-Containing Radicals in the Atmosphere. *Geophys. Res. Lett.* **2001**, *28* (17), 3231–3234. https://doi.org/10.1029/2000GL012791.

(32) Anastasio, C.; Jordan, A. L. Photoformation of Hydroxyl Radical and Hydrogen Peroxide in Aerosol Particles from Alert, Nunavut: Implications for Aerosol and Snowpack Chemistry in the Arctic. *Atmos. Environ.* **2004**, *38* (8), 1153–1166. https://doi.org/10.1016/j.atmosenv.2003.11.016.

(33) Chu, L.; Anastasio, C. Formation of Hydroxyl Radical from the Photolysis of Frozen Hydrogen Peroxide. *J. Phys. Chem. A* **2005**, *109* (28), 6264–6271. https://doi.org/10.1021/jp051415f.

(34) Dubey, M. K.; Mohrschladt, R.; Donahue, N. M.; Anderson, J. G. Isotope Specific Kinetics of Hydroxyl Radical (OH) with Water (H_2O): Testing Models of Reactivity and Atmospheric Fractionation. *J. Phys. Chem. A* **1997**, *101* (8), 1494–1500. https://doi.org/10.1021/jp962332p.

(35) Lee, C. C.-W.; Savarino, J. H.; Cachier, H.; Thiemens, M. H. Sulfur (32S, 33S, 34S, 36S) and Oxygen (16O,17O,18O) Isotopic Ratios of Primary Sulfate Produced from Combustion Processes. *Tellus B* **2002**, *54* (3), 193–200. https://doi.org/10.1034/j.1600-0889.2002.01384.x.

(36) Harris, E.; Sinha, B.; Hoppe, P.; Foley, S.; Borrmann, S. Fractionation of Sulfur Isotopes during Heterogeneous Oxidation of SO<Sub>2</Sub> on Sea Salt Aerosol: A New Tool to Investigate Non-Sea Salt Sulfate Production in the Marine Boundary Layer. *Atmospheric Chem. Phys.* **2012**, *12* (10), 4619–4631. https://doi.org/10.5194/acp-12-4619-2012.

(37) Yang, Y.; Weber, R. J. Ultrafiltration to Characterize PM2.5 Water-Soluble Iron and Its Sources in an Urban Environment. *Atmos. Environ.* **2022**, *286*, 119246. https://doi.org/10.1016/j.atmosenv.2022.119246.

(38) Anastasio, C.; Faust, B. C.; Rao, C. J. Aromatic Carbonyl Compounds as Aqueous-Phase Photochemical Sources of Hydrogen Peroxide in Acidic Sulfate Aerosols, Fogs, and Clouds. 1. Non-Phenolic Methoxybenzaldehydes and Methoxyacetophenones with Reductants (Phenols). *Environ. Sci. Technol.* **1997**, *31* (1), 218–232. https://doi.org/10.1021/es960359g.

```
#####################################################################################
```

Here is the code for the Bayesian isotope mixing model used in this study including source signature calculations.

```
import arviz as az
import corner
import matplotlib as mpl
import matplotlib.pyplot as plt
import numpy as np
import scipy.stats as stats
import pandas as pd
import pymc as pm
import pymc.sampling_jax
import jaxlib

###read in data here
obs_rawdata_df = pd.read_excel('###')
obs_data_df = obs_rawdata_df.set_index('sampleID')
obs_data_df

#Configurations
NUM_MCMC_CHAINS = 10
LENGTH_MCMC_CHAIN = 40000
BURNIN_LENGTH = int(0.25*LENGTH_MCMC_CHAIN) # discard this number of initial steps while calculating the statisics of f

all_factor_marginal_stats_df_arr = []
modeled_val_df_arr = []
samples_closet_to_median_in_5D = []
idata_arr = []

obs_data_for_pymc_df = obs_data_df.iloc[0:10]
d34S = obs_data_df['d34S']
d18O = obs_data_df['O18']
D17O = obs_data_df['O17']
SOR = obs_data_df['SOR']
temp = obs_data_df['CTC_temp_3m_C']

### d18O(SO4) source signatures
# gas-phase chemistry
d18O_H2O_vapor = (temp*0.403)-25.946
d18O_OH = (0.71*d18O_H2O_vapor)+16.5

#aqueous-phase chemistry
d18O_H2O_liquid = (temp*0.4315) - 17.224
d18O_SIV = (d18O_H2O_liquid*0.9447) + 7.7837

d18O_NO2 = (d18O_SIV*0.75) + (d18O_H2O_liquid*0.25)
```

```
d18O_TMI = (d18O_SIV*0.75) + (23.5*0.25) #d18O(O2) = 23.5
d18O_H2O2 = (d18O_SIV*0.5) + (35*0.5) #d18O(H2O2) = 35
d18O_HOOH = (d18O_SIV*0.5) + (23.5*0.5) #d18O(O2(aq))= 23.5
d18O_O3 = (d18O_SIV*0.75) + (130*0.25) #d18O(O3) = 130
d18O_primary = 23.5

### D17O(SO4) source signatures
D17O_primary = -0.34 #Unit: per mille
D17O_O3 = 9.8 #Unit: per mille
D17O_H2O2 =   0.81
D17O_HOOH =   -0.17
D17O_OH = 0
D17O_TMI = -0.085
D17O_NO2 = 0
### d34S(SO4) source signatures
#reference Harris et al. 2012 and 2013
# e = epsilon values

e_OH = (-0.004*temp) + 10.6 + 1
e_H2O2 = (-0.085*temp) + 16.51 + 1
e_O3 = (-0.085*temp) + 16.51 + 1
e_TMI = (-0.237*temp) + -5.039 +1
e_NO2 = 1
d34S_SO4_primary = 4.7
d34S_emission = 4.7

obs_data_for_pymc_df = obs_data_df.iloc[0:63]
for i_sample_id in obs_data_for_pymc_df.index:
  i_d18O = obs_data_df.loc[i_sample_id, 'O18']
  i_D17O = obs_data_df.loc[i_sample_id, 'O17']
  i_d34S =obs_data_df.loc[i_sample_id, 'd34S']
  i_SO4_obs = obs_data_df.loc[i_sample_id, 'SO4_umol']
  i_SO2_obs = obs_data_df.loc[i_sample_id, 'SO2_umol']
  i_e_TMI = obs_data_df.loc[i_sample_id, 'e_TMI']
  i_e_O3 = obs_data_df.loc[i_sample_id, 'e_O3']
  i_e_H2O2 = obs_data_df.loc[i_sample_id, 'e_H2O2']
  i_e_OH = obs_data_df.loc[i_sample_id, 'e_OH']
  i_d18O_TMI = obs_data_df.loc[i_sample_id, 'd18O_TMI']
  i_d18O_O3 = obs_data_df.loc[i_sample_id, 'd18O_O3']
  i_d18O_H2O2 = obs_data_df.loc[i_sample_id, 'd18O_H2O2']
  i_d18O_OH = obs_data_df.loc[i_sample_id, 'd18O_OH']
  i_d18O_NO2 = obs_data_df.loc[i_sample_id, 'd18O_NO2']
  i_obs = np.array([i_D17O, i_d18O, i_d34S]) # order: D17O, d18O

  with pm.Model() as model:
    # this is where you weigh the importance of different pathways.
    #Its useful when two signatures are very similar
    #but you have good reason to believe one is more dominant than another
```

```
    #(pH, photolysis rates, O3 obs, HYSPLIT, etc)
    f = pm.Dirichlet('f', a=[1,1,1,1,1,1]) # Using equal weight prior

    f_primary = pm.Deterministic("f_primary", f[0])
    f_OH = pm.Deterministic("f_OH", f[1])
    #f_HOOH_pm = pm.Deterministic("f_HOOH_pm", f[2])
    f_H2O2 = pm.Deterministic("f_H2O2", f[2])
    f_TMI = pm.Deterministic("f_TMI", f[3])
    f_O3 = pm.Deterministic("f_O3", f[4])
    f_NO2 = pm.Deterministic("f_NO2", f[5])

    # Statistics of the observations
    ###these are the analytical errors // can also expand to get a larger range of uncertainty
    obs_D17O_std = 0.16 #Unit: per mille
    obs_d18O_std =  0.8 #Unit: per mille
    obs_d34S_std = 1.0
    obs_D17O_var = obs_D17O_std**2
    obs_d18O_var = obs_d18O_std**2
    obs_d34S_var= obs_d34S_std**2
    obs_D17O_d18O_correlation = 0.0
    obs_D17O_d34S_correlation = 0.0
    obs_d18O_d34S_correlation = 0.0

    obs_D17O_d18O_cov = obs_D17O_std*obs_d18O_std*obs_D17O_d18O_correlation
    obs_D17O_d34S_cov = obs_D17O_std*obs_d34S_std* obs_D17O_d34S_correlation
    obs_d18O_d34S_cov = obs_d18O_std*obs_d34S_std*obs_d18O_d34S_correlation

    # Main dish :-)
    model_D17O = pm.Deterministic("model_D17O", f_primary*D17O_primary + f_O3*D17O_O3 +
f_H2O2*D17O_H2O2 + f_OH*D17O_OH + f_NO2*D17O_NO2 +f_TMI*D17O_TMI )
    model_d18O = pm.Deterministic("model_d18O", f_primary*d18O_primary + f_O3*i_d18O_O3 +
f_H2O2*i_d18O_H2O2 + f_OH*i_d18O_OH +f_NO2*i_d18O_NO2 + f_TMI*i_d18O_TMI)
    ###we calculate SOR_2nd since the fraction of primary sulfate is large and independent of chemical
fractionation
    ###this is not necessary in secondary sulfate-dominated regimes
    SO4_secondary_umol = i_SO4_obs*(1-f_primary)
    SOR_2nd = SO4_secondary_umol  / (SO4_secondary_umol + i_SO2_obs)
    model_d34S_epsilon = pm.Deterministic("model_d34S_epsilon", f_primary*4.7 + (1-f_primary)*(-
1*((d34S_emission- (i_e_O3*f_O3/(1-f_primary)+ (i_e_H2O2*f_H2O2/(1-f_primary))+
(i_e_OH*f_OH/(1-f_primary)) + (e_NO2*f_NO2/(1-f_primary))+ (i_e_TMI*f_TMI/(1-
f_primary))*(np.log(SOR_2nd)*((1-SOR_2nd)/SOR_2nd)))))))

    # Likelihood function
    obs = pm.MvNormal("obs", observed = i_obs,
                    mu=[model_D17O, model_d18O,model_d34S_epsilon],
                    cov=np.array([[obs_D17O_var,obs_D17O_d18O_cov,obs_D17O_d34S_cov],
                            [obs_D17O_d18O_cov,obs_d18O_var,obs_d18O_d34S_cov],
                            [obs_D17O_d34S_cov,obs_d18O_d34S_cov,obs_d34S_var]]))
```

```
    idata_Dirichlet = pm.sampling_jax.sample_numpyro_nuts(draws=LENGTH_MCMC_CHAIN,
                                                          chains=NUM_MCMC_CHAINS,
                                                          tune=4000)

  # Create the corner plot
  corner.corner(idata_Dirichlet, var_names=['f_primary', 'f_OH', 'f_H2O2', 'f_TMI', 'f_O3', 'f_NO2'])
  plt.suptitle("{}'s corner plot".format(i_sample_id), fontsize=30)
  plt.show()

  # Save the statistics for each sample for later

  i_all_factor_df = idata_Dirichlet['posterior']['f'].isel(draw=slice(BURNIN_LENGTH,
None)).stack({'sample':['chain','draw']}).to_dataframe()['f'].unstack('f_dim_0')
  i_all_factor_df.rows = ['f_primary', 'f_OH', 'f_H2O2', 'f_TMI', 'f_O3', 'f_NO2']
  i_all_factor_marginal_stats_df = pd.DataFrame()

  for i_factor in i_all_factor_df.columns:

    i_all_factor_marginal_stats_df.loc['2.5th percentile',i_factor] =
i_all_factor_df[i_factor].quantile(0.025)
    i_all_factor_marginal_stats_df.loc['25th percentile',i_factor]  = i_all_factor_df[i_factor].quantile(0.25)
    i_all_factor_marginal_stats_df.loc['Median',i_factor]  = i_all_factor_df[i_factor].quantile(0.5)
    i_all_factor_marginal_stats_df.loc['75th percentile',i_factor]  = i_all_factor_df[i_factor].quantile(0.75)
    i_all_factor_marginal_stats_df.loc['97.5th percentile',i_factor]  =
i_all_factor_df[i_factor].quantile(0.975)

  all_factor_marginal_stats_df_arr += [i_all_factor_marginal_stats_df]

  i_model_vals_df = idata_Dirichlet.posterior[['model_D17O', 'model_d18O',
'model_d34S_epsilon']].isel(draw=slice(BURNIN_LENGTH,
None)).stack({'sample':['chain','draw']}).to_dataframe()
  i_modeled_val_stats_df = pd.DataFrame()

  for i_model_val_type in ['model_D17O', 'model_d18O', 'model_d34S_epsilon']:

    i_modeled_val_stats_df.loc['2.5th percentile',i_model_val_type] =
i_model_vals_df[i_model_val_type].quantile(0.025)
    i_modeled_val_stats_df.loc['25th percentile',i_model_val_type]  =
i_model_vals_df[i_model_val_type].quantile(0.25)
    i_modeled_val_stats_df.loc['Median',i_model_val_type]  =
i_model_vals_df[i_model_val_type].quantile(0.5)
    i_modeled_val_stats_df.loc['75th percentile',i_model_val_type]  =
i_model_vals_df[i_model_val_type].quantile(0.75)
    i_modeled_val_stats_df.loc['97.5th percentile',i_model_val_type]  =
i_model_vals_df[i_model_val_type].quantile(0.975)

  modeled_val_df_arr += [i_modeled_val_stats_df]
```

```
  idata_arr += [idata_Dirichlet]

  ################################################################################
  #### Output statistics
  all_factor_marginal_stats_df = pd.concat(all_factor_marginal_stats_df_arr, axis=0,
keys=obs_data_for_pymc_df.index)
modeled_vals_df = pd.concat(modeled_val_df_arr, axis=0, keys=obs_data_for_pymc_df.index)
modeled_D17O_stats_df = modeled_vals_df.loc[:,'model_D17O'].unstack()
modeled_d18O_stats_df = modeled_vals_df.loc[:,'model_d18O'].unstack()
modeled_d34S_stats_df = modeled_vals_df.loc[:, 'model_d34S_epsilon'].unstack()

all_factor_marginal_stats_df = pd.concat(all_factor_marginal_stats_df_arr, axis=0,
keys=obs_data_for_pymc_df.index)
modeled_vals_df = pd.concat(modeled_val_df_arr, axis=0, keys=obs_data_for_pymc_df.index)
modeled_D17O_stats_df = modeled_vals_df.loc[:,'model_D17O'].unstack()
modeled_d18O_stats_df = modeled_vals_df.loc[:, 'model_d18O'].unstack()
modeled_d34S_stats_df = modeled_vals_df.loc[:,'model_d34S_epsilon'].unstack()

f_primary_marginal_stats_df = all_factor_marginal_stats_df.loc[:,0].unstack()
f_OH_marginal_stats_df = all_factor_marginal_stats_df.loc[:,1].unstack()
f_HOOH_marginal_stats_df = all_factor_marginal_stats_df.loc[:,2].unstack()
f_TMI_marginal_stats_df = all_factor_marginal_stats_df.loc[:,3].unstack()
f_O3_marginal_stats_df = all_factor_marginal_stats_df.loc[:,4].unstack()
f_NO2_marginal_stats_df = all_factor_marginal_stats_df.loc[:,5].unstack()

f_primary_marginal_stats_df = all_factor_marginal_stats_df.loc[:,0].unstack()
Primary = f_primary_marginal_stats_df['97.5th percentile']
print(*Primary)

f_OH_marginal_stats_df = all_factor_marginal_stats_df.loc[:,1].unstack()
OH = f_OH_marginal_stats_df['97.5th percentile']
print(*OH)

f_H2O2_marginal_stats_df = all_factor_marginal_stats_df.loc[:,2].unstack()
H2O2 = f_H2O2_marginal_stats_df['97.5th percentile']
print(*H2O2)

f_TMI_marginal_stats_df = all_factor_marginal_stats_df.loc[:,3].unstack()
TMI = f_TMI_marginal_stats_df['97.5th percentile']
print(*TMI)

f_O3_marginal_stats_df = all_factor_marginal_stats_df.loc[:,4].unstack()
O3 = f_O3_marginal_stats_df['97.5th percentile']
print(*O3)

f_NO2_marginal_stats_df = all_factor_marginal_stats_df.loc[:,5].unstack()
NO2 = f_NO2_marginal_stats_df['97.5th percentile']
```

```
print(*NO2)


f_primary_marginal_stats_df = all_factor_marginal_stats_df.loc[:,0].unstack()
Primary = f_primary_marginal_stats_df['2.5th percentile']
print(*Primary)

f_OH_marginal_stats_df = all_factor_marginal_stats_df.loc[:,1].unstack()
OH = f_OH_marginal_stats_df['2.5th percentile']
print(*OH)

f_H2O2_marginal_stats_df = all_factor_marginal_stats_df.loc[:,2].unstack()
H2O2 = f_H2O2_marginal_stats_df['2.5th percentile']
print(*H2O2)

f_TMI_marginal_stats_df = all_factor_marginal_stats_df.loc[:,3].unstack()
TMI = f_TMI_marginal_stats_df['2.5th percentile']
print(*TMI)

f_O3_marginal_stats_df = all_factor_marginal_stats_df.loc[:,4].unstack()
O3 = f_O3_marginal_stats_df['2.5th percentile']
print(*O3)

f_NO2_marginal_stats_df = all_factor_marginal_stats_df.loc[:,5].unstack()
NO2 = f_NO2_marginal_stats_df['2.5th percentile']
print(*NO2)

####### compare model output with observations
all_factor_marginal_stats_df = pd.concat(all_factor_marginal_stats_df_arr, axis=0,
keys=obs_data_for_pymc_df.index)
modeled_vals_df = pd.concat(modeled_val_df_arr, axis=0, keys=obs_data_for_pymc_df.index)
modeled_D17O_stats_df = modeled_vals_df.loc[:,'model_D17O'].unstack()
modeled_d18O_stats_df = modeled_vals_df.loc[:,'model_d18O'].unstack()
#modeled_d34S_stats_df = modeled_vals_df.loc[:, 'model_d34S'].unstack()
modeled_d34S_stats_df = modeled_vals_df.loc[:, 'model_d34S_epsilon'].unstack()

all_factor_marginal_stats_df = pd.concat(all_factor_marginal_stats_df_arr, axis=0,
keys=obs_data_for_pymc_df.index)
modeled_vals_df = pd.concat(modeled_val_df_arr, axis=0, keys=obs_data_for_pymc_df.index)
modeled_D17O_stats_df = modeled_vals_df.loc[:,'model_D17O'].unstack()
modeled_d18O_stats_df = modeled_vals_df.loc[:, 'model_d18O'].unstack()
#modeled_d34S_stats_df = modeled_vals_df.loc[:, 'model_d34S'].unstack()
modeled_d34S_stats_df = modeled_vals_df.loc[:,'model_d34S_epsilon'].unstack()

f_primary_marginal_stats_df = all_factor_marginal_stats_df.loc[:,0].unstack()
f_O3_marginal_stats_df = all_factor_marginal_stats_df.loc[:,4].unstack()
#f_H2O2_marginal_stats_df = all_factor_marginal_stats_df.loc[:,2].unstack()
f_OH_marginal_stats_df = all_factor_marginal_stats_df.loc[:,1].unstack()
```

```
f_TMI_marginal_stats_df = all_factor_marginal_stats_df.loc[:,3].unstack()
f_NO2_marginal_stats_df = all_factor_marginal_stats_df.loc[:,5].unstack()
f_HOOH_marginal_stats_df = all_factor_marginal_stats_df.loc[:,2].unstack()
i_SO4_obs = obs_data_df.loc[i_sample_id, 'SO4_umol']
i_SO2_obs = obs_data_df.loc[i_sample_id, 'SO2_umol']
i_d34S =obs_data_df.loc[i_sample_id, 'd34S']

plt.figure(figsize=(5,5), dpi=300)
plt.scatter(y=modeled_D17O_stats_df['Median'],
          x=obs_data_df.loc[obs_data_for_pymc_df.index,'O17'],
          marker='x', color='k')

plt.plot(np.arange(-100,100),
       np.arange(-100,100),
       linestyle='--', alpha=0.5, color='k')
plt.gca().set_aspect('equal')

plt.xlim(-0.3,3)
plt.xlabel('$\Delta^{17}$O Observations(‰)')

plt.ylim(-0.3,3)
plt.ylabel('MCMC Median $\Delta^{17}$O (‰)')
plt.title('$\Delta^{17}$O')
plt.show()


plt.figure(figsize=(5,5),  dpi=300)
plt.scatter(y=modeled_d18O_stats_df['Median'],
          x=obs_data_df.loc[obs_data_for_pymc_df.index,'O18'],
          marker='x', color='k')

plt.plot(np.arange(-100,100),
       np.arange(-100,100),
       linestyle='--', alpha=0.5, color='k')
plt.gca().set_aspect('equal')

plt.xlim(0,25)
plt.ylim(0,25)
plt.xlabel('$\delta^{18}$O Observations (‰)')
plt.ylabel('MCMC Median $\delta^{18}$O (‰)')
plt.title(' $\delta^{18}$O')

plt.show()

plt.figure(figsize=(5,5),  dpi=300)
plt.scatter(y=modeled_d34S_stats_df['Median'],
          x=obs_data_df.loc[obs_data_for_pymc_df.index,'d34S'],
          marker='x', color='k')
```

```
plt.plot(np.arange(-100,100),
        np.arange(-100,100),
        linestyle='--', alpha=0.5, color='k')
plt.gca().set_aspect('equal')

plt.xlim(3.3,10)
plt.ylim(3,10)
#ax.text(4, 9, 'R$^$ = 0.68', color = 'k', fontsize = 22)

plt.xlabel('$\delta^{34}$S Observations (‰)')
plt.ylabel('MCMC Median $\delta^{34}$S (‰)')
plt.title('$\delta^{34}$S')

plt.show()

plt.figure(figsize=(10,5), dpi=300)

plt.plot(modeled_D17O_stats_df.index,
        modeled_D17O_stats_df['Median'],
        label="MCMC samples' median",
        linewidth=3, alpha=.7, color='darkgoldenrod')
plt.fill_between(x=modeled_D17O_stats_df.index,
                y1=modeled_D17O_stats_df['2.5th percentile'],
                y2=modeled_D17O_stats_df['97.5th percentile'],
                label="MCMC samples' 2.5 to 97.5th percentiles",
                linewidth=2, alpha=.25, color='goldenrod')

plt.plot(obs_data_for_pymc_df.index,
        obs_data_df.loc[obs_data_for_pymc_df.index,'O17'],
        label="Observations",
        color='k', linewidth=2, alpha=.7)

plt.tick_params(rotation=90, axis='x')
plt.ylabel(('$\Delta^{17}$O ‰'))

plt.legend()
plt.title('$\Delta^{17}$O', fontsize=18)
plt.show()


# Plot d18O

plt.figure(figsize=(10,5), dpi=300)

plt.plot(modeled_d18O_stats_df.index,
        modeled_d18O_stats_df['Median'],
        label="MCMC samples' median",
```

```
        linewidth=3, alpha=.75, color='purple')
plt.fill_between(x=modeled_d18O_stats_df.index,
              y1=modeled_d18O_stats_df['2.5th percentile'],
              y2=modeled_d18O_stats_df['97.5th percentile'],
              label="MCMC samples' 2.5 to 97.5th percentiles",
              linewidth=2, alpha=.1, color='indigo')

plt.plot(obs_data_for_pymc_df.index,
        obs_data_df.loc[obs_data_for_pymc_df.index,'O18'],
        label="Observations",
        color='k', linewidth=2, alpha=.6)

plt.tick_params(rotation=90, axis='x')
plt.ylabel(('$\delta^{18}$O ‰'))

plt.legend()
plt.title(' $\delta^{18}$O',fontsize=18)
plt.show()


# Plot d34S_2nd
plt.figure(figsize=(10,5), dpi=300)

plt.plot(modeled_d34S_stats_df.index,
        modeled_d34S_stats_df['Median'],
        label="MCMC samples' median",
        linewidth=3, alpha=.75, color='b')
plt.fill_between(x=modeled_d34S_stats_df.index,
              y1=modeled_d34S_stats_df['2.5th percentile'],
              y2=modeled_d34S_stats_df['97.5th percentile'],
              label="MCMC samples' 2.5 to 97.5th percentiles",
              linewidth=2, alpha=.1, color='b')

plt.plot(obs_data_for_pymc_df.index,
        obs_data_df.loc[obs_data_for_pymc_df.index,'d34S'],
        label="Observations",
        color='k', linewidth=2, alpha=.6)

plt.tick_params(rotation=90, axis='x')
plt.ylabel(('$\delta^{34}$S ‰'))

plt.legend()
plt.title('$\delta^{34}$S',fontsize=18)
plt.show()

d34S_2nd = modeled_d34S_stats_df['Median']
d34S_lower = modeled_d34S_stats_df['2.5th percentile']
d34S_upper = modeled_d34S_stats_df['97.5th percentile']
```

```
f_primary = f_primary_marginal_stats_df['Median']

d34S_MCMC = (f_primary*4.5) + (d34S_2nd*(1-f_primary))
d34S_MCMC_lower = (f_primary*4.5) + (d34S_lower *(1-f_primary))
d34S_MCMC_upper = (f_primary*4.5) + (d34S_upper *(1-f_primary))

plt.figure(figsize=(10,5), dpi=300)

plt.plot(modeled_d34S_stats_df.index,
        d34S_MCMC,
        label="MCMC samples' median",
        linewidth=3, alpha=.75, color='b')
plt.fill_between(x=modeled_d34S_stats_df.index,
              y1=d34S_MCMC_lower ,
              y2=d34S_MCMC_upper,
              label="MCMC samples' 2.5 to 97.5th percentiles",
              linewidth=2, alpha=.1, color='b')

plt.plot(obs_data_for_pymc_df.index,
        obs_data_df.loc[obs_data_for_pymc_df.index,'d34S'],
        label="Observations",
        color='k', linewidth=2, alpha=.6)

plt.tick_params(rotation=90, axis='x')
plt.ylabel(('$\delta^{34}$S ‰'))

plt.legend()
plt.title('$\delta^{34}$S',fontsize=18)
plt.show()

###bar chart

import seaborn as sns
from sklearn import preprocessing
import numpy as np

all_factor_marginal_stats_df = pd.concat(all_factor_marginal_stats_df_arr, axis=0,
keys=obs_data_for_pymc_df.index)

modeled_vals_df = pd.concat(modeled_val_df_arr, axis=0, keys=obs_data_for_pymc_df.index)

f_primary_marginal_stats_df = all_factor_marginal_stats_df.loc[:,0].unstack()
f_O3_marginal_stats_df = all_factor_marginal_stats_df.loc[:,4].unstack()
f_H2O2_marginal_stats_df = all_factor_marginal_stats_df.loc[:,2].unstack()
f_OH_marginal_stats_df = all_factor_marginal_stats_df.loc[:,1].unstack()
f_TMI_marginal_stats_df = all_factor_marginal_stats_df.loc[:,3].unstack()
f_NO2_marginal_stats_df = all_factor_marginal_stats_df.loc[:,5].unstack()
```

```
all_factor_marginal_stats_df = pd.concat(all_factor_marginal_stats_df_arr, axis=0,
keys=obs_data_for_pymc_df.index)

labels = f_primary_marginal_stats_df.index
labels = f_primary_marginal_stats_df.index


j=20
f_primary_marginal_stats_df = all_factor_marginal_stats_df.loc[:,0].unstack()
Primary = f_primary_marginal_stats_df['Median']

f_OH_marginal_stats_df = all_factor_marginal_stats_df.loc[:,1].unstack()
OH = f_OH_marginal_stats_df['Median']

f_H2O2_marginal_stats_df = all_factor_marginal_stats_df.loc[:,2].unstack()
H2O2 = f_H2O2_marginal_stats_df['Median']

f_TMI_marginal_stats_df = all_factor_marginal_stats_df.loc[:,3].unstack()
TMI = f_TMI_marginal_stats_df['Median']

f_O3_marginal_stats_df = all_factor_marginal_stats_df.loc[:,4].unstack()
O3 = f_O3_marginal_stats_df['Median']

f_NO2_marginal_stats_df = all_factor_marginal_stats_df.loc[:,5].unstack()
NO2 = f_NO2_marginal_stats_df['Median']


fig, ax = plt.subplots(figsize=(20,8), dpi=500)
width = 0.88

#pal = sns.color_palette("Set1")
#rescale = lambda y: (y - np.min(y)) / (np.max(y) - np.min(y))
Norm = 1/(Primary+OH+O3+TMI+H2O2+NO2)
O3 = Norm*O3
OH=Norm*OH
TMI=Norm*TMI
H2O2=Norm*H2O2
Primary =Norm*Primary
NO2 = Norm*NO2
#triplet = Norm*triplet

NO2_plt = ax.bar(labels[0:43], NO2[0:43], width, color='teal',alpha=0.6,label='NO$_2$')
O3_plt =ax.bar(labels[0:43], O3[0:43], width, bottom = NO2[0:43], color='gold', alpha=
0.8,label='O$_3$')
OH_plt=ax.bar(labels[0:43], OH[0:43], width, bottom=O3[0:43]+NO2[0:43],
color='darkorange',alpha=0.8, label='OH')
TMI_plt=ax.bar(labels[0:43], TMI[0:43], width, bottom=O3[0:43]+OH[0:43]+NO2[0:43], color=
'mediumvioletred',alpha=0.8,label='TMI')
```

```
H2O2_plt =ax.bar(labels[0:43], H2O2[0:43], width,
bottom=O3[0:43]+TMI[0:43]+OH[0:43]+NO2[0:43],color='mediumblue', alpha=0.5, label='H$_2$O$_2$')
primary_plt = ax.bar(labels[0:43], Primary[0:43], width,
bottom=OH[0:43]+TMI[0:43]+H2O2[0:43]+O3[0:43]+NO2[0:43],color='midnightblue',alpha=0.8,label='Pr
imary')
#NO2_plt = ax.bar(labels, NO2, width,
bottom=OH+TMI+H2O2+O3+Primary+NO2,color='teal',alpha=0.6,label='NO2')
#triplet_plt = ax.bar(labels, triplet, width,
bottom=OH+TMI+H2O2+O3+Primary+NO2,color='mediumblue',alpha=0.15,label='triplet')

ax.set_xticks(f_primary_marginal_stats_df.index[0:43])
ax.set_xlabel('Sample ID',fontsize=16)

ax.tick_params(axis = 'y', labelsize=16, rotation=0)
plt.tick_params(rotation=90, axis='x',labelsize=16)

ax.set_ylabel('Fraction of PM0.7 Sulfate',fontsize=20)
ax.set_title('Sources and Formation of Fairbanks Sulfate',fontsize=24)
ax.legend(prop={'size': 16},loc='upper center', bbox_to_anchor=(0.5, -0.3),
        fancybox=True, shadow=True, ncol=5)

for r1, r2, r3, r4, r5,r6 in zip(NO2_plt,O3_plt, OH_plt, TMI_plt, H2O2_plt,primary_plt):
    h1 = r1.get_height()
    h2 = r2.get_height()
    h3 = r3.get_height()
    h4 =r4.get_height()
    h5 = r5.get_height()
    h6 = r6.get_height()
    plt.text(r1.get_x() + r1.get_width() / 2., h1 / 2., "{}".format(np.round(h1, decimals=2)), ha="center",
va="center", color="white", fontsize=8, fontweight="bold")
    plt.text(r2.get_x() + r2.get_width() / 2., (h1 + h2/2), "{}".format(np.round(h2, decimals=2)),
ha="center", va="center", color="midnightblue", fontsize=8, fontweight="bold")
    plt.text(r3.get_x() + r3.get_width() / 2., (h1 + h2+h3/2), "{}".format(np.round(h3, decimals=2)),
ha="center", va="center", color="white", fontsize=8, fontweight="bold")
    plt.text(r4.get_x() + r4.get_width() / 2., (h1 + h2+h3+h4/2), "{}".format(np.round(h4, decimals=2)),
ha="center", va="center", color="white", fontsize=8, fontweight="bold")
    plt.text(r5.get_x() + r5.get_width() / 2., (h1 + h2+h3+h4+h5/2), "{}".format(np.round(h5, decimals=2)),
ha="center", va="center", color="white", fontsize=8, fontweight="bold")
    plt.text(r6.get_x() + r6.get_width() / 2., (h1 + h2+h3+h4+h5+h6/2), "{}".format(np.round(h6,
decimals=2)), ha="center", va="center", color="white", fontsize=8, fontweight="bold")

plt.show()

###time series with 95% confidence interval
import matplotlib.dates as mdates
all_factor_marginal_stats_df = pd.concat(all_factor_marginal_stats_df_arr, axis=0,
keys=obs_data_for_pymc_df.index)
```

```
all_factor_marginal_stats_df = pd.concat(all_factor_marginal_stats_df_arr, axis=0,
keys=obs_data_for_pymc_df.index)
modeled_vals_df = pd.concat(modeled_val_df_arr, axis=0, keys=obs_data_for_pymc_df.index[0:43])
modeled_D17O_stats_df = modeled_vals_df.loc[:,'model_D17O'].unstack()
modeled_d18O_stats_df = modeled_vals_df.loc[:, 'model_d18O'].unstack()
modeled_d34S_stats_df = modeled_vals_df.loc[:,'model_d34S_epsilon'].unstack()

f_primary_marginal_stats_df = all_factor_marginal_stats_df.loc[:,0].unstack()
f_O3_marginal_stats_df = all_factor_marginal_stats_df.loc[:,4].unstack()
f_H2O2_marginal_stats_df = all_factor_marginal_stats_df.loc[:,2].unstack()
f_OH_marginal_stats_df = all_factor_marginal_stats_df.loc[:,1].unstack()
f_TMI_marginal_stats_df = all_factor_marginal_stats_df.loc[:,3].unstack()
f_NO2_marginal_stats_df = all_factor_marginal_stats_df.loc[:,5].unstack()

modeled_vals_df = pd.concat(modeled_val_df_arr, axis=0, keys=obs_data_for_pymc_df.index)
modeled_D17O_stats_df = modeled_vals_df.loc[:,'model_D17O'].unstack()
modeled_d18O_stats_df = modeled_vals_df.loc[:,'model_d18O'].unstack()

fig, ax = plt.subplots(figsize=(15,5), dpi=300)

plt.plot(f_primary_marginal_stats_df.index[0:43],
        f_primary_marginal_stats_df['Median'][0:43],
        label="Primary median",
        linewidth=4, alpha=.9, color='midnightblue')
plt.fill_between(f_primary_marginal_stats_df.index[0:43],
               y1=f_primary_marginal_stats_df['2.5th percentile'][0:43],
               y2=f_primary_marginal_stats_df['97.5th percentile'][0:43],
               #label="Primary 25 to 75th percentiles",
               linewidth=2, alpha=.05, color='midnightblue')

plt.fill_between(f_primary_marginal_stats_df.index[0:43],
              y1=f_O3_marginal_stats_df['2.5th percentile'][0:43],
              y2=f_O3_marginal_stats_df['97.5th percentile'][0:43],
              #label="O$_3$ 25 to 75th percentiles",
              linewidth=2, alpha=.2, color='gold')
plt.plot(f_primary_marginal_stats_df.index[0:43],
        f_O3_marginal_stats_df['Median'][0:43],
        label="O$_3$ Median",
        linewidth=4, alpha=0.9, color='gold')

plt.plot(f_primary_marginal_stats_df.index[0:43],
        f_OH_marginal_stats_df['Median'][0:43],
        label="OH Median",
        linewidth=4, alpha=0.9, color='darkorange')

plt.plot(f_primary_marginal_stats_df.index[0:43],
        f_H2O2_marginal_stats_df['Median'][0:43],
        label="H$_2$O$_2$ median",
```

```
     linewidth=4, alpha=0.9, color='mediumblue')
plt.fill_between(f_primary_marginal_stats_df.index[0:43],
          y1=f_H2O2_marginal_stats_df['2.5th percentile'][0:43],
          y2=f_H2O2_marginal_stats_df['97.5th percentile'][0:43],
          #label="H$_2$O$_2$ 25 to 75th percentiles",
          linewidth=2, alpha=.05, color='mediumblue')

plt.plot(f_primary_marginal_stats_df.index[0:43],
     f_TMI_marginal_stats_df['Median'][0:43],
     label="TMI-O$_2$ median",
     linewidth=4, alpha=0.9, color='mediumvioletred')
plt.fill_between(f_primary_marginal_stats_df.index[0:43],
          y1=f_TMI_marginal_stats_df['2.5th percentile'][0:43],
          y2=f_TMI_marginal_stats_df['97.5th percentile'][0:43],
         #label="TMI-O$_2$ 25 to 75th percentiles",
          linewidth=2, alpha=.1, color='mediumvioletred')

plt.plot(f_primary_marginal_stats_df.index[0:43],
     f_NO2_marginal_stats_df['Median'][0:43],
     label="NO$_2$ median",
     linewidth=4, alpha=0.9, color='gray')
plt.fill_between(f_primary_marginal_stats_df.index[0:43],
          y1=f_NO2_marginal_stats_df['2.5th percentile'][0:43],
          y2=f_NO2_marginal_stats_df['97.5th percentile'][0:43],
         #label="TMI-O$_2$ 25 to 75th percentiles",
          linewidth=2, alpha=.15, color='gray')


ax.set_xticks(f_primary_marginal_stats_df.index[0:43])
plt.ylim(0,1)
#ax.xaxis.grid()
#ax.set_xlabel('Sample ID',fontsize=20)
ax.set_ylabel('Fraction of PM0.7 Sulfate',fontsize=24)
ax.set_title('Sources and Formation of Fairbanks Sulfate',fontsize=24)

ax.legend(prop={'size': 14},loc='upper center', bbox_to_anchor=(0.5, -0.3),
      fancybox=True, shadow=True, ncol=5)
ax.tick_params(axis = 'y', labelsize=20, rotation=0)
plt.tick_params(rotation=90, axis='x',labelsize=10)
plt.show()
```